Exergy comparison of lunar propellant manufacturing and insertion into LEO using a fully reusable refueling rocket

C.M.A. Vissers - 4573005

May 15, 2023

Delft

Delft University of Technology

Table of Contents

List of Figures 5

List of Tables 7

Preface 9

Abstract 10

Executive summary 11

1 Introduction 20

2 Literature Review 23
- 2.1 Lunar Environment . . . 23
- 2.2 Power Systems . . . 23
- 2.3 Rocket System Design . . . 23
- 2.4 ISRU methods . . . 24
- 2.5 Storage . . . 24
- 2.6 Exergy . . . 24

3 Methodology 26
- 3.1 Exergy equations and balances . . . 30

4 Refueling Module 31
- 4.1 Patched Conics . . . 31
- 4.2 Propellant . . . 38
  - 4.2.1 Hydrolox . . . 38
  - 4.2.2 Oxygen . . . 38
  - 4.2.3 ALICE . . . 39
- 4.3 Refueling Operation . . . 41
  - 4.3.1 Model Derivation . . . 41
  - 4.3.2 Algorithm . . . 43
  - 4.3.3 Hydrolox Rocket . . . 44
  - 4.3.4 ALICE Rocket . . . 46
  - 4.3.5 Payload Structural Mass . . . 51
  - 4.3.6 Hydrolox Rocket Design . . . 51
  - 4.3.7 ALICE Rocket Design . . . 54
    - 4.3.7.1 Structural Mass . . . 55
  - 4.3.8 Propellant Depot . . . 56
    - 4.3.8.1 Space Weather . . . 57

5 Environment and Thermodynamic Properties 61
- 5.1 Environment . . . 61
- 5.2 Thermodynamic properties . . . 63

6 Radiation 66
- 6.1 Multi-layer insulation . . . 66
- 6.2 Passive Cooling . . . 66

7 Processes 68
- 7.1 Excavation . . . 68
- 7.2 PEM Electrolyzer . . . 72
- 7.3 Liquefaction . . . 74
- 7.4 Storage . . . 78

7.5 MRE reactor . . . 79
7.6 YSZ separator . . . 81
7.7 Aluminum Powder Manufacturing . . . 82

8 Power **87**
8.1 Nuclear Reactor . . . 87
8.2 Solar Concentrators . . . 88
8.3 Photovoltaics . . . 90

9 Results **91**

10 Discussion **93**

11 Conclusion **97**

12 Recommendations **100**

Appendix **103**
A: Patched conics & ΔV . . . 103
B: Regolith Properties . . . 104
C: Thermodynamic Properties . . . 106
D: Rocket Materials and Characteristics . . . 109
E: Atmospheric Model . . . 109
F: Sankey-Diagram . . . 110
G: YSZ-separator . . . 111

Bibliography **112**

NOMENCLATURE

α	Absorption coefficient
ΔV_a	Delta-V of ascend
ΔV_d	Delta-V of descend
ΔV_{gl}	Delta-V of gravity loss
$\Delta V_{Hohmann}$	Delta-V of a Hohmann transfer
$\Delta V_{landing}$	Delta-V of landing on the moon from LLO
ΔV_{LLO}	Delta-V of launch on the moon to LLO
ΔV_p	Delta-V for insertion or departure at perilune
$\dot{m}$	Mass flow rate
ϵ	Emissivity
η_0	Optical efficiency
$\eta_{el,m}$	Weight percentage of the element in a molecule
η_k	Weight percentage of substance k
$\eta_{m,l}$	Weight percentage a molecule in the lithosphere
$\frac{A_e}{A_t}$	Area ratio
$\frac{O}{F}$	Mass mixture ratio
Γ	Vandenkerckhove parameter
γ	specific heat ratio
μ	Standard gravitational parameter
SOI	Radius of the Sphere of Influence
ρ_f	Fuel Density
ρ_h	Hydrogen density
ρ_n	Density of the nozzle
ρ_o	Oxidizer Density
ρ_o	Oxygen density
ρ_p	Propellant Density
ρ_{shell}	Density of the shell
σ	Stefan-Boltzmann constant
σ_{a_i}	Ascend phase structural mass ratio
σ_{d_i}	Descend phase structural mass ratio
σ_e	Electrical conductivity
σ_{yield}	Yield strength of a material
ξ_{com}	Quality factor of combustion

	Yttria-Stabalized Separator
a	Semi-major axis
A_t	Surface area of a tank
$ALICE$	Aluminum Ice
B	Spalding number
c^*	Characteristic Velocity
c_p	Heat capacity
D	Diameter
e	Eccentricity
E_{ch}	Chemical Exergy
E_{kin}	Kinetic Exergy
E_{ph}	Physical Exergy
E_{pot}	Potential Gravity Exergy
E_x	Exergy of a system
ex_0^{ch}	Standard chemical exergy
g_0	Gravity constant of the Earth
g_{moon}	Gravity constant of the Moon
$GLOM$	Gross Lift-Off Mass
H	Enthalpy
h_c	Convection coefficient
$Hydrolox$	Hydrogen Liquid oxygen
I	Current
I_{sol}	Solar intensity
I_{sp}	Specific Impulse
IRT	Ideal Rocket Theory
$ISRU$	In-situ Resource Utilisation
JT	Joule-Thompson
k	Thermal conductivity
$KRUSTY$	Kilopower Reactor Using Stirling Technology
L	Length of rocket
L_c	Length of cylindrical part of tank
L_{engine}	Length of rocket engine
l_i	Number of atoms of an element in the reference species
L_{sol}	Luminocity of the sun
L_{tank}	Length of rocket tank
$LCROSS$	(Lunar Crater Observation and Sensing Satellite
LEO	Low-Earth Orbit
$LH2$	Liquid Hydrogen

LLO	Low Lunar Orbit
LOX	Liquid Oxygen
LS	Lunar Surface
M_0	Initial mass
M_0	Molar mass of the lithosphere
$m_{ablative}$	Ablative material mass
m_{av}	Avionics mass
m_{Earth}	Mass of the Earth
M_{el}	Molecular weight of an element
m_{engine}	Engine mass
m_f	Fuel Mass
m_h	Hydrogen mass
m_{ins}	Insulation mass
m_{Moon}	Mass of the moon
m_{nozzle}	Nozzle mass
m_o	Oxidizer Mass
m_o	Oxygen mass
$m_{p,a}$	Ascend phase propellant mass
$m_{p,d}$	Descend phase propellant mass
$m_{payload}$	Payload mass
M_p	Propellant mass
m_p	Propellant Mass
$m_{s,payload}$	Payload structure mass
m_{shell}	Shell mass
m_{ss}	Sum of subsystem structural masses
m_s	Structural mass
m_t	Tank mass
n_{el}	Molar concentration
p_0	Pressure of the environment
p_c	Pressure in the combustion chamber
PEL	Peak of Eternal Light
Pr	Prandtl number
PSR	Permanently Shadowed Region
PTP	Payload-to-Propellant Ratio
PV	Photovoltaic
Q	Heat
q	Heat flux
R	Radius of the rocket

r	Regression rate
R_{YSZ}	Resistance of YSZ separator
REM	Rare Earth Metal
S	Entropy
S	Safety Factor
SPE	Strong/Single Proton Event
t	Thickness of a tank
T_0	Temperature of the dead state
t_{burn}	Burn time
T_c	Temperature in the combustion chamber
T_{env}	Temperature of the environment
T_e	Temperature of the environment
T_f	Temperature of the film
T_r	Thrust of a rocket
T_s	Temperature of the system
T_w	Wall temperature
TRL	Technological Readiness Level
v_e	Exhaust velocity
V_h	Hydrogen volume
V_{orbit}	Velocity of a spacecraft in a specific orbit
V_o	Oxygen volume
W	Work
x_{in}	Mean molar fraction

List of Figures

1.1 Difference in exergy output between two outflow water levels for the same inflow water level [20] 21

3.1 Propellant Production Processes . . . 27
3.2 Schematic of propellant transportation . . . 27
3.3 Exergy Components of a system . . . 28
3.4 Different exergy states of a substance . . . 29

4.1 Refueling mission schematic . . . 31
4.2 Conditions of a spacecraft entering the lunar SOI [101] . . . 35
4.3 Schematic of all burns related to the Moon-Earth transfer trajectory . . . 37
4.4 ALICE grain density . . . 39
4.5 Algorithm procedure for rocket design mass estimation . . . 43
4.6 Heat flow and shell mass behaviour . . . 49
4.7 Length comparison of a bell and conical nozzle with the same area ratio using Rao's approach . 50
4.8 Algorithm mechanics hydrolox rocket . . . 51
4.9 Input change from upper to lower stage . . . 51
4.10 Hydrolox rocket subsystem masses . . . 52
4.11 Structural, propellant and total mass of the hydrolox rocket as a function of the rocket diameter 53
4.12 Payload-to-Propellant ratio of a hydrolox rocket carrying various payloads . . . 53
4.13 Rocket mass breakdown . . . 54
4.14 Rocket fractional mass breakdown . . . 54
4.15 Error of convergence . . . 55
4.16 Multi-stage structural mass breakdown . . . 55
4.17 Payload-to-propellant ratio of ALICE rocket . . . 56
4.18 Tiangong-1 orbital decay . . . 57
4.19 modeled behavior of atmospheric drag on a mass in LEO . . . 57
4.20 Atmospheric density as a function of altitude . . . 57
4.21 Effect of the solar cycle on air density of the upper atmosphere [10] . . . 58
4.22 Projected Area . . . 58
4.23 Force acting on the propellant depot per square meter of effective area as a function of air density for different drag coefficients . . . 59
4.24 Power requirement of the ion thruster per square meter of effective area as a function of air density for different drag coefficients . . . 59
4.25 Propellant mass requirement of the ion thruster per square meter of effective area as a function of air density for different drag coefficients . . . 59

5.1 Lunar Environment Specifications . . . 62

6.1 Radiation Cooling Behaviour . . . 67

7.1 Regolith Advanced Surface Systems Operations Robot (RASSOR) Excavator . . . 70
7.2 Proton exchange membrane electrolyzer . . . 72
7.3 Para-to-ortho conversion of hydrogen . . . 75
7.4 Linde-Hampson liquefaction cycle . . . 76
7.5 T-s diagram of the Linde-Hampson process . . . 76
7.6 MRE reactor: voltage and temperature distribution . . . 80
7.7 Aluminum nanoparticle oxide layer behavior and figure . . . 85
7.8 Effect of particle size on amount of fuel burnt . . . 85

8.1 Energy and Exergy Efficiency as a function of solar concentrator ratio . . . 89

8.2 Efficiency of solar concentrators depending on solar concentrator ratio 89
8.3 Frequency of Single Proton Events[27] 90

12.1 Heat capacity of Highlands regolith as a function of temperature 105
12.2 The schematic process of oxygen and hydrogen extraction through water electrolysis for hydrolox production 107
12.3 The schematic process of oxygen and aluminum extraction through molten regolith electrolysis for ALICE production 107
12.4 Sankey-diagram of hydrolox production 110
12.5 Sankey-diagram of ALICE production 111

List of Tables

4.1 Optimized variables for a lunar trajectory . . . 37
4.2 ΔV requirements for mission stages . . . 37
4.3 Design ΔV for two-stage rocket . . . 37
4.4 Mass Mixture Ratio, Specific Impulse, Density and Temperature for ALICE and Hydrolox rocket propellants . . . 40
4.5 Hydrolox Rocket Payload-to-Propellant ratio for different types payloads . . . 53
4.6 ALICE Rocket Payload-to-Propellant ratio for different types payloads . . . 56
4.7 Drag coefficient of various elliptical cylinders[30] [11]. . . . 58
4.8 Propellant depot characteristics for oxygen, hydrolox, and ALICE storage . . . 60

5.1 Conditions an composition of the PSR environment . . . 63
5.2 Composition of the regolith present in the PSRs . . . 63
5.3 Weight percentage of elements and molar concentration in the lithosphere . . . 63
5.4 Standard Chemical Exergy of Oxides present in the regolith . . . 64

7.1 Specifications of RASSOR [66] . . . 70
7.2 Exergy input, output and destruction for excavation . . . 71
7.3 Exergy input, output and destruction for heating . . . 73
7.4 Exergy input, output and destruction for compression . . . 73
7.5 Exergy input, output and destruction for water electrolysis . . . 74
7.6 Exergy input, output and destruction for oxygen and hydrogen liquefaction and storage . . . 78
7.7 Storage of the elements of water in lunar PSRs based on 1 million kg of electrolyzed water; top table is based on the use of MLI; the bottom table is based on maximum absorption and maximum emission . . . 79
7.8 Weight percentage of metals in regolith . . . 79
7.9 Production results of reactor operating at 2300 K for the extraction of metals and oxygen for High-Ti Mare and Highlands regolith[87] . . . 80
7.10 Yield of metals and oxygen as a percentage of regolith mass . . . 81
7.11 Yield of aluminum and oxygen after aluminum powder manufacturing as a percentage of regolith mass . . . 81
7.12 Exergy input, output and destruction of the MRE reactor . . . 81
7.13 Exergy input, output and destruction YSZ separator . . . 82
7.14 Exergy input, output and destruction aluminum particle manufacturing . . . 86

8.1 KRUSTY: Specifications[73] . . . 87

9.1 Hydrolox Production . . . 91
9.2 ALICE production . . . 91
9.3 Hydrolox Production based on a mass mixture ratio of 6.03 . . . 91
9.4 ALICE production . . . 91
9.5 Yield and Exergy input for the production of 1 kg of ALICE propellant . . . 91
9.6 Yield and Exergy input for the production of 1 kg of Hydrolox propellant . . . 92
9.7 Payload-to-Propellant ratio of the ALICE rocket for multiple payloads . . . 92
9.8 Payload-to-Propellant ratio of the hydrolox rocket for multiple payloads . . . 92
9.9 Exergy input for the transportation of 1 kg of the desired payload into LEO . . . 92

12.1 ΔV requirements for mission stages . . . 103
12.2 Optimized variables for a lunar trajectory . . . 103
12.3 Latent heat and molar concentration of multiple minerals in different types of regolith . . . 105
12.4 Iron and Silicon properties . . . 106

12.5 Properties of water . . . 106
12.6 Properties of oxygen . . . 106
12.7 Properties of hydrogen . . . 106
12.8 Ascend and descent ΔV's for the respective stages of the two-stage rocket . . . 109
12.9 Propellant properties of hydrolox and gravitational parameters of the Earth and Moon . . . 109
12.10 Combustion chamber and propellant performance characteristics for the ALICE rocket optimization algorithm . . . 109
12.11 Mechanical Properties and propellant filling factor of the Epoxy Kevlar Shell . . . 109
12.12 Ablative properties and density of Avcoat39-5026 . . . 109
12.13 Nozzle shape parameters and density . . . 109
12.14 YSZ separator variables . . . 111

PREFACE

As a mechanical engineering student that finished his bachelors after studying for 3 years at the TU Delft, doing an aerospace engineering masters was compelling. A few years ago, I made the decision to transition into space engineering because it appeared to be a field focused on exploration and pushing boundaries, representing the final frontier that could be investigated for the betterment of humanity.

The current new space race has increased the interest and innovation in the space industry, which means new opportunities for the advancement of technology and human exploration have opened up. The challenges that arise for the efficient use of technologies are innumerable. Among many, the use of in-space resources is a field of interest because it would reduce the amount of material that needs to be transported from Earth. The processing and transportation of these materials on celestial bodies needs to be researched more. One of the possibilities that became apparent is the generation of propellant on the moon that can be transported to a propellant depot in low-earth orbit. This depot could greatly reduce the initial mass of a spacecraft, making space flight cheaper and thus opening up space to more people and businesses. Naturally, it requires a lot of infrastructure and power to create rocket propellant from the cold moon rocks. This thesis aims to quantify the exergetic process to evaluate the efficiencies and magnitude of the power consumption as well as the development of a reusable two-stage rocket for two possible propellants that the moon can provide. Hopefully, my work is able to provide some insight, understanding or methods that bring us a step, although small, closer to being a true spacefaring species.

I would like to thank my parents for their support during my bachelors and masters and my supervisors Sebastien and Angelo for their patience and help during my thesis.

Casper Vissers May 15, 2023

ABSTRACT

Quantifying the exergy requirement of propellant insertion into LEO can lead to insight into the feasibility of a lunar propellant-generating architecture. Spacecraft leaving from Earth can greatly reduce their lift-off mass if in-space refueling would possible. Exergy analyses quantify the available energy of a system and show where a reduction in usable energy occurs. Insight into the exergy destruction and input provides a key parameter into the scaling and design of processes and corresponding power systems. The present study aims to define an exergy environment in the lunar PSRs and then to analyze the exergy destruction related to the production of oxygen, ALICE, and hydrolox, in terms of both manufacturing and transportation using a two-stage fully reusable rocket. Extraction processes for ALICE and hydrolox were selected and analyzed w.r.t. the lunar environment to get an understanding of the exergy input. The behavior and exergy requirements of an LEO propellant depot was described. Two fully reusable two-stage rockets using ALICE and hydrolox were designed and compared based on their payload-to-propellant ratio for the oxygen, ALICE, and hydrolox payloads. The study found that the exergetic cost for the insertion of oxygen, hydrolox, and ALICE in LEO were 1.32 $\frac{GJ}{kg}$, 1.64 $\frac{GJ}{kg}$, and 1.81 $\frac{GJ}{kg}$ and 23.3 $\frac{GJ}{kg}$, 23.4 $\frac{GJ}{kg}$ and 26.9 $\frac{GJ}{kg}$ for the hydrolox and ALICE rocket, respectively.

EXECUTIVE SUMMARY

Currently, the reemergence of interest in space-related activities has increased business opportunities. However many difficulties still need to be overcome. The mechanics of the rocket equation clearly indicate that a rise in ΔV exponentially increases the GLOM of a rocket. In-space refueling, however, can reduce both the structural mass and propellant mass of a rocket and increase the efficiency of payload transportation. Given that mission departing from Earth to LEO has a V of about 9.3-10 $\frac{km}{s}$ and a mission from the Moon to LEO has a ΔV of 6.1 $\frac{km}{s}$, the question whether a propellant-generating infrastructure on the Moon is an interesting option arises.

In order to estimate if such a refueling operation is interesting one should examine the initial mass and thus the cost of the infrastructure as well as the efficiency of propellant-generating processes that can be employed to acquire the desired propellant. Possible propellants to look at are hydrolox and ALICE, which are propellants that require hydrogen and oxygen for hydrolox and aluminum and water in the case of ALICE. Considering the LCROSS mission has found interesting amounts of water that enable the production of both hydrogen, oxygen and water, an analysis regarding the exergetic cost and feasibility can be made.

The process can be divided into two parts. The first is the propellant manufacturing and the second is the transportation of that propellant to LEO where it will be transferred to a propellant depot where spacecraft can dock to refuel. To this end a spacecraft design approach has to be chosen for both the case of a hydrolox rocket and an ALICE rocket, these spacecraft carry ALICE, oxygen or hydrolox as payload. Oxygen is being considered since both methalox and hydrolox rockets can use it as a propellant and the architectures providing the propellant have excess oxygen as a byproduct thus requiring no additional infrastructure or exergy for the synthesis of oxygen.

First, the orbital maneuvers of the refueling operation are looked at. For the preliminary mission design and estimation of the magnitudes of the ΔV a patched conics approach is chosen. A two-stage fully reusable spacecraft will decouple at LLO after which the upper stage will continue to LEO where it will refuel the propellant depot. Both stage return to the lunar surface, the lower stage after LLO insertion and the upper stage after the LEO refueling operation. To estimate the discrete ΔV burns, the trajectory is looked at in more detail. First, the spacecraft leaves the lunar surface and is placed quickly into a low lunar orbit to reduce gravity loss. From this low orbit, a Hohmann transfer is used to bring the spacecraft into a higher orbit. At this altitude, the spacecraft decouples. Now the lower stage returns to Earth, whereas the upper stage accelerates to a velocity above the escape velocity which allows it to leave the gravitational field of the Moon. As the spacecraft approaches the Earth another burn places the spacecraft in LEO for the refueling operation after which it returns to the lunar surface. The ΔV's provided by Hohmann, pathed conics and initial orbit insertion calculation are 2155 $\frac{km}{s}$ between the lunar surface and low lunar orbit, 3784 $\frac{km}{s}$ between low lunar orbit and low Earth orbit and 6094 $\frac{km}{s}$ between low Earth orbit and the lunar surface. These ΔV's are used to design the refueling rockets. The I_{sp}'s used for the design for the hydrolox and ALICE rocket are 284.7 s and 432 s, respectively. The required exergy of production for a mass unit of propellant mass is dependent upon the mass mixture ratio, $\frac{O}{F}$. Which is 6.03 and 1.0 for hydrolox and ALICE, respectively. These ratios can differ from the stoichiometric mass mixture ratio which are 7 and 1 respectively. In the case of hydrolox, the production of this propellant from water results in excess production of oxygen. This ratio provides insight into the mass of the oxidizer and fuel of each propellant, respectively. The densities of the propellants found in literature give the volume that must be contained by a rocket structure.

To estimate the exergetic cost to place a unit mass of payload into low Earth orbit is directly related to the payload-to-propellant ratio, which is defined as the ratio of the mass of the payload divided by the mass of the total mission propellant mass. If it is known what the cost of manufacturing of both a unit mass of propellant and a unit mass of payload, this ratio can be used to give the total exergetic cost to place a single unit mass of payload into LEO. This is done by multiplying the cost of propellant manufacturing by the inverse of the payload-to-propellant ratio and then add the additional cost of payload manufacturing.

For the design approach for an initial mass estimation, a combination of methods found in literature is employed. First, a relationship between the payload mass and propellant mass was derived from the Tiolkovsky rocket equation constrained by the need for reusability. This relation is a function of I_{sp}, ascend and descend ΔV, payload mass and the structural mass ratio. From these variables, only the structural mass ratio is not a design parameter and therefore not initially known. The method employs and iterative optimization procedure. For each structural mass ratio, a propellant mass, structural mass and total mass is found. A different method can now be used to estimate the structural mass by estimating the subsystems that make up the structural mass. If both these structural masses are equal the design has converged to a solution that is capable of performing the orbital maneuvers required for the refueling operation.

The structural masses of the ALICE and hydrolox rocket are calculated using different design approaches. In the case of the ALICE rocket, an approach is taken based on Ideal Rocket Theory where the subsystem masses are estimated using payload mass, chamber pressure, temperature, material properties, rocket geometry, and the expected heat flow in the rocket chamber in addition to both the propellant mass and total mass that were obtained by guessing a structural mass ratio. The subsystem masses that are estimated are the shell mass, ablative material mass, nozzle mass, and structural mass encapsulating the payload.

In the case of the hydrolox rocket mass relations that were derived by Akin from the University of Maryland are used. These mass relations are based on regression models that use real tanks as data points for the fit from which the regression parameters are obtained. The input of these relations are again the total and propellant mass, required minimum thrust, length of the rocket, and surface area of the rocket. The subsystem masses that make up the rocket are the mass of the fuel and oxidizer tanks, the avionics mass, the fairing mass, the engine mass and structural mass encapsulating the payload. For both the hydrolox and ALICE rocket, an optimization is performed using the 'Scipy' library in Python. By iterating through structural mass ratios, two structural masses are found. At the convergence of these structural masses, the entire mass of the preliminary rocket is defined. It is known how much propellant is expelled during the mission to bring the payload to LEO, from this the payload-to-propellant ratio can be directly calculated. Now an additional layer is added to the algorithm. The effect of the diameter of the rocket on the payload-to-propellant ratio can be estimated to find find the best configuration for both rockets. It should be noted that the effect of diameter on the hydrolox rocket is weaker and less fundamental, because the geometry follows from the regression relations instead of the other way around, meaning that the mass of a propellant tank is only a function of the propellant mass and not of the geometry of that tank. The regression, therefore, assumes that spherical and cylindrical propellant tanks have the same mass. The minimization of the structural mass of the hydrolox rocket therefore mainly depends on the minimization of the surface area of the tanks for insulation mass reduction. The fairing and avionics mass are also functions of the geometry of the hydrolox rocket and scale with the surface area and the length of the rocket respectively. This length is derived from the length of the propellant tanks, the expected length of the engine and avionics and the length of the payload structure, which is modeled in the same manner as the propellant tanks since the payload that is being transported is propellant. The ALICE model which depends on IRT is more strongly influenced by the change in diameter. The change in diameter is most strongly related to the heat flow, radiation cooling capabilities, and thickness of the combustion chamber shell. According to the thin-walled vessel equations the thickness of a shell scales linearly with an increase in diameter, this means that for larger diameters the shell has a higher mass, and this increase in mass is exponential considering that more propellant is needed due to the increase in mass. On the other hand, an increase in the diameter of a combustion chamber reduces the heat flow to the chamber wall and also increases the radiation surface area which means that thermal control poses fewer challenges. Passive radiation cooling is not an option because the very large diameter of the rocket would increase the structural mass of the shell to a point where the efficiency of the mission is not interesting any longer. This means that an ablative material is used to mitigate the heat flow to the chamber wall thereby protecting the structural integrity of the rocket. An optimum can be found given that an ablator is used, the chosen ablator is however not manufactured on the Moon meaning that the ablative material should be taken from Earth which makes the current configuration unattractive. This process of iteratively guessing a structural mass ratio for a range of diameters is done to obtain estimates for the payload-to-propellant ratio of both the ALICE and hydrolox rocket. Considering that ALICE, oxygen and hydrolox are chosen as payloads for the LEO propellant depot, optima for these three payloads are calculated for each rocket type. The resulting payload-to-propellant ratios for the hydrolox rocket are 2.93 %, 2.87 %, and 2.24 % for ALICE, oxygen, and hydrolox payloads, respectively. For the ALICE rocket, these are 2.23 %, 2.17 %, and 1.89 %. The difference in efficiency between the payloads is due to the difference in structural mass required to encapsulate the substances, which is a function of den-

sity and number of tanks and payload mass, which is kept constant. ALICE has a higher density than liquid oxygen and liquid hydrogen, and also requires no insulation to prevent boil-off. Liquid oxygen has a density that is about 16 times as high as liquid hydrogen which partly explains why the gap between hydrolox and oxygen is much larger than between oxygen and ALICE. An additional factor in the case of hydrolox is the fact that the payload structure needs two separate tanks for the transportation of the liquid oxygen and liquid hydrogen which make this option the least efficient in terms of the PTP-ratio. Even though ALICE has the best PTP-ratio it should be kept in mind that the I_{sp} of this propellant is much lower than that of methalox or hydrolox. The relatively low ratios are due to the constraint that the spacecraft ought to be fully reusable, which requires the tanks to carry more propellant for the round trip. The propellant is deposited at the LEO depot which orbits the Earth at an altitude of 420 km. This propellant depot is subjected to a drag force because at this altitude the atmosphere still has a very low density between about $0.5-6\cdot10^{-12}$ $\frac{kg}{m^3}$ depending on the solar cycle. The solar cycle is a periodic cycle of 11 years where the solar activity changes, here a maximum value of $6\cdot10^{-12}$ $\frac{kg}{m^3}$ was used. The density of the upper atmosphere is a function of this cycle. The drag that the depot is subjected to needs to be counteracted to prevent orbital decay. A model is made that links the density and mass of a given propellant to the shape of a propellant depot. By doing this an estimate of the drag force can be obtained. Equating this drag force to the force that can be generated by a krypton ion thruster, allows for the calculation of the required power and mass flow rate and thus the yearly power mass and consumption of krypton for the orbital station-keeping of the propellant depot. For a constant propellant mass, the drag surface area of the propellant depot is a function of density, therefore propellants with higher densities require less krypton for station-keeping per unit mass. Furthermore, an increase in total propellant mass results in a lower requirement of krypton per unit mass propellant because the mass flow rate scales with the propellant mass at a rate of $m_{prop}^{\frac{2}{3}}$, which means that doubling the propellant mass increases the krypton requirements by a factor 1.59. Exergy is a useful tool to estimate the extractable useful work of a system and can be divided into chemical, thermomechanical, potential gravitational, and kinetic exergy. Exergy of gravitational and kinetic exergy will not be looked into. The calculation of chemical exergy depends either on mixing when the substance is present in the environment or on a hypothetical reaction of the substance with a molecule in the environment. When looking at solids that are also present in the lithosphere, Szargut has proposed a method that was used to estimate the chemical exergy of mixing. The thermomechanical part can be calculated when the temperature and pressure of the environment and system are known by using the corresponding entropy and enthalpy that were found in the thermodynamic tables. By applying the exergy analysis to the processes for the synthesis of ALICE and hydrolox the exergy input, output and destruction can be determined and used to get a better understanding of the power requirements of propellant-generating architecture on the Moon. The lunar environment is a harsh one. This is due to the lack of an atmosphere and a magnetic field as well as the long lunar day-night cycle. The lack of a magnetic field makes radiation a big problem for electronics and human safety. Big temperature swings are expected because the lunar surface cannot contain the heat that the sun provides and is quickly lost to space when not illuminated. Across the lunar surface, this varies between 40-350 K which is strongly dependent on the latitude and the moment of the lunar day. For the manufacturing of both of the propellants water is required. Evidence for the presence of water at the lunar South pole makes the construction of a lunar base near the pole an interesting endeavor. Water is only present in Permanently Shadowed Regions such as craters. The South pole has another interesting property, due to the elevation of certain parts near the Shackleton crater solar power can be captured up to 85 % of the year, these so-called Peaks of Eternal Light in combination with the presence of water make deployment near the South pole a good choice. The temperature and pressure in the PSRs are 40 K and $3\cdot10^{-15}$ bar, respectively. The composition of the regolith should also be looked at since the aluminum required for the ALICE propellant will be extracted from this regolith. Lunar samples that were brought back during the Apollo program give indications of the mineralogical composition of the regolith. Three types of regolith compositions were defined, namely highlands regolith, low-Ti mare regolith, and high-Ti mare regolith. The composition of all three types is roughly the same the differences are mainly found when looking at the iron, titanium, and aluminum concentrations. In the case of the South pole, highlands regolith combined with a 5.6 % water concentration is taken as the composition of the PSR. Furthermore, values of the thermodynamic properties of regolith and water, such as heat capacity, enthalpy and entropy are collected from JANAF, NIST, and other literature to be able to estimate the required exergy for the processing of the regolith into useful products. To be able to estimate the exergy flow from excavation to propellant, one should look at the exergy inflow into a system and the exergy outflow outside the system, this then allows for the calculation of the destruction and efficiency.

Radiation is the biggest form of heat transfer on the Moon and makes the efficient design of processes difficult. Considering that radiation scales with temperature to the fourth power and the operating range of the processes that will be considered are between 40-2250 K high losses can be expected for high-temperature processes, if not mitigated. For a radiating body with an emission coefficient of 1, the expected loss varies greatly depending on the temperature with a range of 900 $\frac{kW}{m^2}$ to only 0.1 $\frac{kW}{m^2}$ between 2000-200 K and then continues to 0 net radiation at 40 K.

In order to process the regolith and generate useful products from them, it first needs to be collected. Multiple excavation processes have been proposed such as pneumatic drills, bucket drums, and bucket wheels. Operating in a low-gravity environment poses challenges because the lower normal force reduces the grip between the excavator and the lunar surface. Also, many techniques require liquids or gas for cooling or operation, which are not present in the lunar environment. The first 30 cm of the lunar soil is relatively loose and does not require pneumatic drilling to loosen up the lithosphere. A proven concept at a high enough TRL is the RASSOR excavator from NASA. The simultaneous excavation of multiple bucket drums operating at the same that turn in opposite directions counteract each other's force and allow for a low mass excavator because a lower normal force is needed. Also, this excavator has been tested in icy settings and has had sufficient results that indicate that it would be capable of operating in the icy environment of the PSR. An energy consumption for the excavator of 2.74 kJ per kg of regolith can be found in the literature. From an exergetic point of view excavation is very inefficient because all of the exergy that is put into the system is lost since the available work after excavation is 0 because the regolith is in chemical and thermomechanical equilibrium with the environment, this equilibrium condition is called the dead state.

This icy regolith must then be heated such that the water can be separated from the regolith. Heating the regolith results in the sublimation of water because at the very low pressure of the lunar environment, water cannot exist in liquid form. The heat that is required for the heating and sublimation of the regolith and water can be estimated by taking the average heat capacity of a temperature gradient between two temperatures multiplied by that gradient. This can be used to calculate the exergy by multiplying it by the Carnot efficiency term. The water vapor is now compressed to liquefy it such that it is usable for electrolysis. The exergy input, output and destruction of the heating and sublimation process of the icy regolith is 311 $\frac{kJ}{kg}$, 167.4 $\frac{kJ}{kg}$, and 152.8 $\frac{kJ}{kg}$, respectively. Unsurprisingly, much of the exergy is lost because the heated regolith is discarded. The values presented are for the processing of 1 kg of icy regolith, this is equivalent to a water yield of 56 g.

The water vapor was heated to 87 $°C$ and isothermally compressed to 2 bar before continuing to the electrolyzer. The isothermal compression of the water vapor requires electrical work to be performed by the compressor. Current compressors have efficiencies of about 90 %, however when looking at the exergy output, input, and destruction of the compressor these values correspond to 361.9 $\frac{kJ}{kg}$, 54.6 $\frac{kJ}{kg}$ and 307.3 $\frac{kJ}{kg}$, respectively. The exergy destruction is in the order of 85 % which is understandable considering the enthalpy of the system decreases due to the loss of exergy during the phase change and the mechanical work used for the compression.

A variety of electrolyzers are currently in use, from these, the Proton Exchange Membrane electrolyzer was selected because it has some useful characteristics. It is a compact, low-maintenance, low-pressure, high-efficiency electrolyzer, a disadvantage however is the need for expensive materials that require replacement after some time. Currently in use, PEM electrolyzers have demonstrated an exergy efficiency of 65 % when looking at the chemical exergy of the chemical reaction based on the Gibbs free energy. The exergy input, output and destruction are 1223 $\frac{kJ}{kg}$, 752.8 $\frac{kJ}{kg}$ and 470.4 $\frac{kJ}{kg}$. Even though this process has the highest exergy input, it is not inefficient. The hydrogen and oxygen are collected after the electrolysis and redirected for cooling and liquefaction.

The PSR environment allows for the passive cooling of oxygen and hydrogen. The hydrogen is cooled to 40 K, at this point about 10 % of the hydrogen is orthohydrogen, at room temperature this is 75 %. This is important since the two spin isomeres of the hydrogen, so-called ortho, and parahydrogen, have different energy levels. If rapid cooling from room temperature occurs much more energy is released during the ortho-para conversion compared to the cooling from 40 K. This difference makes liquefaction more exergy efficient. The liquefaction of hydrogen happens through the Joule-Thomson (JT) effect, this highly entropic effect occurs when a real gas is pushed through a throttling valve that causes a rapid decrease in the pressure. When pushed through this valve the temperature of the gas can increase or decrease depending on whether the gas is below or above the inversion temperature. For hydrogen and helium, this is at a very low temperature. Normally

the hydrogen needs to be precooled by nitrogen to reach the inversion temperature after which it can be used for liquefaction. This nitrogen precooling system is not required on the Moon because passive radiation cooling can cool the hydrogen below the inversion temperature. For the liquefaction of the hydrogen the Linde-Hampson cycle was selected which consists of a compressor, heat exchanger, JT throttling valve and a reservoir. All the energy input comes from the isothermal compression of the hydrogen, after the isothermal compression the heat exchanger cools the hydrogen further before it goes through the valve after which the hydrogen is partly liquefied and partly remains gas at a lower temperature, the liquid is stored and the gas is pumped back through the heat exchanger for cooling. The oxygen also experiences exergy destruction from cooling to 94 K. The exergy input, output, and destruction of passive cooling and the liquefaction and ortho-para conversion process are 855.1 $\frac{kJ}{kg}$, 808.5 $\frac{kJ}{kg}$ and 46.7 $\frac{kJ}{kg}$. The chemical exergy related to the chemical reaction of oxygen is considered here, to get a better understanding of the exergy destruction without the chemical exergy gives the values, 153.1 $\frac{kJ}{kg}$, 106.5 $\frac{kJ}{kg}$ and 46.7 $\frac{kJ}{kg}$. This is for the liquefaction of 6.2 grams of hydrogen and 49.8 grams of oxygen.

Storage of hydrogen and oxygen can be done passively, the very low radiation and complete absence of convection make it possible to store oxygen and hydrogen for long periods of time in the PSR environment. During the liquefaction of hydrogen, it was cooled to a lower temperature than strictly required, this means that the hydrogen can absorb heat without changing phase, the rate at which this happens is a function of the mass, density, and surface area of the tank in addition to the temperature of the environment, hydrogen and the tanks emission and absorption. For an emission coefficient of around 0.15 a big oxygen tank should be able to store oxygen for a year in the PSR environment, during this time the oxygen would only decrease 3 K. The substantial enthalpy difference for a 1 K temperature increase and the very low temperature of hydrogen and the environment make the passive storage of hydrogen without large amounts of hydrogen possible in the PSRs for an extended period. When needed the oxygen and hydrogen can be transferred into the propellant tanks of the refueling spacecraft.

In the case of ALICE production, regolith is collected and used to make a MRE reactor, this reactor uses a part of the regolith as a heat shield against the molten core. The molten regolith is subjected to different voltages and current strengths in a subsequent manner, this way iron oxide, silicon oxide, titanium oxide and aluminum oxide are electrolyzed one after the other which should prevent the mixing of the molecules. Given that an effective method is used to prevent radiation loss, the power consumption of this process is divided into three parts, the endothermic heat required for the electrolysis, the energy needed to split the molecules in their respective elements and the heat required to increase the temperature and make the regolith change phase. After the electrolysis process, oxygen and metals can be extracted. The yield of 1 kg of regolith is expected to give 188 g, 91 g, 46 g, and 417 g of silicon, aluminum, iron, and oxygen respectively. The MRE reactor uses the temperature gradient through the regolith where the core is molten and the wall is solid, this way the structural integrity of the reactor can be maintained without the use of materials that would have to contain very high-temperature material.

The two main components that we are interested in are oxygen and aluminum because they are used in the propellant and the payload of the mission. The oxygen is filtered out of the vapor that resulted from the heating and subsequent electrolysis of the regolith. This is done by means of a YSZ separator. They offer high ionic conductivity, mechanical strength, and chemical stability, making them valuable in high-temperature electrochemical devices and lunar architecture. To estimate exergy flow and calculate the required electrical work for separation.

To manufacture aluminum nanopowder for the ALICE rocket propellant, there is a trade-off to consider regarding combustion. An aluminum oxide layer is added to prevent instant combustion when the particles come in contact with water. As the particle diameter increases, the relative volume and mass of the oxide layer decrease. For example, with a 2 nm oxide layer thickness, the percentage of non-reactive aluminum oxide is 2 %, 8 %, and 20 % for particle diameters of 80 nm, 200 nm, and 1000 nm, respectively. Maintaining a 2nm oxide layer thickness is essential to prevent spontaneous combustion by preventing aluminum reaction with water. Consequently, larger particle sizes have a higher percentage of combustible aluminum.

However, larger aluminum particles also have drawbacks. They exhibit slower combustion, which can result in incomplete combustion before the particles exit the combustion chamber. Therefore, achieving an optimal particle size is crucial to balance the reactivity of aluminum, ensuring efficient and complete combustion of the ALICE rocket propellant.

For the use of aluminum as a propellant in the grain, nanoparticles are required for the effective combustion of the propellant. Therefore a method was selected. Multiple methods have been proposed for the manufacturing of aluminum nanoparticles. These methods include mechanical ball milling, mechanochemical synthesis, exploding wire, solution reduction, gas-phase synthesis, liquid-phase synthesis, and laser ablation. Each method offers distinct techniques to control the size, morphology, and properties of the aluminum nanoparticles. These methods provide flexibility in nanoparticle production for various applications in industries such as metallurgy, materials science, and chemical engineering. The pulsed laser ablation (PLA) method is known for its ability to produce aluminum nanoparticles with a narrow size distribution. The process involves the evaporation of the target material and the hydrodynamic expansion of the ablated plume into the ambient gas. Nanoparticle formation occurs through homogeneous nucleation and particle growth, where supersaturated vapor atoms form critical nuclei that capture atoms on their surfaces and transition into larger particles.

Using the laser ablation method with argon gas as the ambient gas, researchers have found that controlling the ambient gas temperature allows for control over the particle size. Introducing ethylene to the argon quench flow enables the coating of aluminum nanoparticles with carbon, resulting in an average mobility diameter of 80 nm.

Investigations of nanoparticle generation during laser ablation of various metals (Ni, Al, W, and stainless steel) in both ambient air and argon gas have revealed differences in size distribution and number concentration. The number concentrations of generated nanoparticles in argon gas were up to 100 times higher than those produced in ambient air.

Due to its narrow size distribution and capability to produce 80 nm aluminum nanoparticles, along with its continuous operation without the need for material replenishment from Earth, the laser ablation method is selected for the production of aluminum fuel particles.

To meet power consumption needs, two main options are available: solar energy conversion and nuclear energy. Solar power can be harnessed using solar concentrators and photovoltaic cells for generating both heat and electricity. On the other hand, the nuclear option involves nuclear reactors and Radioisotope Thermoelectric Generators (RTGs). Both approaches offer viable solutions for meeting power requirements in various systems.

The US invested in space fission power through the SNAP program but faced challenges due to complex approaches. Launch failures and power requirements for space applications posed difficulties. NASA's Kilopower project is developing KRUSTY (Kilopower Reactor Using Stirling Technology) to address these issues. KRUSTY prototypes, with energy output based on reactor mass, are being researched and developed. Components include a titanium/water heat pipe radiator, Stirling power conversion, sodium heat pipes, and tungsten/lithium heat shielding.

The KRUSTY reactor is a highly efficient power source for space usage. It utilizes a uranium-molybdenum alloy as fuel and is surrounded by a beryllium oxide reflector, which prevents neutrons from escaping and sustains the nuclear reaction. The reactor produces radioactive energy that is converted into both electric and thermal energy. The power density of the reactor is significantly higher than that of traditional photovoltaic systems, with values of 190 $\frac{\mathrm{W}}{\mathrm{kg}_{^{235}\mathrm{U}}}$ and 1220 $\frac{\mathrm{W}}{\mathrm{kg}_{^{235}\mathrm{U}}}$.

One of the main advantages of the KRUSTY reactor is its ability to provide reliable year-round power, making it an attractive option for space applications. Unlike solar panels, the reactor's efficiency does not decrease over time. It can supply both heat and electrical power to In-Situ Resource Utilization (ISRU) systems, allowing for various applications in space. However, it should be noted that the radioactivity related to this technology poses challenges during launch, landing, and operation, which need to be carefully addressed.

Solar concentrator mirrors are a technology used to enhance the efficiency of solar energy collection by concentrating sunlight onto a smaller area, increasing its intensity. This allows for more effective capture of solar energy and can significantly boost the power output of solar systems. These mirrors find applications in solar thermal power plants and concentrated photovoltaic systems, contributing to the advancement of sustainable energy solutions.

The performance of a solar concentrator system is influenced by the temperature of the thermal reservoir. As the temperature increases, both energy and exergy efficiency decrease, while higher concentrator ratios im-

prove efficiency. Interestingly, the energy and exergy efficiency tend to converge as the temperature rises. At lower temperatures, the behavior of exergy efficiency differs from energy efficiency. Exergy efficiency starts at 0 and gradually increases, while energy efficiency reaches a peak and then declines. This behavior can be attributed to the characteristics of the Carnot cycle. At low temperatures, the maximum efficiency of the Carnot cycle is close to 0. With increasing temperature, the maximum work that can be extracted from a heat reservoir increases, but so does radiation. At a certain temperature, an optimal combination is reached, beyond which further increases in radiation would reduce efficiency. Decreasing the temperature would decrease radiation, but the reduction in Carnot efficiency would outweigh the benefits, leading to a decrease in overall efficiency.

In recent decades, advancements in technology have opened up possibilities for more efficient and reliable energy sources. Solar cells, especially, have garnered attention for their potential in space applications, benefiting from the consistent availability of solar power. However, the inclusion of necessary infrastructure for mounting and operating solar cells reduces their specific power.

Solar cells operating in space face a significant challenge posed by continuous cosmic radiation, which damages the cells and reduces their efficiency. This challenge is more severe in space compared to Earth, as Earth's magnetic field diverts particles towards the poles, while high-energy particles from the sun reach the lunar surface due to the absence of a magnetic field. The severity of cosmic radiation events can impact the efficiency of solar cells, with constant exposure to weak radiation leading to an annual efficiency reduction of approximately 2-3 %.

Solar radiation also presents a significant challenge in the form of strong proton events (SPEs), resulting from solar storms and the ejection of solar mass. These high-energy particle plumes can cause damage to electronics and hardware in space. Monocrystalline silicon solar cells may experience efficiency reductions of 20-25 %, while multi-junction cells could see reductions of 5-10 %, due to ionized particles.

It is crucial for lunar architecture and space systems to be designed to withstand the occurrence of SPEs. This can be achieved through radiation shielding or implementing protective measures to safeguard hardware and electronics during such events.

The exergy input for producing and transporting propellants was calculated using the inverse of the payload-to-propellant ratio. Comparing the ALICE and hydrolox rockets, it was found that the ALICE rocket had lower efficiency in payload-carrying capacity. This can be attributed to the lower density of hydrogen and the need for two tanks as oxygen and hydrogen are both transported, requiring larger and more numerous tanks.

Furthermore, the specific impulse, which affects rocket performance, is influenced by the choice of propellant that is placed in the depot. While ALICE is easier to transport to LEO, the higher specific impulse of an alternative propellant might make it a more favorable option overall.

In terms of versatility, the oxygen payload can serve as an oxidizer for multiple propellants, making it compatible with a wider range of rocket systems. This flexibility gives the oxygen payload an advantage over other propellants.

Further research is needed to understand the lunar environment and develop specialized equipment for lunar conditions. Location on the lunar surface greatly impacts solar energy availability, operating conditions, and mineral composition.

Radiative losses pose a challenge in lunar power systems, especially for solar concentrator mirrors used for regolith heating. Radiation-induced energy losses make certain operating temperatures unfeasible, emphasizing the importance of considering and mitigating radiation losses in system design.

Production of ALICE and hydrolox propellants requires significant exergy input. MRE reactors can produce multiple metals for in-situ resource utilization (ISRU) with minimal equipment from Earth. Hydrolox has an advantage in terms of exergy input per kg of propellant.

Solar radiation and Strong Proton Events can reduce the efficiency of PV cells, which is difficult to mitigate as they rely on solar radiation for electricity generation. Hydrolox propellant shows better performance compared to ALICE.

Subsystem masses for hydrolox rockets are weakly related to rocket shape, requiring a different approach for

specific designs. Ablative material poses a trade-off between diameter, shell thickness, and mass. Manufacturing ablative material on the Moon reduces reliance on Earth supplies for the expensive ALICE rocket.

The expected payload-to-propellant ratios for fully reusable two-stage ALICE and hydrolox rockets are around 2.50-2.96% and 3.13-3.84% respectively, making hydrolox more efficient. The exergy input for transportation of 1 kg of payload is one order of magnitude lower for hydrolox compared to ALICE.

The research conducted on regolith processing demonstrated the generation of various components from the process. Specifically, the water electrolysis process yielded 6.2 g of hydrogen and 49.8 g of oxygen, which corresponded to 43.7 g of hydrolox and 12.3 g of surplus oxygen with an exergy input of 38 MJ. In the case of the ALICE production process, the yield comprised 100 g of nano aluminum particles for fuel, along with byproducts consisting of 406 g of oxygen (from the MRE reactor), 188 g of silicon, and 46 g of iron. Notably, the addition of 100 g of water resulted in the production of 200 g of ALICE propellant. The entire ALICE production process required an exergy input of 508 MJ.

The overall exergy input to bring one kg of propellant into LEO depends on the rocket system and propellant that is being transported. For the ALICE rocket, this is 23.3, 23.4, and 26.9 $\frac{GJ}{kg}$ for ALICE, oxygen, and hydrolox, respectively. The difference between the least and most exergy-consuming process is 15 %. For the ALICE rocket, this is 1.81, 1.32, and 1.64 $\frac{GJ}{kg}$ for ALICE, oxygen, and hydrolox, respectively. The difference between the least and most exergy-consuming process is 37 %. The exergy consumption of the processes in the ALICE rocket remains relatively consistent, as the exergy required for manufacturing the propellant greatly outweighs the influence of payload manufacturing. On the other hand, the exergy consumption of the hydrolox rocket exhibits a larger range, being approximately one order of magnitude less costly than the ALICE rocket. Additionally, the choice of payload has a more significant impact on the overall exergy input for the hydrolox rocket.

Oxygen remains a good option for propellants due to its abundance in space, transportation efficiency, and versatility in various propellant systems. It also requires a smaller propellant depot.

To enable more efficient and effective lunar missions, several key areas of research and development have been identified.

Firstly, spacecraft performance optimization is essential. By analyzing the spacecraft's trajectory and considering the forces acting upon it in the Earth-Moon reference frame, it is possible to enhance performance during the decoupling phase. Utilizing advanced methods in orbital mechanics, precise calculations of the required ΔV's can be made, ensuring efficient maneuvers.

Secondly, the improvement of ALICE propellants is crucial for enhancing their specific impulse. By increasing the specific impulse, which measures the propellant's thrust efficiency, higher thrust can be achieved while reducing propellant mass. This research aims to improve the efficiency and effectiveness of ALICE propellants, enabling long-duration space missions.

Furthermore, the design and optimization of propellant depots in low Earth orbit require detailed consideration. Factors such as shape, drag, and accommodation of multiple propellants within the depot need to be taken into account. A comprehensive design process will facilitate the establishment of reliable and efficient methods for storing and accessing propellants in space.

The lunar environment presents unique challenges and opportunities for resource extraction and utilization. Research on selective approaches for mining regolith, such as utilizing higher pressures to melt water instead of sublimation, can improve efficiency and reduce energy requirements. Investigating thermodynamic properties of regolith and developing effective strategies for resource extraction will enhance our understanding of the lunar environment and enable sustainable exploration and development.

Specifically, refining the separation of metals from molten regolith mixtures in MRE reactors is recommended to optimize the process. This will facilitate efficient extraction of pure metals for use in various applications.

To maximize energy potential, updating the values for standard chemical exergy based on a deeper understanding of lunar mineral distribution is proposed. This will provide a more accurate assessment of useful work that can be extracted from lunar substances, considering location-specific temperature and pressure.

Moreover, alternative methods for lunar aluminum production should be explored. Developing novel techniques for manufacturing aluminum on the lunar surface will overcome challenges associated with extrater-

restrial manufacturing, such as limited resources and harsh environmental conditions. This research aims to achieve more efficient and cost-effective methods for future space exploration and habitation missions.

Lastly, conducting comprehensive trade-off analyses will aid in selecting appropriate power systems for specific lunar applications. Considering factors like energy output, efficiency, cost-effectiveness, and technological feasibility, along with unique requirements and constraints, will guide decision-making and ensure sustainable energy generation and utilization on the Moon.

By addressing these research areas, we can advance our understanding and capabilities in lunar exploration, resource utilization, and space mission design, enabling the long-term presence and development of human activities on the Moon.

1

INTRODUCTION

The many technological developments of the last two decades have started renewed interest in the use and extraction of space resources as well as a newly announced exploration era. After more than 50 years, it has been announced that humans will return to the Moon and are planning on staying there. The current Mars project among others is also a testimony of the exciting times that are ahead of us. A major problem regarding all space missions is 'the tyranny of the rocket equation', this equation that was derived by a Russian scientist in the 19th century and is the most fundamental equation regarding rocket design and behavior. The equation looks like this:

$$M_p = M_0 \cdot \left(1 - e^{-\frac{\Delta V}{v_e}}\right) \tag{1.1}$$

Where M_p, M_0, ΔV and v_e are propellant mass, initial total mass, stage ΔV and exhaust velocity of the spacecraft respectively. An alternative form is given by:

$$\Delta V = v_e \cdot ln\left(\frac{M_0}{M_f}\right) \tag{1.2}$$

Where M_f is the final mass and equal to the difference between initial mass and propellant mass. The equation uses the Euler number named after the legendary mathematician Leonhard Euler to a certain power, which means it is an exponential function. The equation states that as the ΔV, which is a mission characteristic that captures the impulse change of a spacecraft for a maneuver, rises $(1 - e^{-\frac{\Delta V}{v_e}})$ increases which means that the propellant also increases, if the propellant mass is kept constant, the m_0 term can compensate by decreasing which means that a smaller payload can be carried. The exponential nature of the equation makes transporting payload an increasingly expensive and propellant-consuming endeavor. This payload problem has spiked interest in the use of something that is called In-situ Resource Utilization or ISRU. The basic idea of ISRU is to use the resources that are available in space. Ever since the beginning of space exploration the use of space resources have been proposed because of the difficulty of mass transporation. The use of methods to extract metals for ISRU purposes is essential for an independent base in the solar system. The applications of ISRU are numerous and diverse. The extracted materials can be used for the further construction of a base in terms of thermal control, structural support, radiation shielding, among others. Also, vital consumables such as water and oxygen ought to be present for sustained human presence. Nitrogen and carbon are not present in meaningful amounts on all celestial bodies, which is a major problem for humans considering aminoacids and human tissue are dependent upon these. In addition to supporting the upkeep and expansion of a space station, space mining has the potential to offer valuable resources that are scarce on Earth, such as Helium-3, a fuel source for fusion reactors, and Rare Earth Metals (REM's) which are critical components in the production of highly sought-after electronic devices such as cellphones. The problem regarding the payload and propellant in combination with the ISRU method gives rise to the question whether we could make in-space propellant to refuel rockets and thereby inevitably reduce their GLOM (Gross Lift-Off Mass) for the same payload. Currently many rockets use hydrolox, which is a hydrogen, oxygen rocket because of the very high exhaust velocity of the hydrolox products. Another propellant that is gaining interest is methalox , which consists of methane and oxygen. The thermal and technological difficulties of storing hydrogen and oxygen at cryogenic temperatures begs the question whether the use of another propellant might

be interesting for in-space refueling. The LCROSS (Lunar Crater Observation and Sensing Satellite) mission has provided strong indications of the presence of water on the Moon in interesting quantities. This water can be used for human consumption but it is also an opportunity for the manufacturing of ALICE (aluminum-ice) and hydrolox, which are both rocket propellants that require water or its elements. The aluminum that is required for the ALICE has been found in aluminum oxide that the lunar regolith partly consists of.
To access the feasibility of an in-space mission it is important to know the energy that goes into it. For assessing the efficiency of the energy conversion, an exergy analysis can be done, this method provided insight into whether a net loss of available energy has occurred between the beginning and end of a process. Some processes for example can be exergetically very inefficient whereas one could argue that energetically not much has happened. Consider a dam for example in Figure 1.1. Even though the water level before passing the dam is constant, which means the potential gravitational energy is constant, the exergy or useful work that can be extracted is strongly dependent on the other side of the dam, thus the environment. A system can yield varying exergy outputs for an equal amount of energy.

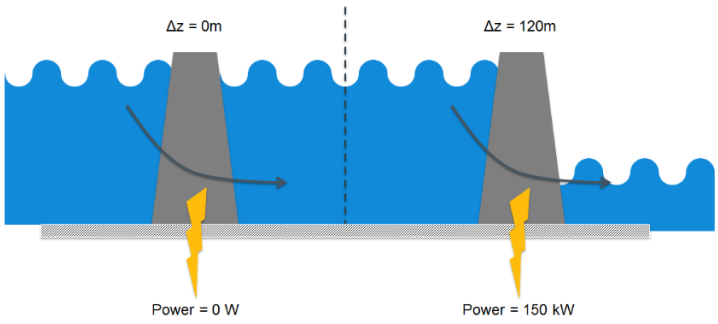

Figure 1.1: Difference in exergy output between two outflow water levels for the same inflow water level [20]

The question that remains to be answered is, what is the exergy input and destruction related to the synthesis and transportation of propellant to low earth orbit.

An exergy analysis through the entire process of the extraction and formation of the propellants in combination with the efficiency of the reusable rocket system that ought to transport the payload to LEO, provides insight into the architectures power requirements, capabilities of metal extraction, exergetic cost of transporting propellant and useful payload to consider for transportation.

To research this topic, the following steps are taken:

1. Identify the lunar environment in terms of resources, thermodynamic properties, potential sources of power, and ambient conditions.
2. Select possible technologies that can be used for the production of the desired propellants.
3. Collect estimates regarding the thermodynamic process and power and heat input to get an understanding of the exergy flow and efficiency of the respective processes.
4. Identify byproducts of the regolith processing that are considered as a beneficial factor of a specific architecture.
5. Select preliminary rocket design methods to estimate the payload-to-propellant ratio of the mission for each propellant.
6. Estimate the propellant requirements for the transportation of oxygen, hydrolox, and ALICE payloads for both cases where the rocket is propelled using either ALICE or hydrolox.
7. Combine the exergy requirements for manufacturing with the payload-to-propellant ratio of the rockets to acquire insight into the total exergy requirements for propellant insertion into LEO.

The hydrolox and ALICE rockets will transport oxygen, hydrogen and ALICE respectively. The corresponding payload-to-propellant ratio for each rocket and propellant combination can be used to investigate what the

entire exergy input of the processes to bring the propellant into LEO is.

2

Literature Review

2.1. Lunar Environment

The lunar environment is a harsh waste land that lacks an atmosphere and mainly consists of a variety minerals this is based on the lunar rocks that were brought back from the Moon during the Apollo program [18, 61]. These minerals are plagioclase, pyroxene, olivine, and ilmenite [91]. Interestingly two interesting new minerals have been found. These minerals are Armalcolite, named after the Apollo astronauts and pyroxferroite [60], which are titanium-iron and high-iron minerals. The composition of the regolith however can be described by combining different concentrations of the first four minerals mentioned above. It is known that the composition of the regolith is, but the lack of lunar rock that has been brought back from the Moon over the last 70 years makes it very difficult to accurately determine the exact chemical makeup of the specific soil that will be processed. Some interesting locations such as the Shackleton crater near the South Pole [55] have not yet been mineralogically analyzed to be able to make strong claims, however, currently, it is thought to most strongly resemble highlands regolith[77]. The lunar night and day cycle is a factor to consider when operating on the Moon since lunar PELs (peaks of eternal light) are only present around the lunar south pole [55]. A full night-day cycle takes 29.5 Earth days[4] meaning that systems relying on solar radiation cannot be operated all the time but only in periods of 14 consecutive days. Another problem that is related to the short periods of illumination and following darkness is the extreme temperature swings that they bring about.

2.2. Power Systems

Nuclear energy is interesting for space use because it provides both heat and electricity to lunar systems. KRUSTY is the only bigger nuclear reactor that has been developed over the last years, the problems for the development of reliable nuclear reactors have been persistent over the last decades with only recent breakthroughs in the field [73]. Notable about photovoltaic cells and solar concentrators is the large mass injection and the degradation due to dust and radiation and the lunar day-night cycle. Radiation of in-space systems is a problem that requires attention because it damages both the circuitry of electronic systems as well as the health of humans that would go into space. A reliable method for the permanent presence in a space environment is yet to be discovered. In general thermodynamic properties of most molecules have been documented really well especially in the range of 100-2000 K.

2.3. Rocket System Design

To be able to assess the performance of rocket systems the characteristics of the propellants are needed. Hydrolox is a widely used rocket propellant of which the characteristics are well-documented, the new Vulcain 2.1 that is being developed by the Ariane group has a vacuum I_{sp} of 432 s for a mass mixture ratio of 6.03 and a length of 3.7 m and an area ratio of 61.5 [5]. ALICE is a rocket propellant that is not currently used in big rockets and needs further research. Rocket engines using this propellant or a variation of this propellant have been reported to have I_{sp} ranging from 170-314.7 s [75]. It should be noted that some Aluminum-Ice propellants have a better specific impulse than pure aluminum and water, for example, aluminum peroxide and water, aluminum hydride and water and aluminum hydride and peroxide. Also, the exact composition of the

ALICE propellant such as mass fraction of additives such as iron or other substances has not been extensively researched, theoretically ALICE should be able to provide an I_{sp} above 300 s with an expansion ratio of 100, and a mass mixture ratio of 1.2 [76]. Further research and optimization of ALICE rocket engines is needed to reach the potential of the propellant.
The development of rockets is a highly iterative process whereby the system masses are optimized to synthesize a design. In general, rockets can be split up into multiple groups depending on the mission. They can be categorized as solid rockets, liquid rockets, and ion or electric propulsion rockets. The thrust for the electric rocket is very low despite the very high I_{sp} the mass flow rate of this method is not sufficient for launch from celestial bodies [34]. The methods to estimate these masses depend on the depth of the design project. For preliminary estimations, the options vary from systematic engineering design of each subsystem using thin-walled vessel equations, thermal modeling, and rocket theory [1, 41, 52, 93, 107]. Other options that have been proposed focused on numerical relations that have been derived from regression analysis on real rocket data [2]. A more detailed lower-level approach to the estimation of the rocket structure is expected to better capture the idiosyncratic mission requirements.

2.4. ISRU METHODS

The development of ISRU systems in general is a difficult and slow process, multiple space companies are trying to create new devices that can operate in the harsh space environment [13, 15, 40, 48]. Considering, many devices have not yet been optimized for space use and do not exist, the use of technologies that are currently used on Earth is taken into account, keeping in mind that some approaches are not feasible due to the many complications the environment would pose. A variety of methods have been proposed for the extraction and processing of the lunar regolith into useful materials. The first step for human presence has been the extraction of oxygen, which is the reason many proposed technologies focus on the synthesis of oxygen. Since the LCROSS mission and the observations of the Chandrayaan missions that detected 600 million metrics tons of ice [14, 94] have discovered interesting amounts of water the focus has shifted more to also include water mining. Thermal mining, which is a mechanism whereby a dome is used to heat the regolith that it covers and then by heating sublimates the water contained in the underlying regolith has been proposed as a means for acquiring water in the lunar environment. Chemical reduction techniques may be a possibility such as hydrogen reduction a method that has been pushed forward by many [80, 83–85]. The low yield and many steps make the method problematic. Also, hydrogen is only present in water or in trace quantities in the lunar soil. Vapor phase pyrolysis is a method where the regolith is heated to a temperature that dissociates the molecules and starts to release oxygen. Apart from oxygen, it is very difficult to mine pure metals that can be used for construction or more specified manufacturing processes [54, 100]. Pyrolysis happens at very high temperatures meaning that a reactor that is able to contain the heated substance needs a very high thermal resistance. For the mining of purer metals and oxygen, fluorination, molten regolith electrolysis, and the FFC Cambridge method is more interesting [24, 51, 98].

2.5. STORAGE

Hydrogen and oxygen are notoriously hard to store substances, especially hydrogen. The very low boiling point of hydrogen means that heating the hydrogen results in a pressure increase that could rupture the hydrogen tank [28, 31], thermal control is therefore very important. Sometimes hydrogen is compressed and stored in a tank, this tank however needs to be thicker than one that contains cryogenic hydrogen because of the very large pressure difference, additionally compressed hydrogen only has a density of 39 $\frac{\text{kg}}{\text{m}^3}$ whereas liquid hydrogen has a density of 71 $\frac{\text{kg}}{\text{m}^3}$ [37, 49]. The hydrogen molecule is the smallest possible molecule, which means that some of the hydrogen can leak through the solid wall by slipping through the solid metal.

2.6. EXERGY

Exergy analysis is an interesting approach to studying energy systems because it focuses on the useful work that can be extracted from an energy source or system, rather than just the total amount of energy available. This means that exergy analysis provides a more accurate and comprehensive picture of the efficiency and sustainability of an energy system.

In contrast to traditional energy analysis, which considers only the quantity of energy inputs and outputs, exergy analysis takes into account the quality of energy, or its ability to do work. Exergy is defined as the

maximum useful work that can be obtained from an energy source, given its initial state and the surroundings [78].

A problem regarding exergy is that the standard chemical exergy is tabulated in literature w.r.t. the ambient conditions and composition of Earth's environment. Environments for exergy analysis that have been proposed are the lithosphere, hydrosphere, and atmosphere. For lunar purposes the use of the lithosphere seems reasonable, however, the standard chemical exergy of species is highly dependent on the composition of the reference environment, the substances present in the environment, temperature and pressure. For the calculation of standard chemical exergies the method used by Szargut can be used, however, the lack of knowledge regarding the exact reference environment makes it difficult to make claims with high certainty. The method to determine the chemical exergy scales most strongly with the temperature of the reference environment and is related to the work of mixing regarding the partial pressures of an ideal gas mixture, applied to solids [62, 82, 96].

RESEARCH QUESTIONS

Many interesting questions regarding the lunar environment, ISRU and in-space propellant manufacturing remain to be researched, for this thesis the following have been selected:

What is the exergy destruction related to logistic and technological processes for in-situ lunar propellant generation and transportation to LEO?

- What energy generation methods are feasible and reliable on the moon?
- What logistical and technological processes are possible on the moon?
- What processes are compatible?
- How much exergy is needed to obtain, transport and process the propellant?
- How much exergy is required to store each propellant respectively?
- How much exergy is destroyed during the refueling operation?

What propulsion system would be most efficient in terms of exergy for refueling operations?

- What dimensions, propellant, and technology should a refueling spacecraft have?
- What propellant is most exergetically efficient?
- What is the performance of liquid and solid boosters?
- What refueling orbit is most beneficial?

3

METHODOLOGY

The objective of this thesis is to evaluate hydrolox and ALICE rocket propellants in terms of exergy input and destruction during their creation and transportation to a propellant depot in Low Earth Orbit (LEO) such that the lunar propellant can be used by spacecraft leaving from Earth. This study involves evaluating and selecting a location on the Moon, applying data from current literature related to the composition of minerals of the lunar soil and the possible energy resources. The thesis aims to identify processes that are capable of converting regolith into rocket propellant and analyze the exergy destruction and input for the operating conditions. In addition to the generation of the propellant, the transportation of that propellant to LEO is associated with the expulsion of high amount of propellant. In general it could be said that there are two fundamental parts that should be considered to get a grasp on the exergy requirement for a LEO-depot providing propellant to spacecraft from Earth. These two subjects consist of the following:

1. Refueling rocket:
    - Patched conics approach for the estimation of ΔV requirements of the reusable two-stage rocket [107].
    - Literature study to quantify propellant characteristics such as I_{sp}, density, mass mixture ratio, temperature and pressure.
    - Algorithm derivation for an iterative process converging to a reusable rocket design by equating two different expressions for the structural mass [19, 93].
    - Mass estimation formulas for the hydrolox rocket structural mass using numerical approximations as proposed by Akin [2].
    - Structural mass estimation for the ALICE rocket using IRT (Ideal Rocket Theory) [107].
    - Analyzing the impact of different payload types on the efficiency both in terms of payload-to-propellant ratio as well as the effect on the overall exergy input.
2. Propellant production:
    - Defining and evaluating the lunar environment for extraction and exergetic purposes by using the relevant literature.
    - Identifying, analyzing and selecting propellant generating technologies in literature based on TRL (technological readiness level), mass of the system, energy efficiency, reliability, maintenance cost and additional useful byproducts that the technology provides.
    - Quantifying exergetic input, output and destruction of all the relevant subsystems of the propellant-generating process.

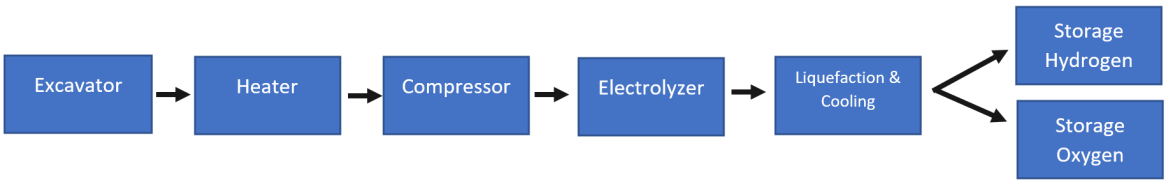

(a) Hydrolox production process

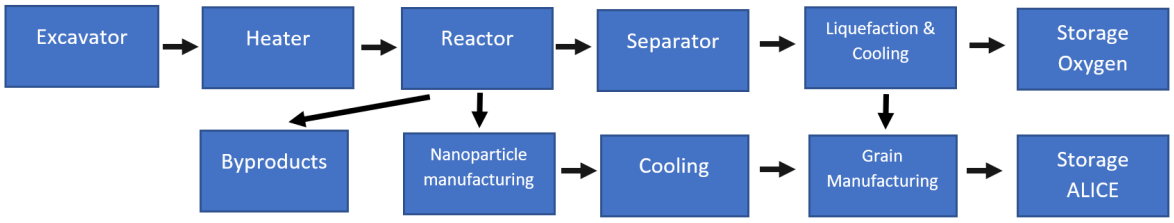

(b) ALICE production process

Figure 3.1: Propellant Production Processes

Figure 3.1 show the steps to be taken for the synthesis of the desired propellants. Figure 3.1a shows the process required for the production of hydrolox where the end products are oxygen and hydrogen. Water is extracted from the icy regolith, sublimated, compressed and electrolyzed. The hydrogen and oxygen are cooled and liquefied and the stored. Figure 3.1b depicts the process for the production of ALICE where a reactor converts the regolith into oxygen, aluminum and other materials. The separator collects the oxygen, which is subsequently liquefied and stored. The metallic byproducts are kept aside, whereas the aluminum is converted into particles, cooled and then combined with water to create a solid propellant grain.

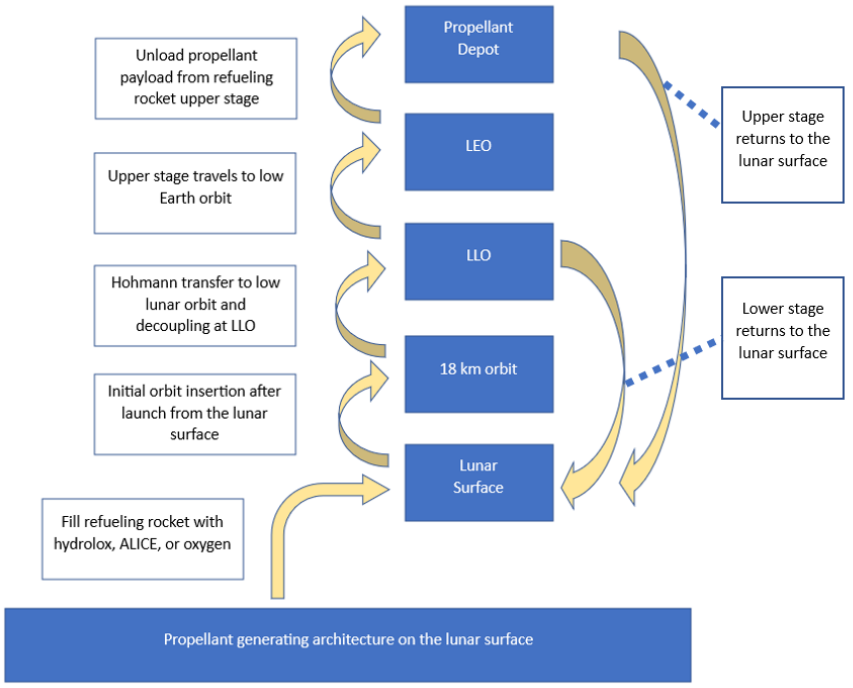

Figure 3.2: Schematic of propellant transportation

As can be seen in figure 3.2, the refueling mission consists of multiple steps. First, the spacecraft is loaded with the selected propellant, which is ALICE, hydrolox, or oxygen. Then the spacecraft is launched from the lunar surface to be placed into a low parking orbit. From this orbit, a Hohmann transfer is done to the orbit where the lower and upper stages are separated. The lower stage returns to the Moon whereas the upper stage is accelerated to a hyperbolic trajectory w.r.t. the Moon. The upper stage is parked into LEO where the propellant is transferred into a propellant depot, after which the upper stage returns to the lunar surface.

For the exergy analysis of the processes, the thermodynamic properties of the chemical substances that appear in the process are required. To this end, NIST Webbook [12] is used and provides the values for enthalpy, entropy and heat capacity among others, the values that were used in the analysis can be found in Appendix B and C. However, it should be noted that due to the lack of documented data in very low temperature environments, extrapolation from available data is necessary. In literature material properties such as yield strength, melting temperature and density will be taken in order to design a rocket that meets the requirements. The properties of oxygen are also taken into account, since a rocket only transporting oxygen could also be interesting for hydrolox and methalox rockets that are being used at the moment. The propellant architecture can be divided in a multitude of subsystems. These subsystems are power, synthesis, storage, transportation and the propellant depot. In this thesis solar concentrators, solar cells and nuclear energy will be considered as possible energy sources to power the manufacturing process. The synthesis of the desired propellant constitutes devices that are used for the excavation, separation, electrolysis, chemical reduction, powder formation, cooling, liquefaction, compression and heating. The storage of the propellant can be one of two categories, the first one is the storage of the propellant in the lunar environment whereas the second one is the storage in the propellant depot, both have to deal with storage constraints related to the temperature. In the case of the propellant depot, however, the exergetic cost for station-keeping should also be added to the exergy cost. The transportation part of the exergy destruction is directly related to the efficiency of the refueling rocket. Once a design has been selected the payload-to-propellant ratio of the rocket provides insight into the exergetic cost of propellant synthesis, transportation and storage.

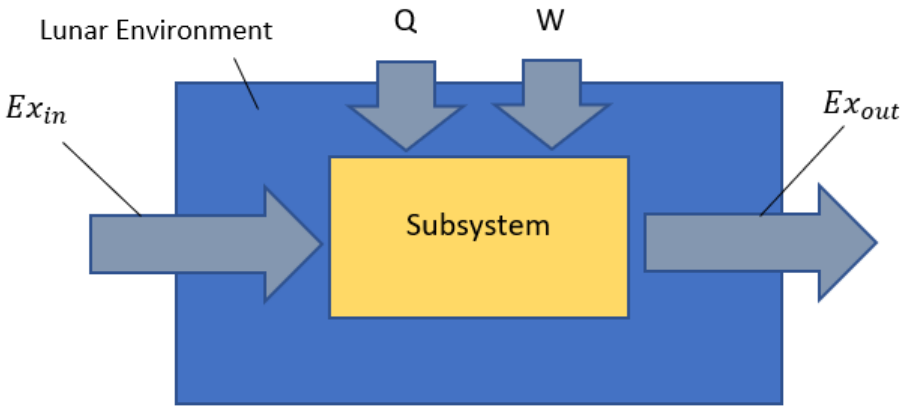

Figure 3.3: Exergy Components of a system

Power estimates can be found in the literature and then be applied to the equations in section 3.1 for each subsystem that follows the schematic in figure 3.3. For the specific chemical components such as oxygen, hydrogen, and water "NIST Webbook" will provide the required data for enthalpy, entropy, specific heat and other thermodynamic properties to calculate Ex_{in}, Ex_{out}, Q and W. For regolith, the desired thermodynamic properties are taken from the literature. The thermodynamic properties for all relevant substances in all processes should be estimated when temperature and pressure conditions are known. The exergy input for each system can be summed to find an estimate for specific exergy consumption $\frac{kJ}{kg_{propellant}}$. The sizing of the rocket system of the propellant with a reusable rocket able to transport the payload to LEO, the sizing of these rocket systems for ALICE and hydrolox is done using a combination of procedures as described in "The regolith rocket—A hybrid rocket using lunar resources" [93] and "Multidisciplinary Design Optimization of Reusable Launch Vehicles for Different Propellants and Objectives "[19]. These spacecraft will carry oxygen, hydrolox or ALICE propellant to LEO. Analyzing the payload-to-propellant ratio will provide insight in the total exergy consumption to bring a given propellant into LEO. The use of IRT (Ideal Rocket Theory), Thermodynamic Theory, and Orbital Mechanics will be used to fill knowledge gaps. Furthermore, the package 'SciPy' is used for the optimization of the procedure. After selecting the rocket systems for the refueling operations, which are sized using the Tiolkovsky rocket equation and structural mass ratio, the required propellant for the payload transportation can be calculated. Combining this with ISRU exergy destruction, the total exergy destruction of the manufacturing and refueling process can be calculated.

EXERGY

Exergy is defined as the maximum usable work that can be extracted from a system when it is being brought into equilibrium with the environment. This work can be extracted by energy conversion devices that would be able to transform the difference in energy levels in terms of thermomechanical and chemical energy into usable work. For the thermomechanical component of a system, the system is brought to the ambient state, and then for the chemical exergy, the system is brought from the ambient state to the dead state as depicted in figure 3.4. If the system state is in the ambient state, it is in thermomechanical equilibrium with the environment but could still hold chemical exergy, if this is not the case the system is in the dead state and completely incapable of generating usable work. In the dead state, ex_{dead}, a system has no exergy both thermomechanical or chemical. In the ambient state, $ex_{ambient}$, it could still hold chemical exergy. Often a system in the system state, ex_{system}, is in a different thermomechanical and chemical state than the environment and can therefore generate usable work. This means that the inequality holds: $ex_{system} \geq ex_{ambient} \geq ex_{dead}$. In the case that the system is at a lower temperature the absolute difference is taken between the thermomechanical states at the respective temperatures.

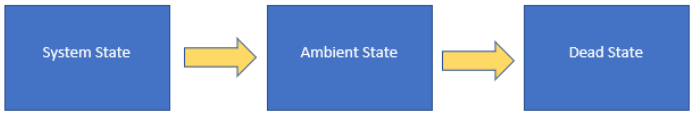

Figure 3.4: Different exergy states of a substance

The thermomechanical exergy of a system is dependent on the specific species and the pressure and temperature difference with respect to the environment. This thermomechanical component can be calculated if the temperature and pressure of both the system and the environment are known in addition to the heat flow and work that is acted on or produced by the system.

Secondly, the chemical exergy of a system can be calculated, this is defined as the maximum possible work that can be extracted by a system if the system is being brought into chemical equilibrium with the environment. The calculation of this component highly depends on the composition of the environment and the species that are present in the system. One of two scenario's is possible, the first possibility is (1) the species is present in both the system and the environment (2) the species is not present in the environment. In the first case, the calculation of the chemical potential depends on the phase of the reference environment. In this case the lithosphere of the Moon is under consideration, thus the solid phase of the chemical components is relevant, the chemical exergy of the species is based on the mixture of ideal gases as explained in section 5.2 as proposed by Szargut [95].

The second case, where the species is only present in the system but not in the reference environment assumes a chemical reaction of the species of interest with the environment, the environment is considered to have an unchanging fraction of the species present in it and an infinite amount of material, this ensures the system does not change the environmental composition. Therefore the carrier of the total amount of chemical exergy of a chemical reaction is the species not present in the environment, since its introduction into the environment creates only species already present in the environment and energy. This is the reason that hydrogen and carbohydrate fuels are said to have a high energy density, but the fact that oxygen is needed for the reaction is often not taken into consideration. Oxygen is assumed to be present in the environment because the atmosphere of Earth has oxygen in abundant amount. During electrolysis of water on Earth the oxygen generated during that reaction is never seen as an energetically interesting product whereas hydrogen is seen as interesting even though they are two sides of the same coin. The reason this point is being made is the following: After electrolysis in the lunar environment, hydrogen and oxygen are being produced, however, if one would only look at the chemical potential they both carry w.r.t. the environment the exergy present in both species would be greatly underestimated because the combined exergy that is being carried by the hypothetical reaction of the electrolyzed oxygen and hydrogen to water is greater and also the aim of the eventual combustion of the molecules in the combustion chamber of the rocket. When looking at the exergy flow through a system as will be done by means of a Sankey diagram, not considering this would make

an electrolyzer appear as an exergetically highly inefficient device, which it is not.

3.1. EXERGY EQUATIONS AND BALANCES

For the comparison of different processes, exergy is an interesting system characteristic to consider since it takes into account the thermodynamic irreversibilities and therefore the loss of useful work a.k.a exergy destruction. This provides insight into how much work can be done by a system if it would reach an equilibrium with its environment. The exergy of a system can only be defined relative to its operating environment. Not all energy is useful energy this has led to the development of the concept of exergy. Generally, two different types of energy inputs are used in an exergy analysis, electrical energy that is 100 % work and heat, of which the exergy is defined as the maximum work that can be produced between two heat reservoirs and is proportional to the Carnot efficiency and thus depends on the environmental temperature. The system of equations given below defined the exergetic state of a system.

$$Ex_{tot} = Ex_{ph} + Ex_{ch} + Ex_{kin} + Ex_{pot} + Ex_Q + Ex_W \tag{3.1}$$

$$Ex_{ph} = (H - H_0) - T_0(S - S_0) \tag{3.2}$$

$$Ex_{ch} = \sum_i n_i(\mu_{i0} - \mu_{00}) + RT_0 \sum_i n_i \cdot ln(\frac{c_i}{c_{i0}}) \tag{3.3}$$

$$Ex_Q = Q \cdot (1 - \frac{T_0}{T_s}) \tag{3.4}$$

$$Ex_W = W = P_e \tag{3.5}$$

Where Ex_{ph}, Ex_{ch}, Ex_{kin}, Ex_{pot} are physical, chemical, kinetic, and potential exergy of the products of the system respectively. H, S, μ, n, c, T are the enthalpy, entropy, chemical potential, number of moles, concentration, and temperature respectively. The subscript 0 denotes the 'dead state' where the system is in equilibrium with the environment. For chemical processes kinetic and potential can be disregarded because of the small contributions. E_Q and Ex_w are the exergy of a thermal reservoir and electrical work respectively.

$$Ex_D = Q \cdot (1 - \frac{T_e}{T_s}) - W + Ex_{in} - Ex_{out} \tag{3.6}$$

The exergy destruction, Ex_D, can be calculated using the equation above.

4

REFUELING MODULE

4.1. PATCHED CONICS

Rockets are used to transport payloads and people to various destinations in space. One of the most common types of rockets used for space exploration is the two-stage rocket. This rocket uses two stages of engines to achieve orbit or travel to a specific destination. In this particular case as depicted in fig. 4.1, we are exploring a two-stage rocket that will leave the lunar surface, and decouple at low lunar orbit, with the boosters of the first stage returning and the second stage continuing to low Earth orbit, where it will leave the payload before returning to the lunar surface. This type of rocket design requires careful planning and execution to ensure a successful mission.

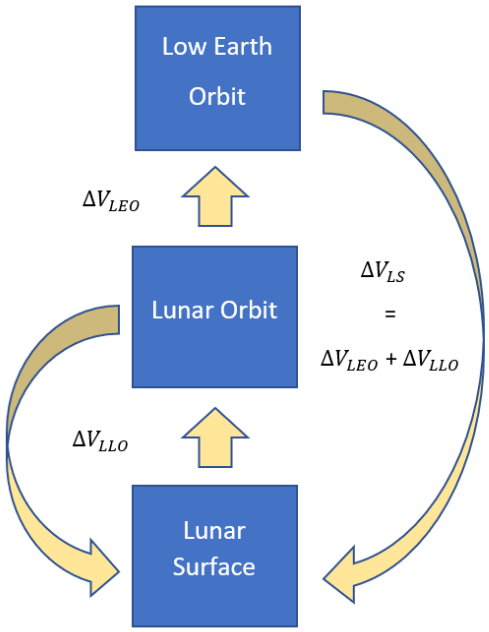

Figure 4.1: Refueling mission schematic

Let us look at the Delta-V of the mission that was calculated using the patched-conics method. Patched conics is a technique used in spaceflight mechanics that simplifies the modeling of the motion of a spacecraft in the vicinity of celestial bodies. It involves dividing the space around a celestial body into a series of conic sections, each of which represents a different gravitational field. While this technique has many advantages, it also has some disadvantages. Here are some of the pros and cons of patched conics in space:

Advantages:

- Simplification: The patched conics technique simplifies the complex problem of spaceflight mechanics by dividing the space around a celestial body into a series of simpler, easier-to-model regions.
- Computationally efficient: The calculations required for patched conics are relatively simple and computationally efficient, making them easy to perform and requiring less computing power.
- Provides a good approximation: Patched conics provide a good approximation of the motion of a spacecraft in the vicinity of a celestial body.

Disadvantages:

- Limited accuracy: The patched conics technique is only an approximation and does not account for all of the complex interactions that can occur in spaceflight, such as gravitational perturbations from other celestial bodies or non-spherical gravitational fields.
- Discontinuous: The patched conics technique is discontinuous, which means that it can produce unrealistic results when a spacecraft crosses the boundary between two conic sections.
- Requires assumptions: The patched conics technique requires several assumptions to be made, such as assuming that the celestial body is a perfect sphere, which can limit its accuracy in some cases.

The method being discussed is an approximation, and it is worth noting that the transition from geocentric to selenocentric motion occurs gradually over a finite arc of the trajectory, affected by both the Earth and the Moon. However, for initial mission analyses, patching two conics together at the edge of the Moon's sphere of influence is a satisfactory approximation [25, 101]. It's important to recognize that while this technique is useful for preliminary analyses, it's not precise enough for computing the exact perilune altitude. A better description of the system can be achieved using the restricted three-body problem. The circular restricted three-body problem is a specific case in which two masses move in circular orbits around their common center of mass, while a third small mass moves in the same plane. This setup is often approximated by the Sun-Earth-Moon system and other similar configurations. In this case Spacecraft-Earth-Moon system. It can be used for more accurate trajectory analyses of spacecraft following Earth-Moon trajectories, the equations of motion must incorporate the gravitational interaction between the Moon and Earth. Compared to the patched conics method, the circular restricted three-body problem is a more precise approximation. To achieve even greater accuracy, perturbations resulting from the gravitational field of the Sun can also be taken into account.

Overall, patched conics is a useful technique for simplifying the modeling of the motion of a spacecraft in the vicinity of celestial bodies, but it is not without its limitations. Its accuracy and applicability depend on the specific circumstances of the space mission.

The spacecraft is first placed into an orbit of 18 km above the lunar surface, through a Hohmann transfer the rocket is brought to a higher orbit that is constrained by the sphere of influence of the Moon, because outside its radius the lunar gravitational field is too weak to keep the spacecraft in orbit. Now the upper stage continues further to Earth whereas the lower stage returns to the Moon.

The relevant mission ΔV's for the design of the respective stages are the following:

- $\Delta V_{LLO} = \Delta V_{orbit} + \Delta V_{gl} + \Delta V_{Hohmann}$
- $\Delta V_{LEO} = \Delta V_0 + \Delta V_p$
- $\Delta V_{LS} = \Delta V_{LLO} + \Delta V_{LEO}$

Where the $\Delta V_{orbit} = \Delta V_{landing}$, ΔV_{gl}, $\Delta V_{Hohmann}$, are the orbital velocity at first orbit insertion at 18 km, the gravity loss of the initial launch and the Hohmann transfer to the orbit from which the spacecraft will leave by accelerating above the escape velocity.

It is required to design a rocket that can bring propellant to LEO to perform a refueling maneuver. The rendezvous operation will allow a spacecraft to continue its journey after it has expelled all of its propellants to place itself in LEO.

The design will depend on a variety of factors including ΔV, I_{sp}, and payload. Firstly the spacecraft will be placed in LLO as described in "The regolith rocket—A hybrid rocket using lunar resources"[93]. Note that there are four different ΔV's to be examined for a two-stage fully reusable rocket.

- ΔV_{LLO} is the ΔV required to bring the entire refueling spacecraft into LLO.
- ΔV_{d_1} is the required ΔV to return the ascent booster stage back to the lunar surface.
- ΔV_{LEO} brings the second stage from LLO to LEO where the payload will be jettisoned.
- ΔV_{d_2} is the ΔV required to bring the empty rocket stage back from LEO to the lunar surface.

For the two stages, the ascend and descent ΔV's are:

- $\Delta V_{a,2} = \Delta V_{LLO}$

- $\Delta V_{d,2} = \Delta V_{LLO}$
- $\Delta V_{a,1} = \Delta V_{LEO}$
- $\Delta V_{d,1} = \Delta V_{LEO} + \Delta V_{LLO}$

It is thus assumed that the required ΔV is equal for both the inbound and outbound trips.

ΔV_{LLO}

Firstly the insertion from the lunar surface into LLO ought to be examined.

$$\Delta V_{LLO} = \Delta V_{orbit} + \Delta V_{gl} + \Delta V_{Hohmann} \tag{4.1}$$

where ΔV_{orbit} is the difference in velocity of the spacecraft at the lunar surface and at a given orbital height and eccentricity around the Moon which is 18 km for the ascent stage as was done during the Apollo mission.

$$\Delta V_{gl} = \int_0^{t_{burn}} g_M \cdot sin(\gamma(t))dt \tag{4.2}$$

Now we assume that the angle of ascent, γ, changes over time in the following way:

$$\gamma(t) = \frac{\pi}{2}\left(1 - \frac{t}{t_{burn}}\right) \tag{4.3}$$

The equation above assumes an initial angle of $\frac{\pi}{2}$ that linearly goes to 0 with a slope of $-\frac{\pi}{2 \cdot t_{burn}}$ Noting that $sin(\frac{\pi}{2} - x) = cos(x)$ and applying it to equation 4.2 where $x = \frac{\pi t}{2t_{burn}}$ and $dx = \frac{\pi dt}{2t_{burn}}$, the equation rewrites to

$$\Delta V_{gl} = \frac{2t_{burn}}{\pi} \int_0^{\frac{\pi}{2}} g_M \cdot cos(x)dx = \frac{2t_{burn}}{\pi} \cdot g_M \tag{4.4}$$

Now assuming a burn time of t_{burn} = 150 s the gravity loss can be found. Such that $\Delta V_{gl} = 154.6\ \frac{m}{s}$.

HOHMANN TRANSFER

Now a Hohmann transfer will be used with two burns, one from a circular orbit to an elliptical one, then a second burn to place the spacecraft in the orbit from which the patched conics interplanetary journey will start. The orbits are constraint by the sphere of influence of the Moon that can be calculated in the following manner[101]:

$$R_{SOI} = a\left(\frac{m}{M}\right)^{\frac{2}{5}} \tag{4.5}$$

Where a is the semi-major axis of the Earth-Moon system, m, is the mass of the smaller body and M is the mass of the larger body. It is known that $a_{Earth-Moon}$ is $385 \cdot 10^3$ km and $m_{Moon} = 7.346 \cdot 10^{22}$ kg and $m_{Earth} = 5.97 \cdot 10^{24}\ \frac{m^3}{s^2}$. Therefore the resulting sphere of influence is:

$$R_{SOI} = 385 \cdot 10^3 \left(\frac{7.346 \cdot 10^{22}}{5.97 \cdot 10^{24}}\right)^{\frac{2}{5}} = 66.1 \cdot 10^3 \text{ km}$$

The mission will be performed using three burns. First, the spacecraft is brought into LLO then the second burn will take the spacecraft to orbit where the first stage will decouple and return to the lunar surface. The second stage will reach the escape velocity and go to LEO to deliver the payload.
The estimated ΔV for Hohmann-transfers is can be described by a system of equations. For elliptical orbits, the vis-viva equation [101] is depicted as:

$$V_{orbit} = \sqrt{\mu_{Moon}\left(\frac{2}{r_{orbit}} - \frac{1}{a}\right)} \tag{4.6}$$

Also, the semi-major axis is given by a,

$$a = \frac{r_1 + r_2}{2} \tag{4.7}$$

Where r_1 and r_2 are the perilune and apolune of the elliptical orbit.
Combining yields the velocity at the perilune of the elliptical orbit that the spacecraft follows after the ΔV burn:

$$V_{orbit} = \sqrt{\mu_{Moon}\left(\frac{2}{r_{orbit,1}} - \frac{2}{r_{orbit,1} + r_{orbit,2}}\right)} \tag{4.8}$$

rewriting gives:

$$V_{orbit} = \sqrt{\frac{\mu_{Moon}}{r_{orbit,1}}\left(2 - \frac{2 \cdot r_{orbit,1}}{r_{orbit,1} + r_{orbit,2}}\right)} \tag{4.9}$$

Consequently,

$$V_{orbit} = \sqrt{\frac{\mu_{Moon}}{r_{orbit,1}}\left(\frac{2r_{orbit,2}}{r_{orbit,1} + r_{orbit,2}}\right)} \tag{4.10}$$

For circular orbits this simplifies to:

$$V_{orbit} = \sqrt{\frac{\mu_{Moon}}{r_{orbit}}} \tag{4.11}$$

Therefore it can be concluded that the required ΔV, to go from a circular orbit with distance r_1 to an elliptical orbit with perilune r_1 and apolune r_2, is the difference in velocity of both orbits at r_1. Resulting in:

$$\Delta V_h = \sqrt{\frac{\mu_M}{r_1}}\left(\sqrt{\frac{2r_2}{r_1 + r_2}} - 1\right) \tag{4.12}$$

PATCHED CONICS

Firstly the orbital energy of a spacecraft operating in the gravitational field of a celestial body is given by:

$$\mathscr{E} = \frac{1}{2} \cdot V^2 - \frac{\mu}{r} < 0 \tag{4.13}$$

If the difference between the kinetic energy and potential energy of the gravitational field is negative, the spacecraft is contained within the gravitational field and does not have enough energy to escape it. An impulsive shot is applied such that the trajectory of a given spacecraft can be altered to a desired elliptical orbit. The case for a transfer from LEO to the edge of the SOI of the Moon will be looked at. Given that the parking orbit of a spacecraft around the Moon is at a distance of r_0, the orbital velocity is $V_0 = \sqrt{\frac{\mu_{Earth}}{r_0}}$ as given by 4.11. When the impulsive shot is applied the subsequent velocity can be written as:

$$\vec{V_1} = \vec{V_0} + \vec{\Delta V_0} \tag{4.14}$$

Considering we operate in a two-dimensional reference frame, the resulting vector is just the sum of the x-components and y-components. Now we define the angle between V_0 and ΔV_0 as δ_0 and the angle between V_0 and V_1 as γ_1, which is also the angle used to project V_1 onto a perpendicular vector and should be used to calculate the angular momentum. The system of equations that arises out of the velocity relations above are the following:

$$\begin{cases} (\Delta V_0)^2 = V_0^2 + V_1^2 - 2V_0V_1cos(\gamma_1) \\ V_1^2 = V_0^2 + (\Delta V_0)^2 + 2V_0\Delta V_0 cos(\delta_0) \end{cases} \tag{4.15}$$

Combining yields the following relationship:

$$V_1 = \frac{V_0}{cos(\gamma_1)} + \Delta V \frac{\delta_0}{cos(\gamma_1)} \tag{4.16}$$

The angular momentum of the spacecraft in the resulting orbit is given by:

$$H = r_1 \cdot V_1 \cdot cos(\gamma_1) \tag{4.17}$$

That can be directly used to calculate the p, the semi-latus rectum:

$$p = \frac{H^2}{\mu} \tag{4.18}$$

V_1 is plugged into the energy equation 4.13 such that the semi-major axis of the orbit can be calculated.

$$a = \frac{-\mu}{2 \cdot \mathscr{E}} \tag{4.19}$$

Using 4.18 and 4.19 the eccentricity of the orbit follows:

$$e = \sqrt{1 - \frac{p}{a}} \tag{4.20}$$

Through the well-known trajectory equation, the true anomaly at a given distance r can be calculated:

$$\theta = cos^{-1}(\frac{p-r}{e \cdot r}) \tag{4.21}$$

The time needed to perform the transfer should be within a reasonable limit and can be derived by firstly calculating the eccentric anomaly E,

$$E = 2 \cdot arctan\left(\sqrt{\frac{1-e}{1+e}} tan\left(\frac{\theta}{2}\right)\right) \tag{4.22}$$

and now applying it to the flight time equation between two eccentric anomalies:

$$t_f = \sqrt{\frac{a^3}{\mu}} \cdot (E_2 - E_1 - e \cdot (sin(E_2) - sin(E_1)) \tag{4.23}$$

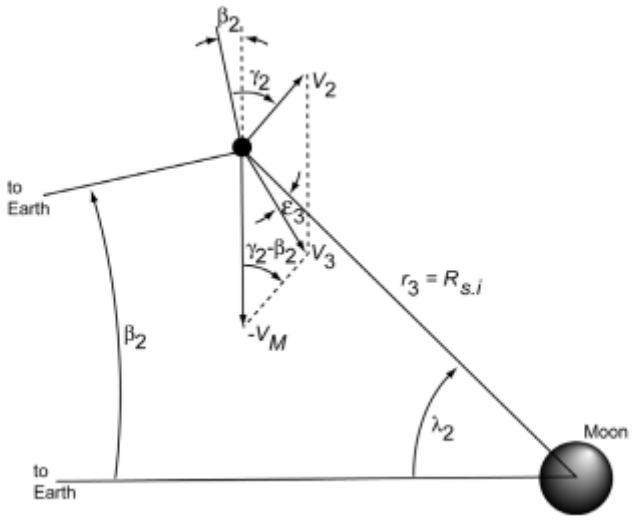

Figure 4.2: Conditions of a spacecraft entering the lunar SOI [101]

The trajectory equations are assumed to hold up until the arrival at the edge of the sphere of influence of the lunar gravitational field, where the conditions are transformed into the lunar reference frame. The position relative to the Earth's center can be computed using the rewritten cosine formula:

$$r_2 = \sqrt{D_M^2 + R_{SOI}^2 - 2 \cdot D_M \cdot R_{SOI} \cdot cos(\lambda)} \tag{4.24}$$

The velocity of the spacecraft in its elliptical orbit around the Earth can be obtained by rewriting 4.13 giving the relation:

$$V_2 = \sqrt{2 \cdot \left(\mathscr{E} + \frac{\mu}{r_2} \right)} \tag{4.25}$$

At the moment of SOI entry, the flight path angle in the Earth reference frame can be found using the angular momentum equation.

$$\gamma_2 = cos^{-1} \left(\frac{H}{r_2 \cdot V_2} \right) \tag{4.26}$$

This is the angle between the velocity vector and a vector perpendicular to the position vector. Now we define the angle between the position vector of the Moon and the position vector of the spacecraft measured from the Earth as β. Note that once the sphere of influence of the Moon is entered the velocity transformation is given by:

$$\vec{V}_3 = \vec{V}_2 - \vec{V}_M \tag{4.27}$$

Where the velocity of the Moon is perpendicular to its position vector. Now using the law of cosines the entry velocity of the sphere of influence can be computed:

$$V_3 = \sqrt{V_M^2 + V_2^2 - 2 \cdot V_M \cdot V_2 \cdot cos(\xi)} \tag{4.28}$$

Where ξ is the difference between the flight path angle of the spacecraft, γ_2, and the angle spanning the position vectors, β_2 relative to the Earth.

Where κ is calculated using the following relation:

$$\kappa = arcsin \left(\frac{V_M}{V_3} cos(\lambda) - \frac{V_2}{V_3} cos(\lambda + \xi) \right) \tag{4.29}$$

Now we know the direction and velocity of the spacecraft within the reference frame of the SOI of the Moon. Therefore the following can be said:

$$\mathscr{E} = \frac{1}{2} \cdot V_3^2 - \frac{\mu_M}{r_3} \tag{4.30}$$

projecting V_3 onto the vector perpendicular to the position vector and calculating the angular momentum:

$$H = r_3 \cdot V_3 \cdot sin(\kappa) \tag{4.31}$$

$$p = \frac{H^2}{\mu_M} \tag{4.32}$$

Considering the trajectory of the spacecraft, it is expected that a hyperbolic trajectory will be taken and thus the equation for the eccentricity is given by:

$$e = \sqrt{1 + 2 \frac{H^2 \cdot \mathscr{E}}{\mu_M^2}} \tag{4.33}$$

Now using this in the trajectory equation, the perilune is found and equal to:

$$r_p = \frac{p}{1 + e} \tag{4.34}$$

with velocity V_p,

$$V_p = \sqrt{2 \cdot \left(\mathscr{E} + \frac{\mu_M}{r_p} \right)} \tag{4.35}$$

To stabilize the orbit at V_p the required ΔV is the difference between the velocity at the perilune of the hyperbolic trajectory and that of the circular orbit at r_p.

$$\Delta V_p = V_p - \frac{\mu_M}{r_p} \tag{4.36}$$

From there a Hohmann transfer to LLO is done and the spacecraft is landed.

Now the parking orbit around Earth is kept constant at 420 km. The trajectory ΔV is minimized using the 'SciPy' package in Python that optimizes ΔV_0, δ_0 and λ_0 is used to minimize the following objective function:

$$\Delta V_{tot} = \Delta V_0 + \Delta V_p + \Delta V_{Hohmann} + \Delta V_{gl} + \Delta V_{landing} \tag{4.37}$$

The parameters for the optimization of the objective function can be found in table 4.1:

Parameters	ΔV_0	δ_0	λ_0
Values	3.140 $\frac{km}{s}$	13.59 °	59.72 °

Table 4.1: Optimized variables for a lunar trajectory

The mission ΔV can be subdivided into multiple parts that are given in 4.2.

ΔV_0	ΔV_p	$\Delta V_{Hohmann}$	ΔV_{orbit}	ΔV_{gl}	ΔV_{tot}
3.140 $\frac{km}{s}$	0.643 $\frac{km}{s}$	0.478 $\frac{km}{s}$	1.678 $\frac{km}{s}$	0.1546 $\frac{km}{s}$	5.939 $\frac{km}{s}$

Table 4.2: ΔV requirements for mission stages

The values for ΔV_{LLO} , ΔV_{LEO}, ΔV_{LS} can be found in table 4.3.

ΔV_{LLO}	ΔV_{LEO}	ΔV_{LS}
2311 $\frac{m}{s}$	3784 $\frac{m}{s}$	6094 $\frac{m}{s}$

Table 4.3: Design ΔV for two-stage rocket

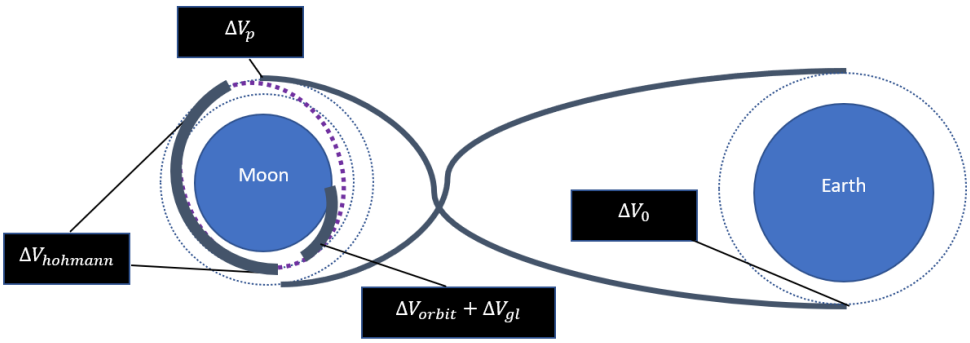

Figure 4.3: Schematic of all burns related to the Moon-Earth transfer trajectory

The lower stage splits off right before the ΔV_p burn because at this instance the upper stage will continue its trajectory that leaves the SOI of the Moon making it very difficult to return the lower stage to the lunar surface, also burns closer to celestial bodies are more efficient. This can be explained by the kinetic energy equation that is given by: $\frac{(V+\Delta V)^2}{2}$. For lower orbits, the velocity, V, is higher, now adding the ΔV of the burn and squaring it gives the energy, thus the initial velocity before the burn determines the energy increase. The total ΔV requirement as calculated by the Patched Conics method might somewhat underestimate the real ΔV requirement when considering the gravitational losses. However, the estimate for the LEO-lunar surface trajectory is close to 6.1 $\frac{km}{s}$ which corresponds to values found in the literature [111].

4.2. PROPELLANT

4.2.1. HYDROLOX

Hydrolox, a rocket propellant composed of liquid hydrogen (LH2) and liquid oxygen (LOX), is considered a significant technological achievement in the space industry for its efficient storage and use of both fuels. Its high specific impulse (I_{sp}) of up to 450-500 seconds makes it a popular choice for rocketry, with the current Vulcain 2.1 rocket engine achieving an I_{sp} of 432 seconds using hydrolox [5]. Hydrolox is also considered a green propellant, producing only water and hydrogen during combustion. The remaining hydrogen after combustion is due to the fuel-rich mixture that is normally used in hydrolox engines. Fuel-rich mixtures are used because the additional fuel lowers the adiabatic flame temperature which prevents melting or damage to the propulsion system, also the exhaust velocity at the nozzle outlet is an inverse function of molar mass. The average molar mass of the exhaust products is lowered by adding the hydrogen considering it has the lowest molar mass of all molecules. In addition to that, hydrolox is a fuel-rich propellant meaning more fuel is added to the propellant mixture that would be required for a perfect stoichiometric reaction.

However, the cost of hydrolox on Earth is relatively high due to the storage requirements at cryogenic temperatures. The extremely low boiling point of hydrogen at just 21 K makes its storage challenging, whereas oxygen has a boiling point of 97K, making its storage comparatively less demanding.

Given the extremely low storage temperature required for hydrogen, it must be constantly insulated and shielded from radiation during space travel. Furthermore, due to its low density, a larger storage tank is needed to hold the hydrogen, resulting in an undesirable increase in overall mass.

In the past decade, it has been discovered that the Moon has vast quantities of water, particularly in the poles where spectrometric analysis has shown concentrations of 100-412 ppm in PSRs and an estimated total mass of nearly 600 billion kilograms [94]. This discovery has significant implications for space exploration, as the water could be used as a rocket propellant and for in-situ life support in the establishment of a permanent and self-sustaining lunar colony. This study focuses on the application of in-situ resource utilization for propellant generation, whereby liquid hydrogen and liquid oxygen can be produced through electrolysis and then combusted to create water, heat, and additional hydrogen.

The fuel-rich hydrogen serves as a non-combusted working fluid, taking advantage of its low molar mass to convert energy in the combustion chamber more efficiently into specific impulse. The chemical reaction is the following:

$$aH_2 + bO_2 \rightarrow 2b \cdot H_2O + (a-2b) \cdot H_2 + Q \tag{4.38}$$

The above reaction, in its simplest form, does not consider dissociation and reverse reactions. As a result, this leads to a lower energy generation (Q) and a subsequent decrease in the chamber temperature of the rocket. Nonetheless, this reaction remains the primary combustion mechanism responsible for generating the energy required for the thrust.

The viability of utilizing lunar water as a propellant source remains uncertain, as the costs associated with mining, separating, transporting, storing, and electrolyzing the water could potentially outweigh the benefits. The economic incentives must be carefully weighed against the reduction in initial system mass, as the cost of purchasing in-space propellant may ultimately render any spacecraft design savings obsolete. However, the importance of water for long-term human presence and self-sufficiency cannot be understated, as it can be used for a variety of purposes, including food production, oxygen generation, and consumption.

For the design of a hydrolox rocket, the specific impulse and mixture ratio of the Vulcain 2.1 engine, which are 432 s and 6.03, respectively, will be taken into consideration [5].

4.2.2. OXYGEN

In order to create propellant, both fuel and an oxidizer are necessary. Oxygen is a popular choice for the oxidizer because it is abundant in space, including on celestial bodies such as the Moon and Mars. The lunar regolith is particularly rich in oxygen, which is stored in various oxides that can be mined using a variety of techniques. One major advantage of this approach is the flexibility to select a location for mining that is optimized based on a variety of factors.

When considering the oxidizer component of the propellant, it is important to note that oxygen makes up a significant portion of the overall mass in hydrolox or methalox propellant. Therefore, generating oxygen on

the Moon would result in a more versatile option and would still have a great reduction in mass for the propellant overall. TThe molar mass of hydrogen is approximately 2, while that of oxygen is approximately 32. The stoichiometric reaction requires twice as many moles of hydrogen as oxygen, resulting in a mass ratio of 8. However, hydrolox rockets usually have a mixture ratio of around 6, which means that for every kilogram of hydrogen, the rocket consumes 6 kilograms of oxygen. As a result, one possible option is to only refuel a hydrolox rocket with oxygen and transport the hydrogen from Earth. Additionally, oxygen can be utilized to combust methane in a methane-powered engine.

Due to the highly reactive nature of oxygen, the lunar soil is primarily made up of oxidized materials. To extract oxygen from the lunar regolith, there are multiple techniques that vary in terms of energy input and resource output. One such method is to concentrate sunlight, which would heat the soil and break the chemical bonds, resulting in the extraction of volatiles through vaporization. As resources and tools brought from Earth are limited, it is crucial to develop efficient extraction methods that yield useful byproducts for building a sustainable lunar base in the long run.

4.2.3. ALICE

The propulsion combination known as ALICE is named after the words aluminum and ice, and involves a chemical reaction between the two substances to produce thrust.

$$2Al + 3H_2O \rightarrow Al_2O_3 + 2H_2 + Q \tag{4.39}$$

The reason aluminum rocket propellant has not been used is the reaction time and inferior specific impulse compared to other well-established rocket propellants. Recent advancements in nanoscale aluminum have shown a significant increase in the reaction rate of propellant mixtures. Varying the grain size in the range of 50μm-100nm for different configurations of the propellant can lead to a burning rate increase of up to 100% [75]. The reaction between aluminum and water has the advantage of producing hydrogen, which can serve as a working fluid to carry momentum. Additionally, the oxide coating of nanoparticles can be more easily overcome, resulting in a higher burn rate and increased energy, leading to higher temperature and pressure, and ultimately, a higher exhaust velocity for the spacecraft.
According to a study, engines that use Viton-coated aluminum powder as an ALICE propellant can achieve a specific impulse of 234s. The density of aluminum water propellant is approximately 1450 $\frac{kg}{m^3}$. Further calculations have shown that ALICE has the potential to achieve even higher specific impulses. By using the NASA CEA equilibrium code and assuming an expansion ratio of 100, a mass mixture ratio of 1.2 can result in specific impulses greater than 300s [76].

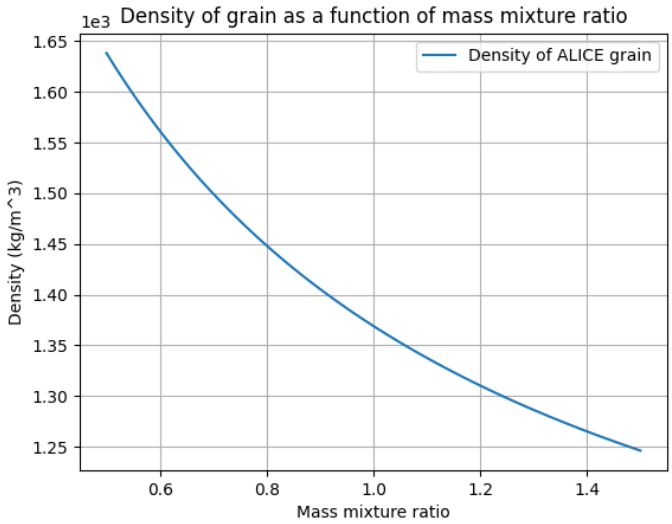

Figure 4.4: ALICE grain density

$$m_p = m_f + m_o = m_f \cdot \left(1 + \frac{O}{F}\right) \tag{4.40}$$

$$m_p = \rho_p \cdot V_p = \rho_p \cdot \left(\frac{m_f}{\rho_f} + \frac{m_o}{\rho_o}\right) = \rho_p \cdot \left(\frac{m_f}{\rho_f} + \frac{m_f \cdot \frac{O}{F}}{\rho_o}\right) = \rho_p \cdot m_f \left(\frac{1}{\rho_f} + \frac{\frac{O}{F}}{\rho_o}\right) \tag{4.41}$$

Where m_p, m_f, m_o, ρ_p, ρ_f and ρ_o are the propellant, fuel and oxidizer masses and densities, respectively. Combining eq. 4.40 and eq. 4.41 gives the following relation between the density of the grain and the mass mixture ratio:

$$\rho_p = \rho_o \cdot \rho_f \frac{1 + \frac{O}{F}}{\rho_o + \rho_f \cdot \frac{O}{F}} \tag{4.42}$$

As can be seen in figure 4.4, that is plotted using eq. 4.42, the density of the grain decreases as the mass ratio increases this is to be expected considering the oxidizer is water ice, which has a density of, ρ_f, 917 $\frac{\text{kg}}{\text{m}^3}$, and the fuel is aluminum, with a density of, ρ_o, 2700 $\frac{\text{kg}}{\text{m}^3}$. The increase in mass mixture ratio increases the relative mass of the oxidizer, water w.r.t. the fuel, aluminum. Thus as the mixture ratio increases the density of the grain deviates further from the density of aluminum as it comes closer to the density of water ice. The solid propellant grain's density and mass mixture ratio determine the shape and performance of the solid rocket motor. As a rule of thumb, the higher the specific impulse, I_{sp}, the more beneficial it is for the rocket system. This is of course due to the Tiolkovsky rocket equation 1.2. The equation indicates that as the I_{sp} increases the ratio $\frac{m_o}{m_f}$ can decrease for a constant ΔV, thus allowing for less propellant or more payload. For further analysis the following characteristics will be assumed for ALICE [75]:

ALICE	I_{sp}	T_c	P_c	c^*	$\frac{O}{F}$	$\frac{A_e}{A_t}$
Value	284.7 s	3084 K	69 bar	1361 $\frac{\text{m}}{\text{s}}$	1.0	40

Table 4.4: Mass Mixture Ratio, Specific Impulse, Density and Temperature for ALICE and Hydrolox rocket propellants

Table 4.4 gives the values for the specific impulse, combustion chamber temperature, chamber pressure, characteristic velocity and mass mixture ratio respectively. These values will be used for the design of the solid rocket motor for the refueling operation. From 4.4 it can be seen that the density related to the given mass mixture ratio is 1370 $\frac{kg}{m^3}$.

4.3. REFUELING OPERATION

4.3.1. MODEL DERIVATION

The propellant also has to be transported to LEO where it can be used for the refueling of spacecraft coming from Earth. For the transportation of the propellant, a spacecraft coming from the Moon must be designed to estimate the propellant requirement for this transportation system. A method for sizing such a spacecraft is provided below: Firstly a modified expression of the Tiolkovsky rocket equation is used:

$$m_{p,a_i} = m_{0_i} \cdot (1 - e^{-\frac{\Delta V a_i}{v_e}}) \tag{4.43}$$

Where m_{p,a_i} is the propellant for the ascent stage, m_{0_i} is the total mass at the start of the ascent stage burn and ΔV_{a_i} the ascent stage ΔV for stage i. Note that v_e is constant across the stages as it is assumed that the I_{sp} does not change. The rocket has a lift-off mass, m_{0_i}, is equal to the sum of the payload, m_{pay_i}, the structural mass,m_{s_i}, and the ascent and descent propellant mass m_{p,a_i} and m_{p,d_i} . The descent mass of the rocket is equal to the overall structural mass considering no part of the fairing is jettisoned.

The spacecraft mass for a given stage i can be defined as,

$$m_{0_i} = m_{s_i} + m_{p,a_i} + m_{p,d_i} + m_{pay_i} \tag{4.44}$$

Now we introduce the structural mass ratios of the ascent and descent phases of the stages which are defined as

$$\sigma_{a_i} = \frac{m_{s,a_i}}{m_{s,a_i} + m_{p,a_i}} \tag{4.45}$$

$$\sigma_{d_i} = \frac{m_{s,d_i}}{m_{s,d_i} + m_{p,d_i}} = e^{\frac{-\Delta V_{d_i}}{v_e}} \tag{4.46}$$

for the ascent and the descent stage respectively. It is important to note that the descent stage structural mass is equal to $e^{\frac{-\Delta V_{d_i}}{v_e}}$, this is derived from the Tiolkovsky rocket equation where:

$$\frac{m_f}{m_0} = e^{\frac{-\Delta V}{v_e}} \tag{4.47}$$

In the case of a descent stage, the structural mass and descent stage propellant mass are the initial mass, m_0, since the payload has been decoupled. At the moment of landing all propellant has been expelled and the final mass, m_f, is then equal to the structural mass. The structural mass ratio of the entire stage is,

$$\sigma_i = \sigma_{a_i} \cdot \sigma_{d_i} = \frac{m_{s_i}}{m_{s_i} + m_{p_i}} \tag{4.48}$$

Where the structural mass $m_{s_i} = m_{s,d_i}$ and $m_{p_i} = m_{p,d_i} + m_{p,a_i}$

Also the ascent stage structural mass is defined as:

$$m_{s,a_i} = m_{s,d_i} + m_{p,d_i} \tag{4.49}$$

Now plugging eq. 4.44 into eq. 4.43 gives,

$$m_{p,a_i} = (m_{s,d_i} + m_{p,a_i} + m_{p,d_i} + m_{pay_i}) \cdot (1 - e^{-\frac{\Delta V a_i}{v_e}}) \tag{4.50}$$

adding eq. 4.49 yields,

$$m_{p,a_i} = (m_{p,a_i} + m_{s,a_i} + m_{pay_i}) \cdot (1 - e^{-\frac{\Delta V a_i}{v_e}}) \tag{4.51}$$

Rewriting eq. 4.45 where m_{s,a_i} is placed on the left-hand-side,

$$m_{p,a_i} = \left(m_{p,a_i} + \left(\frac{\sigma_{a_i}}{1 - \sigma_{a_i}}\right) \cdot m_{p,a_i} + m_{pay_i}\right) \cdot \left(1 - e^{-\frac{\Delta V a_i}{v_e}}\right) \tag{4.52}$$

Restructuring the equation gives,

$$m_{p,a_i} = m_{pay,i} \cdot \frac{1 - e^{-\frac{\Delta V a_i}{v_e}}}{1 - \left(1 + \frac{\sigma_{a_i}}{1-\sigma_{a_i}}\right) \cdot \left(1 - e^{-\frac{\Delta V a_i}{v_e}}\right)} \tag{4.53}$$

An expression linking m_{p,a_i} and m_{s,d_i} is now derived.

Rewriting eq. 4.45 and combining with eq. 4.49

$$m_{s,d_i} + m_{p,d_i} = \frac{\sigma_{a_i}}{1-\sigma_{a_i}} \cdot m_{p,a_i} \tag{4.54}$$

Adding m_{p,a_i} on both sides gives,

$$m_{s,d_i} + m_{p,d_i} + m_{p,a_i} = \left(1 + \frac{\sigma_{a_i}}{1-\sigma_{a_i}}\right) \cdot m_{p,a_i} \tag{4.55}$$

The left-hand side is the sum of the total structural mass and the total stage propellant which and can be written as $m_{s,d} + m_p = \sigma_i^{-1} m_{s,d}$ as implied by equation 4.48.

Therefore,

$$m_{s,d_i} = \sigma_i \left(1 + \frac{\sigma_{a_i}}{1-\sigma_{a_i}}\right) \cdot m_{p,a_i} \tag{4.56}$$

$$m_{p,d_i} = m_{s,d_i} \cdot \left(\frac{1-\sigma_{d_i}}{\sigma_{d_i}}\right) \tag{4.57}$$

The payload of the final stage, the exhaust velocity, and the ΔV of each stage are known. Therefore m_{p,a_i} is a function of the structural mass ratio $\sigma_{a,i}$.

- $m_{pay,i} = \begin{cases} m_{payload} & for \quad i = 1 \\ m_{0_{i+1}} & for \quad i > 1 \end{cases}$
- $m_{p,a_i} = m_{pay,i} \cdot \frac{1-e^{-\frac{\Delta V a_i}{v_e}}}{1-\left(1+\frac{\sigma_{a_i}}{1-\sigma_{a_i}}\right)\cdot\left(1-e^{-\frac{\Delta V a_i}{v_e}}\right)}$
- $m_{s,d_i} = \sigma_i \left(1 + \frac{\sigma_{a_i}}{1-\sigma_{a_i}}\right) \cdot m_{p,a_i} = \sigma_{a_i}\sigma_{d_i} \left(1 + \frac{\sigma_{a_i}}{1-\sigma_{a_i}}\right) \cdot m_{p,a_i}$
- $m_{p,d_i} = m_{s,d_i} \cdot \left(\frac{1-\sigma_{d_i}}{\sigma_{d_i}}\right)$

The payload mass for each stage respectively depends on the number of stages n. Where if $i = 1$, the most upper stage is in effect which carries the mission payload. If $i > 1$ lower stages are in effect and thus the payload that is being carried by those stages is the total mass of the next stage.

Note that equation 4.53 is subject to the constraint,

$$\left(1 + \frac{\sigma_{a_i}}{1-\sigma_{a_i}}\right) \cdot \left(1 - e^{-\frac{\Delta V a_i}{v_e}}\right) < 1 \tag{4.58}$$

which equals,

$$\left(\frac{1}{1-\sigma_{a_i}}\right) \cdot \left(1 - e^{-\frac{\Delta V a_i}{v_e}}\right) < 1 \tag{4.59}$$

Thus,

$$\frac{1}{1-\sigma_{a_i}} < \frac{1}{1 - e^{-\frac{\Delta V a_i}{v_e}}} \tag{4.60}$$

Therefore m_{p,a_i} is defined by $\sigma_{a,i}$ if,

$$\sigma_{a_i} < e^{-\frac{\Delta V_{a,i}}{v_e}} \tag{4.61}$$

4.3.2. ALGORITHM

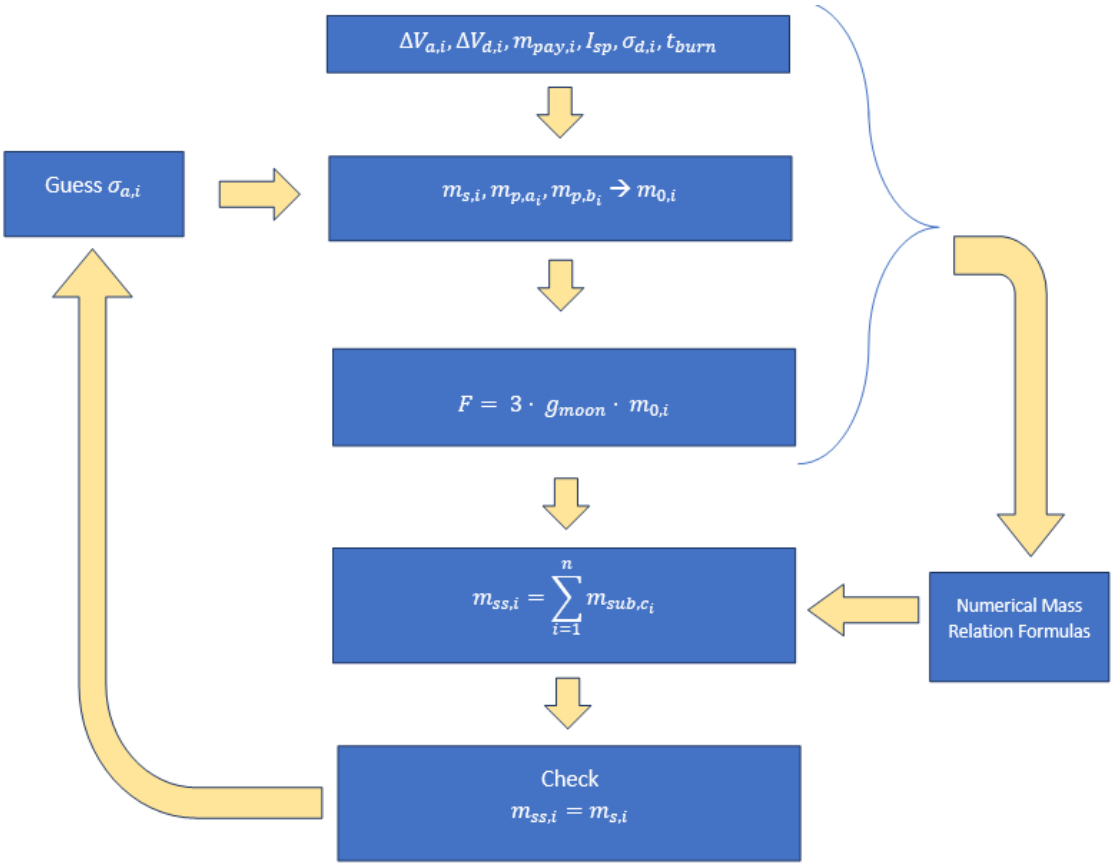

Figure 4.5: Algorithm procedure for rocket design mass estimation

The algorithm is based on both 'The regolith rocket—A hybrid rocket using lunar resources' [93], which uses Akin's mass relations [2] and the structural mass ratio as the driving parameter for the rocket optimization procedure and "Multidisciplinary Design Optimization of Reusable Launch Vehicles for Different Propellants and Objectives" [19], which provides insight into the derivation of a multi-stage reusable rocket algorithm.

Figure 4.5 outlines the steps that the algorithm follows to converge on a rocket design. First, known values of $m_{pay,i}$, $\Delta V_{a,i}$, $\Delta V_{d,i}$, and I_{sp} are used to calculate $\sigma_{d,i}$, which are the payload mass, ascent ΔV, descent ΔV, specific impulse and structural mass ratio of the ith stage. Next, an initial guess for $\sigma_{a,i}$ is used in equations 4.53 and 4.48 to determine the propellant mass of the ascent stage, m_{p,a_i}, and the structural mass ratio of the entire stage, σ_i, respectively.

The descent stage structural mass, m_{s,d_i}, is estimated using equation 4.56, and equation 4.57 is used to calculate the descent stage propellant mass, m_{p,d_i}. The total stage mass can then be determined using equation 4.44.

The thrust exerted on the structure must be greater than the gravitational pull of the Moon to have a net acceleration. Therefore the thrust is calculated such that the spacecraft accelerates at $0.1 \cdot g_{Moon}$ at take-off. This thrust is later used to estimate the engine mass.

Subsystem structural masses, m_{sub,c_i} are estimated using numerical relations and Ideal Rocket Theory, based on thrust, ΔV requirements, and masses already derived. The sum of these estimated masses is compared to the earlier derived structural mass, $m_{s,i}$. If they are the same, the rocket design has converged. If not, a new value for $\sigma_{a,i}$ is chosen and the process is repeated until convergence. This process is automated using the 'SciPy' package in Python.

The stages are designed in reversed order since the last stage is the one carrying the payload, which is a known design parameter on which the entire sizing depends. So after the first convergence, the resulting design describes the upper stage, this upper stage is then used in the next stage where it is considered to be the payload as explained in 4.3.1. Because the upper stage already accounts for the structural mass of the payload, there is no need for the lower stage to have its own encapsulating structure. However, the upper stage must have the same subsystems as the lower stage, in addition to a payload encapsulation system.

The breakdown of the structural mass of a hydrolox and ALICE rocket will be discussed in section 4.3.3 and section 4.3.4, respectively.

4.3.3. HYDROLOX ROCKET

To estimate the mass of a hydrolox rocket the mass relations of Akin can be used where regression techniques were applied to real rockets and used to estimate numerical relations for rocket subsystem masses. In this case, the structural mass of a hydrolox rocket is assumed to consist of five major subsystems: propellant tanks and insulation, engines, avionics, fairing, and payload structure. The equation provided shows that the total structural mass of the rocket, denoted as $m_{s,i}$, is equal to the sum of the masses of these five subsystems for a given rocket stage i.

$$m_{s,i} = m_{t_i} + m_{av,i} + m_{fairing,i} + m_{engine,i} + m_{s,payload_i} \tag{4.62}$$

In the equation above, m_{t_i} represents the mass of the propellant tanks and insulation, $m_{av,i}$ represents the mass of the avionics system, $m_{fairing,i}$ represents the mass of the rocket's fairing, $m_{engine,i}$ represents the mass of the rocket's engines, and $m_{s,payload_i}$ represents the mass of the payload structure.

$$m_{h_i} = \frac{m_{p_i}}{1 + \frac{O}{F}} \tag{4.63}$$

$$m_{o_i} = m_{p_i} - m_{h_i} \tag{4.64}$$

The mass mixture ratio, $\frac{O}{F}$, of a propellant is a critical factor in rocket propulsion design. This ratio represents the relative proportions of fuel and oxidizer required to achieve efficient combustion and generate sufficient thrust. The mass mixture ratio is determined by the mass of the propellant and the oxidizer-to-fuel ratio, $\frac{O}{F}$, required for the specific engine design.

When the propellant mass is known, equations 4.63 and 4.64 can be used to determine the mass of fuel and oxidizer required for the given $\frac{O}{F}$ ratio. The equations indicate that the mass of hydrogen, m_{h_i}, required is proportional to the propellant mass, m_{p_i}, and inversely proportional to the sum of the oxidizer-to-fuel ratio and one $(1+\frac{O}{F})$. Similarly, the mass of oxygen, m_{o_i}, can be calculated by subtracting the mass of hydrogen from the total propellant mass.

It is important to note that the ratio $\frac{O}{F}$ is not a constant value, it varies depending on the engine design, mission requirements, and other factors. The $\frac{O}{F}$ ratio can be determined based on the specific impulse and thrust requirements of the engine. For this hydrolox rocket the $\frac{O}{F}$ is 6.03 based on the Vulcain 2.1 engine. Therefore the required mass of fuel and oxidizer can be determined.

$$m_{t_i,h} = 9.09 \cdot V_{h_i} = 9.09 \cdot \frac{m_{h_i}}{\rho_h} \tag{4.65}$$

$$m_{t_i,o} = 12.16 \cdot V_{o_i} = 12.16 \cdot \frac{m_{o_i}}{\rho_o} \tag{4.66}$$

In the design of liquid oxygen and hydrogen tanks, the mass of the tanks must be taken into consideration. The tank mass estimation can be determined by using equations 4.65 and 4.66. These equations describe the mass of the tank for each respective propellant. The mass of the hydrogen tank, $m_{t_i,h}$, is calculated by multiplying the hydrogen tank volume, V_{h_i}, by a factor of 9.09, while the mass of the oxygen tank, $m_{t_i,o}$, is calculated by multiplying the oxygen tank volume, V_{o_i}, by a factor of 12.16. These values are proposed by Akin from the University of Maryland and where empirically derived using linear regression on existing tanks [2]. The volume of each tank is calculated based on the mass of the respective propellant and the density of that propellant which are $\rho_o = 1140\ \frac{\text{kg}}{\text{m}^3}$ and $\rho_h = 71\ \frac{\text{kg}}{\text{m}^3}$ for oxygen and hydrogen respectively [107].

Insulation is essential for the storage of liquid oxygen and hydrogen due to the extremely low temperatures at which they exist as liquids. This is necessary to prevent pressure build-up caused by phase changes and temperature increases in the propellant tanks, ensuring efficient combustion and stable rocket performance. The insulation helps to maintain the propellant temperature and pressure within safe limits.

$$L_c = \frac{V - \frac{4}{3}\pi R^3}{\pi R^2} \tag{4.67}$$

$$A = 4\pi R^2 + 2\pi R L_c \tag{4.68}$$

To estimate the insulation mass required for a spherical-cylindrical tank, an expression for the surface area is necessary. The surface area of a spherical-cylindrical tank can be determined using Equations 4.67 and 4.68, where V, R, and L_c represent the volume of the content of the tank, the radius of the tank, and the length of the cylindrical part, respectively. Once the surface area has been determined, the required insulation for both hydrogen and oxygen can be calculated using equations 4.69 and 4.70, respectively. These were again taken from Akin's mass relations based on empirically derived coefficients from regression.

$$m_{ins,h_i} = 2.88 \cdot A_{t_i,h} \tag{4.69}$$

$$m_{ins,o_i} = 1.123 \cdot A_{t_i,o} \tag{4.70}$$

It is worth noting that the insulation mass for a given surface area of a tank is twofold in the case of hydrogen. This is because of the very low-temperature requirement needed to keep it in a liquid form. Insulation for liquid hydrogen is therefore more critical and requires more mass compared to liquid oxygen.

$$m_{t_i} = m_{t_i,h} + m_{t_i,o} + m_{ins,h_i} + m_{ins,o_i} \tag{4.71}$$

Let us now consider the required mass for avionics. Avionics refers to the electronic systems used in spacecraft and rockets for guidance, navigation, and control. These systems are responsible for controlling the trajectory of the rocket, monitoring its performance, and transmitting data back to the ground.

In a rocket, avionics play a critical role in ensuring that the rocket follows its intended trajectory and reaches its target destination. They provide critical information to the rocket's guidance system, which uses this data to adjust the rocket's thrust and trajectory in real-time.

Avionics systems also play an important role in ensuring the safety of the rocket and its crew. They monitor critical systems such as the rocket's engines, fuel and oxidizer levels, and temperature and pressure sensors, alerting the crew to any issues that may arise during flight.

Overall, avionics are a vital component of any rocket or spacecraft, providing the critical information and control necessary for successful launch, flight, and landing.

The estimation of the mass of the rocket's avionics and wiring components, denoted as $m_{av,i}$, can be approximated by using the following expression [2]:

$$m_{av,i} = 10 \cdot m_{0,i}^{0.36} + 1.058 \cdot m_{0,i}^{0.5} \cdot L_i^{0.25} \tag{4.72}$$

where $m_{0,i}$ represents the initial mass of the rocket and L_i is the length of the rocket. Which is given by:

$$L_i = L_{pay} + L_{tanks,i} + L_{engine,i} \tag{4.73}$$

Where the length of the tanks, $L_{tanks,i}$, payload, L_{pay} and engine, $L_{engine,i}$ are the sum of the length of the cylindrical and spherical parts, the diameter of the payload structure and an assumed length of 2 m for the engine.

The first term of the expression represents the mass of the wiring components, while the second term represents the mass of the avionics components. The coefficients in the terms have been empirically determined through previous rocket designs.

It should be noted that the accuracy of this estimation can be influenced by several factors, such as the specific design and complexity of the avionics and wiring systems. Therefore, this expression serves as a rough estimate and may require adjustments based on the specific rocket design.

The fairing is a structure that encapsulates the all other systems and protects them from the harsh external environment during launch as well as providing structural integrity. The mass of the fairing can be estimated using the equation:

$$m_{fairing,i} = 4.95 \cdot A_{r,i}^{1.15} \tag{4.74}$$

where $A_{r,i}$ is the surface area of the rocket. The equation suggests that the mass of the fairing is proportional to the surface area of the rocket, with a power of 1.15. This implies that as the size of the rocket increases, the mass of the fairing will increase disproportionately. It is important to estimate the mass of the fairing as it directly affects the payload capacity of the rocket.

$$A_{fairing,i} = \pi \cdot R^2 \cdot L_i \tag{4.75}$$

Where R and L_i are the radius and length of the i'th stage, respectively.
The amount of thrust required to launch a rocket depends on the initial mass of the rocket and the gravitational pull of the Moon. The greater the mass and the gravitational pull, the higher the required thrust. The thrust is proportional to:

$$T_{r,i} = 3 \cdot m_{0,i} \cdot g_{moon} \tag{4.76}$$

To ensure that the rocket is able to overcome the gravitational pull of the Moon, the net acceleration should be positive. This means that the thrust must be high enough to provide this acceleration.

The mass of the engine required to generate the necessary thrust can be estimated using the following equation:

$$m_{engine,i} = 0.00514 \cdot T_{r,i}^{0.9207} \tag{4.77}$$

This equation relates the engine mass, denoted as m_{engine}, to the thrust generated by the engine, denoted as $T_{r,i}$. The equation is based on empirical data and can be used to estimate the engine mass for a given level of thrust [106].

In this thesis, three types of payloads are considered: Hydrolox, oxygen and ALICE. In the case of hydrolox, equations 4.63 - 4.70 are used to determine the payload structure. For oxygen equations 4.66, 4.67, 4.68 and 4.70 are used.

4.3.4. ALICE ROCKET

The numerical relations of an ALICE rocket are not present in current literature, therefore an estimation regarding the masses of the subsystems is done in a different manner. It will be assumed that the structural mass, $m_{s,i}$, of the rocket consists of the following: Shell mass, $m_{shell,i}$, nozzle mass, $m_{nozzle,i}$, ablative material, $m_{ablative,i}$, payload structure, $m_{s,payload_i}$ and avionics mass, $m_{av,i}$.

$$m_{s,i} = m_{shell,i} + m_{nozzle,i} + m_{ablative,i} + m_{s,payload} + m_{av,i} \tag{4.78}$$

To estimate the mass of the cylindrical shell, $m_{shell,i}$, we can use the thin-walled vessel equation. The equation relates the thickness of the shell, t, to the combustion chamber pressure, P_c, and diameter of the combustion chamber, D, yield strength of the combustion chamber material σ_{yield}, and a safety factor, S.

$$t = S \cdot \frac{P_c \cdot D}{2 \cdot \sigma_{yield}} \tag{4.79}$$

The safety factor, S, is a measure of how much stronger the shell is than it needs to be. It accounts for uncertainties in the design and manufacturing process, as well as any unexpected loads that the rocket may experience during flight. The combustion chamber pressure, P_c, and diameter, D_c, are specific to the rocket engine being used, while the yield strength of the material, σ_{yield}, depends on the material chosen for the shell.

The diameter of the rocket is then used to determine the overall shell mass by using the difference in volume of two cylinders:

$$m_{shell,i} = \rho_{shell} \cdot V_{shell,i} = \rho_{shell} \cdot \left(\pi \cdot L_{shell} \cdot \left(R_{out}^2 - R_{in}^2\right) + \pi \cdot R_{out}^2 \cdot t\right) \tag{4.80}$$

The symbols R_{out} and R_{in} represent the outer and inner radii, respectively, of a cylindrical structure, and they are related to the diameter D_c and thickness, t, of the structure through the given equations. The symbol

ρ_{shell} refers to the density of the shell material, which is a physical property that quantifies the mass per unit volume of the material. The length of the cylindrical shell of the combustion chamber, denoted by L_{shell}, can be estimated using the following equation:

$$L_{shell} = \frac{m_{p,i}}{\pi R^2 \rho_{ALICE} f} \tag{4.81}$$

Here, $m_{p,i}$ denotes the mass of the propellant for the rocket stage i, R denotes the radius of the combustion chamber, and ρ_{ALICE} is the density of the propellant. Equation 4.81 relates the length of the combustion chamber to the mass of the propellant, assuming a double inward burning grain with a filling ratio, f, of 0.95. The equation shows that the length of the combustion chamber is inversely proportional to the product of the square of the radius, the density of the propellant, and the filling ratio. Thus, a higher mass of propellant or a lower filling ratio would result in a longer combustion chamber.

The high combustion temperature of ALICE rocket propellant is a major obstacle considering the very limited variety of materials able to withstand such temperatures without causing substantial structural damage or complete failure.

To estimate the heat flow through the combustion chamber the values given in table 4.4 are used.

In rocket propulsion, it's crucial to have accurate information about engine parameters such as specific impulse, characteristic velocity, and thrust coefficient to optimize the rocket's performance. However, sometimes we may not have all the necessary data for these parameters. In such cases, we can use the Ideal Rocket Theory (IRT) to fill in the knowledge gaps of some engine parameters.

Let us now consider the quality factor of the combustion, this value is proportional to:

$$\xi_{com} = \frac{(c^*)_{exp}}{(c^*)_{id}} \tag{4.82}$$

The quality factor for the combustion typically ranges from 0.85 to 0.98 [107], depending on the type of propellant and combustion chamber used. A higher quality factor indicates more efficient combustion. A quality factor of 0.9 is taken for the ALICE configuration.

Equation 4.82 gives us the value of the ideal characteristic velocity that the engine should produce under ideal conditions. However, we can also calculate the ideal characteristic velocity using a different formula that involves the Vandenkerckhove parameter, Γ.

$$(c^*)_{id} = \frac{1}{\Gamma} \cdot \sqrt{R \cdot T_c} \tag{4.83}$$

Where the Vandenkerckhove parameter, Γ, is given by:

$$\Gamma = \sqrt{\gamma} \cdot \left(\frac{2}{\gamma+1}\right)^{\frac{\gamma+1}{2\cdot(\gamma-1)}} \tag{4.84}$$

Note that the Vandenkerckhove parameter is an essential parameter for the nozzle and combustion chamber design since it determines the nozzle's ability to expand the exhaust gases efficiently and produce thrust and the heat flow in the chamber.

Using a solver to find γ gives the value of the specific heat ratio. Also for the ALICE combustion gases, it is known what the molar masses of the substances are which in combination with the gas constant and the specific heat ratio give both c_p and c_v:

$$\gamma = \frac{c_p}{c_v} \tag{4.85}$$

$$c_p = c_v + R_M \tag{4.86}$$

In order to estimate the heat flow, the viscosity of the propellant is of importance. Normally it ranges between $6-9\cdot10^{-5}\ \frac{m^2}{s}$ [107]. The conductivity, k, of the propellant, can be calculated as well using:

$$k = \frac{\mu \cdot c_p}{Pr} \tag{4.87}$$

where μ is the kinematic viscosity and, Pr, the Prandtl number which relates thermal and momentum diffusivity and is approximated by:

$$Pr = \frac{4\gamma}{9\gamma - 5} \tag{4.88}$$

Again for the estimation of the required thrust, $T_{r,i}$, an initial acceleration of $0.1 \cdot g_{Moon}$ is required as described by equation 4.76.
Now using Newton's second law, the mass flow rate for a constant exhaust velocity can be determined

$$\dot{m} = \frac{T_{r,i}}{I_{sp} \cdot g_0} \tag{4.89}$$

Furthermore, IRT states that the mass flow, $\dot{m}$, and the throat area, A_t, are related as given by:

$$\dot{m} = \frac{\Gamma \cdot P_c \cdot A_t}{\sqrt{R \cdot T_c}} \tag{4.90}$$

Finally, the heat flow can be estimated as proposed by Cornelisse [107]:

$$h_c = 0.023 \cdot \left(\frac{\dot{m}}{A}\right)^{0.8} \cdot D_c^{-0.2} \cdot k \cdot Pr^{\frac{1}{3}} \cdot \mu^{-0.8} \cdot \left(\frac{T_c}{T_f}\right)^{0.68} \tag{4.91}$$

Where T_f and A are the film temperature between the combustion gases and the chamber wall and the cross-sectional area of the combustion chamber as given by:

$$T_f = \frac{T_c + T_w}{2} \tag{4.92}$$

The mass flow rate through the nozzle throat directly relates to burn time since the total propellant divided by the mass flow rate is equal to the burn time:

$$t_{burn} = \frac{m_p}{\dot{m}} \tag{4.93}$$

The convective heat flow at steady-state, where the chamber wall temperature is constant, can now be calculated,

$$\frac{Q}{t_{burn}} = \zeta_d \cdot h_c \cdot (T_c - T_w) \tag{4.94}$$

Where B is the Spalding number, a dimensionless number, used in liquid droplet evaporation studies [86]. It relates the sensible heat and latent heat of the evaporated material, h_v:

$$B = \frac{c_p \Delta T}{h_v} \tag{4.95}$$

As the enthalpy difference between the chamber wall and the combustion gases increases and the enthalpy required for evaporation of the ablative material decreases, more gas is generated. This results in an increase in the amount of mass flow entering the boundary layer, which in turn reduces the impact of friction on the boundary layer and ultimately decreases the heat transferred [107].

$$\zeta_d = 1.2 \cdot \frac{ln(1+B)}{B} \tag{4.96}$$

Based on the heat flow an ablative material must be selected to absorb the heat such that it does not damage the chamber wall and rocket structure.

In solid rocket propulsion, ablative materials are used as heat shields or cooling materials to protect the structural integrity of the high temperatures during reentry or combustion. Where conductivity, operating temperature, and heat capacity are important parameters when choosing an ablative material [1].

An estimation of the ablative material mass is given by:

$$m_{ablative,i} = \frac{Q_i}{C_{abl}} \tag{4.97}$$

Where C_{abl} denotes the specific energy absorption in $\frac{J}{kg}$.

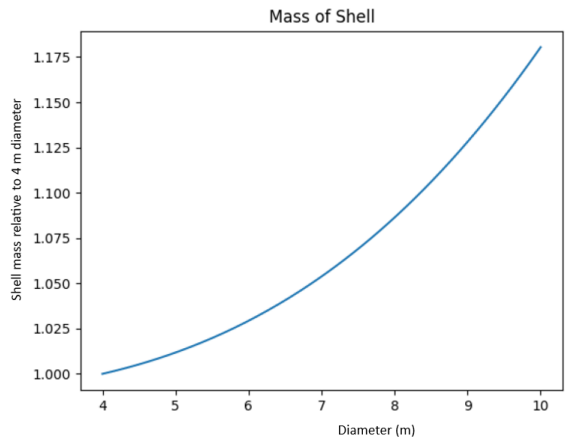

(a) Normalized shell mass behavior for a variety of rocket diameters for a constant inner shell volume

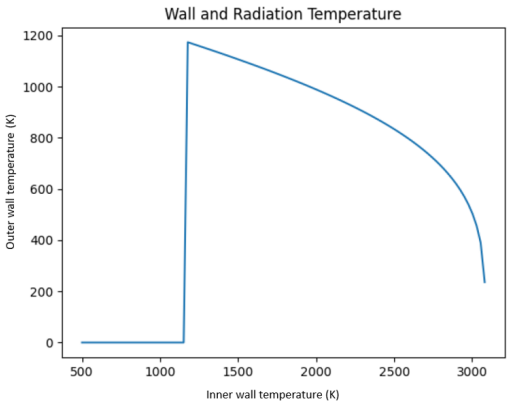

(b) Outer wall temperature required to radiate heat away depending on inner wall temperature and convection from combustion gases for a 6-diameter combustion chamber operating at 3084 K and the emission coefficient $\epsilon = 1$

Figure 4.6: Heat flow and shell mass behaviour

When looking at 4.6a which follows equation 4.81. For a constant inner volume of the shell, an increase in diameter results in a higher mass for the same design parameters of the rocket, this is because the thickness of the shell needs to increase as it follows equation 4.79. It should be noted that despite the volume remaining constant for the visualization in this figure, this actually neglects another very important factor, namely the increase of the propellant itself, as the mass increases the propellant mass needs to increase too and since the shell mass encapsulates the propellant, the increase shown in the figure actually underestimates the effect of the diameter on the total shell mass. The increase in diameter is therefore not desirable from the perspective of the shell mass However, figure 4.6b shows the case where, the following holds:

$$h_c(T_{w_{in}}) \cdot (T_c - T_{w_{in}}) = \epsilon \cdot \sigma \cdot T_{w_{out}}^4 \tag{4.98}$$

h_c is only a function of the inner wall temperature of the combustion chamber, keeping the rest of the parameters constant. The heat flow from the combustion gases to the wall is strongly dependent on the combustion chamber wall temperature as can be seen in the temperature gradient term in the equation above, also h_c reduces with a higher wall temperature, this means that both the convection coefficient and the temperature gradient decrease. Therefore, a very good insulator would be able to reduce the heat flow that needs to be radiated away from the spacecraft. Such an insulator does not exist, and the thermal conductivity of the existing insulators is not low enough to prevent the heating of the structure of the shell behind it. It can be seen that the required temperature for the outer wall reduces in a non-linear manner as the combustion chamber wall temperature increases. Figure 4.6b also has outer wall values of 0 for inner wall temperatures up until 1200, the reason for this is that the outer wall temperature is higher than the inner wall temperature which is impossible even with an infinitely small shell thickness, which is assumed for the calculation of the figure. Some assumptions that were made are the following, the inner shell surface area is equal to the outer wall surface area, which underestimates the radiation area for radiation cooling, the emission coefficient is 1 making it a perfect black body which overestimates the emissivity of the material. Also, the conduction coefficient of the shell affects the temperature of the wall where: $q = -k\frac{\Delta T}{\Delta x}$, for a given heat flow this means that $\Delta T = q \cdot \frac{\Delta x}{k}$. The temperature of the outer wall is therefore overestimated. The combination of the underestimated outer wall due to conduction and the lower emission coefficient reduces the radiation capabilities. The Epoxy-Kevlar that is used for the shell because of its high tensile strength and low density cannot withstand these temperatures. Therefore an ablative material was selected.

Let us now consider the nozzle design, where the procedure for the length of a bell nozzle is given by Zandbergen [107]. Let an intersection of a bell nozzle be represented in a 2-dimensional x,y-plane such that the length can be described as a function of the radius.

$$x = ay^2 + by + c \tag{4.99}$$

Where the parameters a, b, c can be calculated according to:

$$a = \frac{tan(\frac{\pi}{2} - \theta_e) - tan(\frac{\pi}{2} - \theta_p)}{2(y_e - y_p)} \tag{4.100}$$

$$b = tan(\frac{\pi}{2} - \theta_p) - 2ay_p \tag{4.101}$$

$$c = x_p - ay_p^2 - by_p \tag{4.102}$$

Where y_p, y_e, x_p, θ_p and θ_e are the values of the radius and distance from the throat at point P, If y_p, y_e, x_p, θ_p and θ_e are known, the function describing the contour of a bell nozzle can be approximated. For the values of θ_p and θ_e Rao's values for angles of nozzles can be used and thus follow from literature [79]. Also x_p and y_p are both functions of θ_p and the throat area, A_t. Note that y_e is the exit radius and thus related to the throat area through area ratio.

$$y_e = R_e = \sqrt{\frac{A_e}{A_t}} \cdot R_t \tag{4.103}$$

From a, b, c and y_e the length of the nozzle x_e directly follows by plugging the values into equation 4.99. If this function is integrated and then spun around the x-axis by multiplying with π the inner volume of the nozzle can be calculated:

$$V = \pi \int_{x_p}^{x_e} y^2 dx \tag{4.104}$$

As it is difficult to rewrite y as a function of x, a numerical approach can be taken such that:

$$V = \pi \sum_{i=1}^{n} y_i^2 dx \tag{4.105}$$

Where the step $dx = \frac{x_e - x_p}{n}$ with n being the total number of discrete values of x and y. The series y_i is known and is in the range (y_p, y_e). Adding the thickness of the nozzle to all values of y and plugging this new series into equation 4.105 gives the volume under the curve describing the outer radius of the nozzle. The mass then becomes:

$$m_{nozzle} = \rho_n V_{nozzle} = \rho_n (V_{outer} - V_{inner}) \tag{4.106}$$

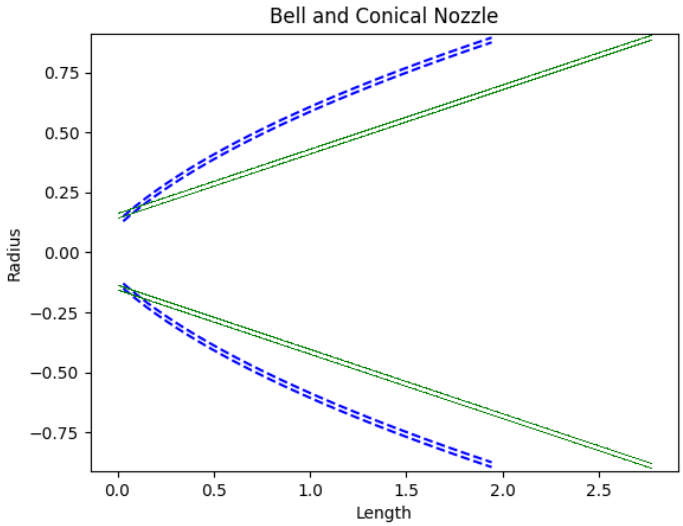

Figure 4.7: Length comparison of a bell and conical nozzle with the same area ratio using Rao's approach

4.3.5. PAYLOAD STRUCTURAL MASS

In this thesis, three types of payloads are considered: Hydrolox, oxygen, and ALICE. In the case of hydrolox, equations 4.63 - 4.70 are used to determine the payload structure. For oxygen equations 4.66, 4.67, 4.68 and 4.70 are used. In the case of ALICE propellant, the structural mass is estimated as follows:

$$m_{s,payload} = \rho_{t_{alice}} \cdot \left(4 \cdot \pi \cdot R^2 \cdot t\right) \tag{4.107}$$

Which is the surface area of the sphere times the thickness of the sphere, giving an approximate volume. Combining with the payload structure density gives the mass. The radius is calculated using the density and mass of the propellant. Note that this mass is only necessary for the last stage considering it is the one carrying the propellant to LEO.

4.3.6. HYDROLOX ROCKET DESIGN

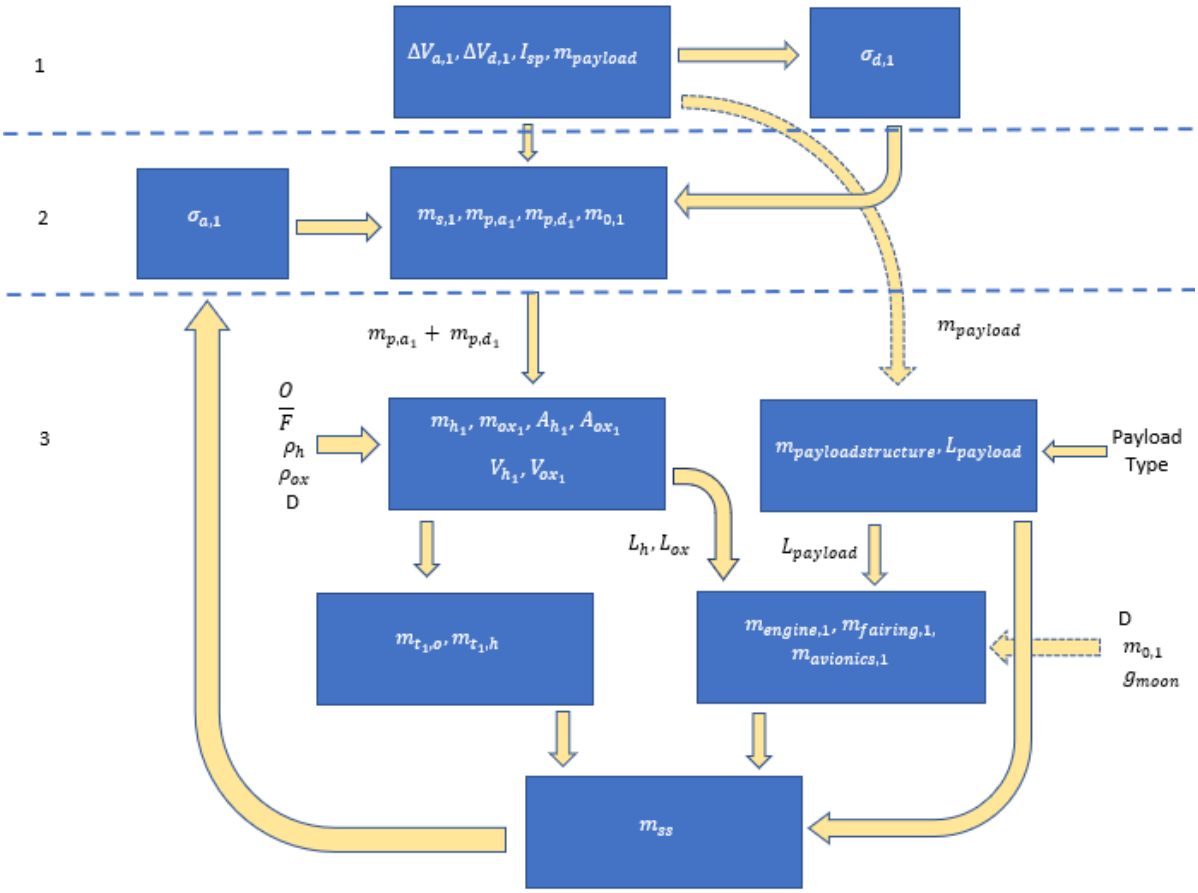

Figure 4.8: Algorithm mechanics hydrolox rocket

Figure 4.9: Input change from upper to lower stage

The algorithm above is divided into three layers. The first layer contains the mission design parameters from which the descending stage structural mass ratio can be directly deduced. In the second layer, the propellant mass, total mass, and structural mass are calculated based on a guess for the ascending stage structural

mass ratio. The third layer uses the values acquired in the first two layers, dimension parameters, propellant properties, and thrust requirements to calculate the mass of all structural subsystems, it repeats this for different structural mass ratios until the calculated structural mass equals the sum of the calculated masses of the subsystems. Figure 4.9 shows how the input block in layer 1 changes for the lower stage also the payload structural mass equals 0 for lower stages. For a two-stage rocket with stages $i = 1,2$, the lower stage is denoted by 2 and the upper stage by 1. For known ΔV, I_{sp} $m_{payload,1}$, $\sigma_{d,1}$, guessing a structural mass ratio, $\sigma_{a,1}$ gives an expression for the ascent stage propellant mass, m_{p,a_1} as can be seen in 4.53. Once this is known, the structural mass, m_{s,d_1}, and descent phase propellant mass, m_{p,d_1} can be derived. From the propellant mass, $m_{p,1} = m_{p,d_1} + m_{p,a_1}$, and the mass mixture ratio, $\frac{O}{F}$, the oxidizer and hydrogen mass follow as given by equations 4.64 and 4.63. From the fuel and oxidizer masses, their corresponding volumes are calculated. From these volumes the tank masses are estimated using the aforementioned numerical equations. The propellant tank, dimensions follow from the volume and radius of the rocket, which give the required length of each tank respectively. The surface area of the tanks follows directly from the dimensions and allows for the calculation of their insulator mass. The payload structural mass is calculated as described in section 4.3.5. The $m_{0,1}$ that was calculated by guessing the structural mass ratio, $m_{s,1}$, is used for the thrust and thus engine sizing. For the remaining subsystem masses, $m_{av,1}$ and $m_{fairing,1}$, an estimation of the length of the rocket is required, this is done by using equation 4.73. Now all masses are determined for the upper stage. If the sum of all these masses is equal to the guessed structural mass, $\sigma_{d,1}$ the algorithm has converged. The converged algorithm gives the total mass of the upper stage. This $m_{0,1}$ is now considered to be the payload mass, and the procedure above is repeated for the specified ΔV's of this stage. The avionics mass of the lower stage however is calculated using equation 4.72 but for the input parameter $m_{0,2}$. Not the GLOM (Gross Lift Off Mass) but only the total mass of the lower stage is used, thus not adding the upper stage mass. The graphs provided are the combined masses of each subsystem as it appears in the total rocket. Meaning that the graphs of the engine, fairing, engine, etc. are the sum of these systems from the upper and lower stage combined.

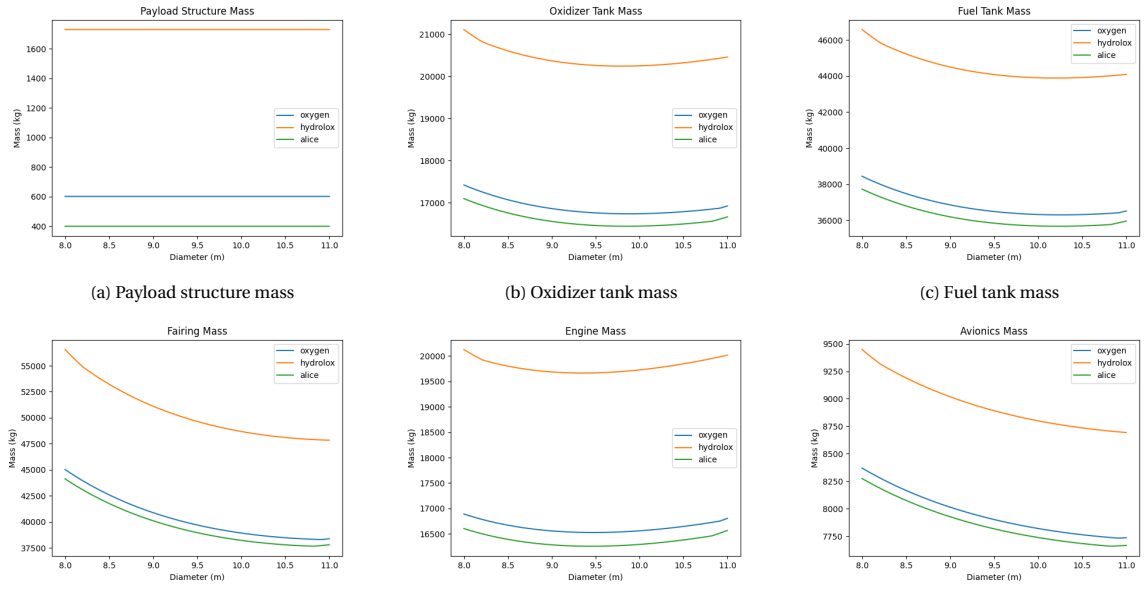

(a) Payload structure mass

(b) Oxidizer tank mass

(c) Fuel tank mass

(d) Fairing mass

(e) Engine mass

(f) Avionics Mass

Figure 4.10: Hydrolox rocket subsystem masses

As can be seen in 4.10, the payload structural mass remains constant as the payload mass is a design parameter and therefore the payload structural mass follows. The figure shows how the different subsystem masses are affected by the change in the diameter of the rocket. In general, the an increase in the diameter increases the oxidizer tank mass and the fuel tank mass, but decreases the avionics and fairing mass. The behaviour of the engine mass is explained by the total mass and thrust requirements. The engine mass minimum corresponds to the total mass minimum.

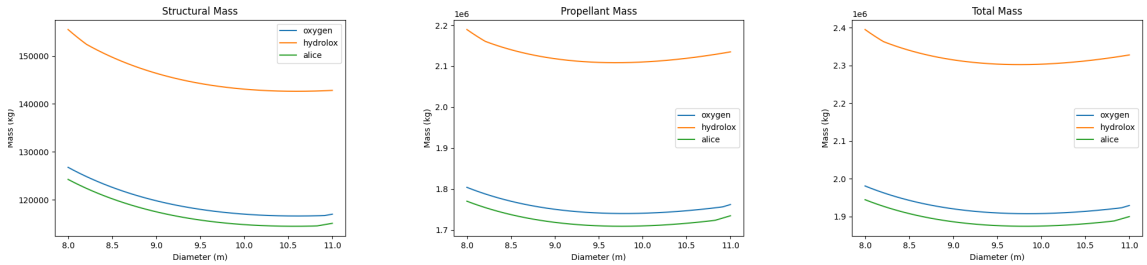

(a) Structural mass (b) Propellant mass (c) Total mass

Figure 4.11: Structural, propellant and total mass of the hydrolox rocket as a function of the rocket diameter

The behavior of the three rocket characteristics as seen in figure 4.11 is very similar which is not surprising considering propellant mass and total mass scale with structural mass.

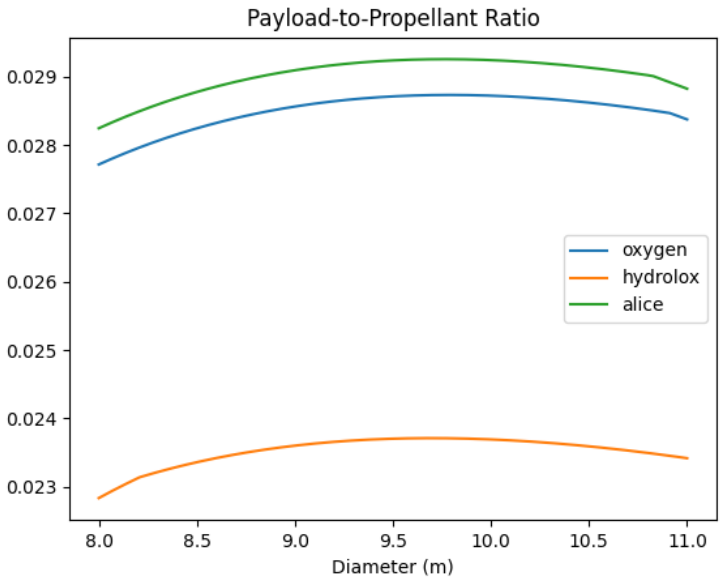

Figure 4.12: Payload-to-Propellant ratio of a hydrolox rocket carrying various payloads

Figure 4.12 shows how the payload-to-propellant ratio of the hydrolox rocket as a function of the it can be seen that the payload-to-propellant ratio of the rocket is highly dependent on the type of propellant it is carrying, this is due to the density of that specific payload. A higher density is more compact and requires a smaller payload structure. Especially carrying hydrolox is inefficient, considering it requires two separate tanks that also both require insulation.

Hydrolox Rocket	ALICE	Oxygen	Hydrolox
PTP	2.93 %	2.87 %	2.24 %
PTP-inverse	34.2	34.8	42.2

Table 4.5: Hydrolox Rocket Payload-to-Propellant ratio for different types payloads

That maximum PTP-ratio (payload-to-propellant ratio) of the three payloads are given in table 4.6. The inverse values of these ratios give the number unit masses of expelled propellant for a unit mass of the specified payload that is carried to LEO from the lunar surface.

4.3.7. ALICE ROCKET DESIGN

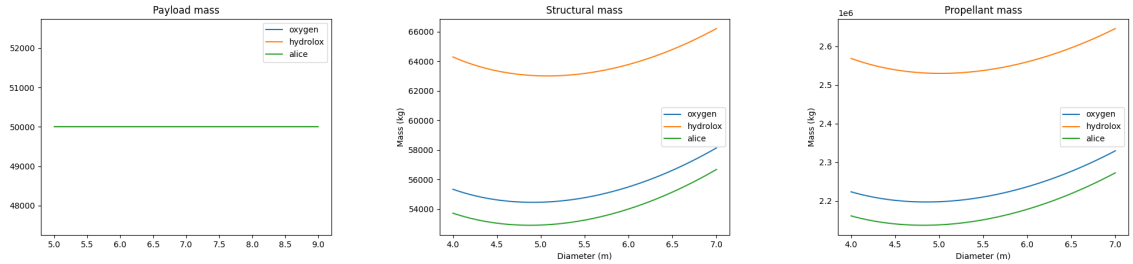

(a) The payload mass as a function of the diameter of the rocket

(b) The structural mass as a function of the diameter of the rocket

(c) The propellant mass as a function of the diameter of the rocket

Figure 4.13: Rocket mass breakdown

The computational method outlined in figure 4.5 was employed to analyze the ΔV requirements for a payload mass of 50000 kg, as presented in table 4.3. The resulting calculations yielded the values, which are shown in figure 4.13. These results can be used to evaluate the feasibility and efficiency of space missions for the given payloads. The payload mass, as indicated in 4.13a, is a fundamental design parameter that remains constant at 50000 kg for all diameters. This ensures that the payload-to-orbit requirements are met consistently across all mission configurations, and enables more accurate comparisons and evaluations of mission feasibility and performance. Upon analyzing figure 4.13b, it becomes apparent that the structural mass of the rocket is heavily influenced by the diameter, leading to a range of values for the transportation of ALICE, oxygen, and hydrolox.

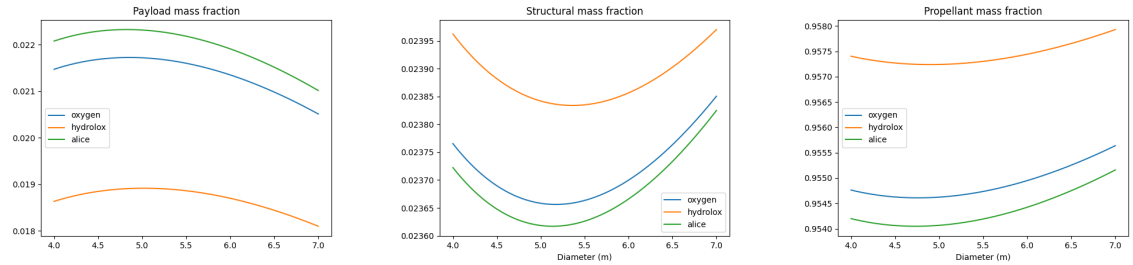

(a) The fraction of the payload as a function of the diameter of the rocket

(b) The fraction of the structural mass as a function of the diameter of the rocket

(c) The fraction of the propellant as a function of the diameter of the rocket

Figure 4.14: Rocket fractional mass breakdown

The ratio of the payload, structural and propellant mass as a fraction of the total spacecraft mass is found in 4.14. The values correspond to a payload, structural, and propellant mass range from 0.0253-0.0281, 0.0238-0.0243 and 0.948-0.950 for ALICE, 0.0247-0.0273, 0.0239-0.0244 and 0.949-0.951 for oxygen, and 0.0220-0.0238, 0.0242-0.0246 and 0.950-0.953 for hydrolox. These ranges correspond to percentage differences of 10.9 %, 2.16 %, and 0.238 % for the payload, structural and propellant fraction for the ALICE-carrying spacecraft. For the oxygen-carrying spacecraft, these ranges correspond to percentages difference of 10.4 %, 1.96 %, and 0.221 % for the payload, structural and propellant fraction for the oxygen-carrying spacecraft. The percentage differences of 8.08 %, 2.16 %, and 0.151 % correspond to the payload, structural and propellant fraction of the hydrolox-carrying ALICE rocket.

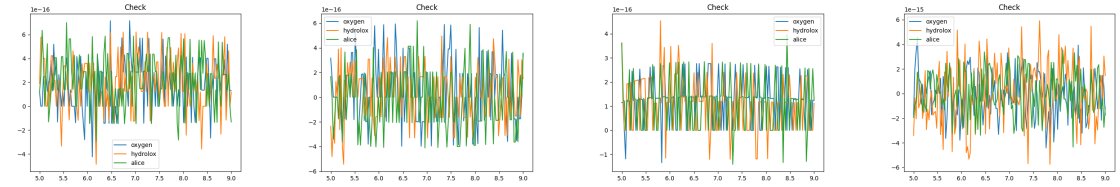

(a) Error of the ascending phase of stage 1 (b) Error of the descending phase of stage 1 (c) Error of the ascending phase of stage 2 (d) Error of the descending phase of stage 2

Figure 4.15: Error of convergence

Figure 4.15 checks whether the calculated mass values follow the constraints put on them by the Tiolkovky rocket equation, in the following manner.

$$\mu_{asc,i} = m_{0,i} \cdot e^{-\frac{\Delta V_a}{v_e}} - m_{f,i} \tag{4.108}$$

$$\mu_{desc,i} = m_{0_{desc},i} \cdot e^{-\frac{\Delta V_d}{v_e}} - m_{s,i} \tag{4.109}$$

For every stage, i, there are two errors that are being considered, firstly the error related to to the ascending phase and secondly the error related to the descending stage. $m_{f,i}$ is the final mass of stage i after the ascend phase burn, which can be calculated using the Tiolkovky rocket equation, this value, however, is also given by the algorithm as $m_{f,i} = m_{0,i} - m_{p,a_i}$. For the descending phase burn, the mass at the beginning of the burn is required which is given by the algorithm as $m_{0_{desc},i} = m_{f,i} - m_{pay,i}$. Again using the Tiolkovky rocket equation, with the descent phase ΔV should give the value of an empty rocket stage on the lunar surface which is equal to the structural mass, $m_{s,i}$. Note that the value should be 0 otherwise the algorithm converges to a solution that does not meet the constraints. All values depicted in 4.15 are negligibly small in the order of magnitude of 10^{-16}.

4.3.7.1 STRUCTURAL MASS

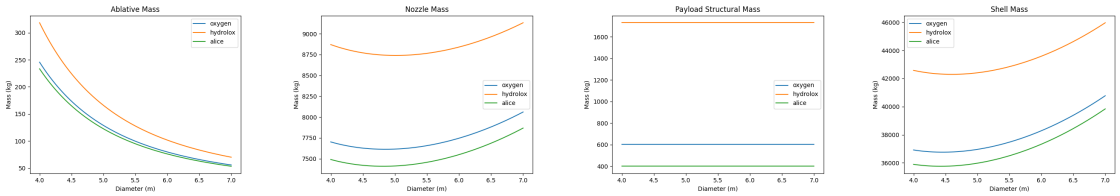

(a) The payload mass as a function of the diameter of the rocket (b) The structural mass as a function of the diameter of the rocket (c) The propellant mass as a function of the diameter of the rocket (d) The propellant mass as a function of the diameter of the rocket

Figure 4.16: Multi-stage structural mass breakdown

The structural mass of the rocket is composed of several subsystems that are each affected by the rocket's diameter, sometimes in conflicting ways. Together, these subsystems contribute to the overall behavior of the rocket's mass. As the diameter of the solid rocket increases the ablative mass required for the ablative cooling of the rocket decreases, this is because the convection heat to the chamber wall is inversely related to the diameter of the combustion chamber as seen in 4.16a.

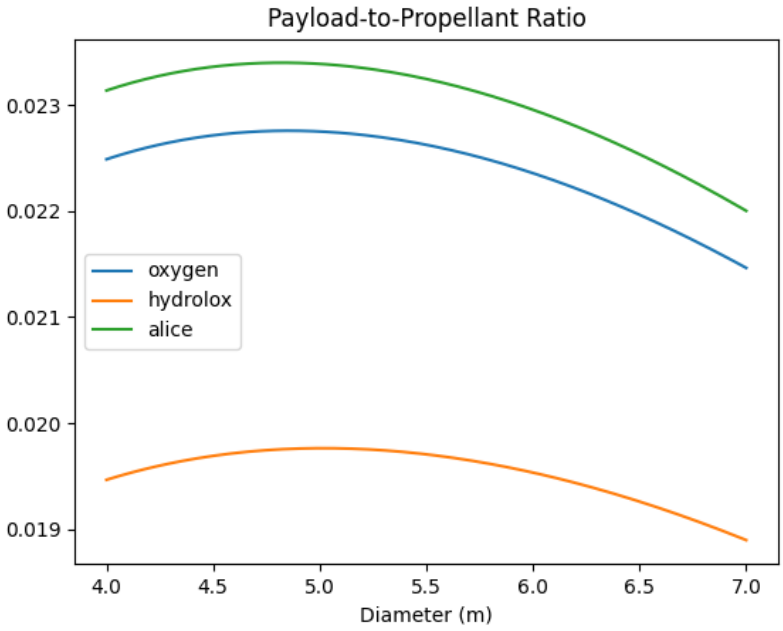

Figure 4.17: Payload-to-propellant ratio of ALICE rocket

ALICE Rocket	ALICE	Oxygen	Hydrolox
PTP	2.23 %	2.17 %	1.89 %
PTP-inverse	44.8	46.0	52.9

Table 4.6: ALICE Rocket Payload-to-Propellant ratio for different types payloads

The payload-to-propellant ratio is 1.89 %, 2.17 %, and 2.23 % for hydrolox, oxygen and ALICE, respectively.

4.3.8. PROPELLANT DEPOT

Let us now consider the construction of a propellant depot in the future, such a structure is placed into an orbit where the air is very thin, since the effect of atmospheric drag is then very low, which otherwise could over time result in serious orbital decay[47].

$$\frac{dR}{dt} = \frac{\alpha_0(R) \cdot T(R)}{\pi} \tag{4.110}$$

Where $\frac{dR}{dt}$ describes the change in orbital height w.r.t. time. Also, $\alpha_0(R)$ and $T(R)$ indicate the drag deceleration and period as a function of the orbital radius R. The drag deceleration can be described by:

$$\alpha_0 = \frac{1}{2} \cdot \rho(R) \cdot v^2(R) \cdot c_d \cdot \frac{A_{pro}}{m} \tag{4.111}$$

where the density, $\rho_a(R)$ is the density of air at R, $v(R)$ is the orbital velocity at R. c_d, A_{pro} and m are the drag coefficient, effective drag area and the mass respectively. Using Kepler's third law the period at R is:

$$T(R) = \sqrt{\frac{4\pi^2}{\mu_{Earth}} R^3} \tag{4.112}$$

One way to mitigate this is to add a micropropulsion device such as an ion thruster that cancels out the atmospheric force acting on the structure. This could be mitigated by adding a propulsion system to the propellant station, this would complicate the system considering a chemical thruster generally provides a much higher thrust changing the orbit [23]. However, the occurring drag can greatly reduce the mission

time. This can be explained by looking at 4.110 and 4.111. 4.110 is a function of the drag coefficient that is dependent on the altitude density, $\rho_a(R)$, as can be seen in 4.111. As the orbit decays the density rises resulting in faster decay which rapidly becomes unfeasible as can be seen in the case of Tiangong-1 [70].

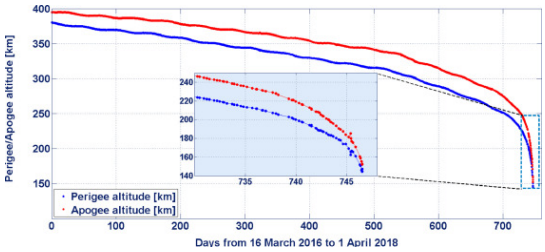

Figure 4.18: Tiangong-1 orbital decay

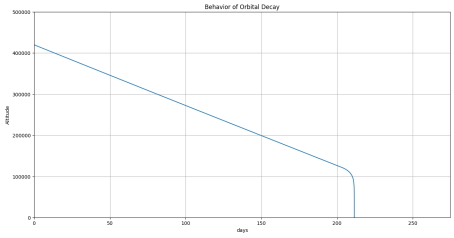

Figure 4.19: modeled behavior of atmospheric drag on a mass in LEO

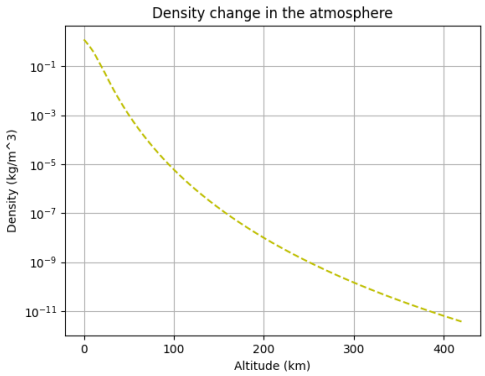

Figure 4.20: Atmospheric density as a function of altitude

The behavior of the spacecraft in fig. 4.18 can be explained by the atmospheric drag continuously applying a small force. This results in a lower orbit in which the mass is subject to a higher atmospheric drag due to the increased density at lower altitudes. As can be seen in fig. 4.20 the density of the atmosphere soars exponentially and increases 12 orders of magnitude from the parking orbit to the Earth's surface. Applying the density model as described in Appendix C, the behavior of a similar case can be modeled as can be seen in 4.19.

A propulsion system could be added to the system to prevent decay. This would however complicate the system. Also, a chemical thruster provides higher thrust and works with discrete burns, a cold gas thruster has a low specific impulse and also is difficult to finetune such that it can precisely counter the very weak force acting on the structure. Closely monitoring the decay and adjusting the orbit accordingly after some time is an option as was done with the ISS, where a ΔV maneuver of 1.32 $\frac{\text{m}}{\text{s}}$ is performed once a month. One way to mitigate this is to add a micropropulsion device such as an ion thruster that exactly cancels out the atmospheric force acting on the structure [23].

Therefore the propellant depot will be residing at the altitude range where current space stations are also operating, it will be assumed that the orbit is circular and has an altitude of 420 km [22].

4.3.8.1 SPACE WEATHER

The fluctuations in solar activity, commonly known as space weather, have a significant impact on various space operations, including station keeping. It is possible to make estimations regarding the exergy destruction, associated with the station-keeping process in light of these solar activity variations. Such estimations can help in better understanding and managing the impact of space weather on the performance of space systems.

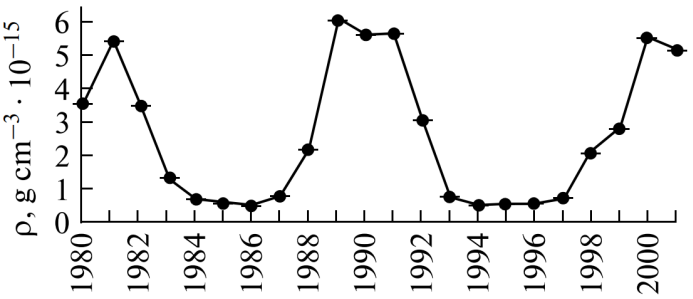

Figure 4.21: Effect of the solar cycle on air density of the upper atmosphere [10]

The figure 4.21 shows that the density in the upper atmosphere fluctuates in the range of approximately $0.5 - 6 \cdot 10^{-12} \frac{kg}{m^3}$, with an average value of about $2.5 \cdot 10^{-12} \frac{kg}{m^3}$ [10]. Given these density values, it is possible to express the fluid pressure as a combination of the drag equation, as given in equation 4.111, and Newton's second law of motion. This approach can be used to study the behavior of objects moving through the upper atmosphere under different conditions, including variations in atmospheric density.

$$\frac{F}{A_{pro}} = \frac{1}{2} \cdot \rho_{air} \cdot c_d \cdot v^2 \tag{4.113}$$

Now the drag coefficients of elliptical cylinders that depend on the ratio of the semi-major and the semi-minor axis of the shape, are considered,

$\frac{a}{b}$	1	2	4	8
c_d	0.3	0.2	0.15	0.1

Table 4.7: Drag coefficient of various elliptical cylinders[30] [11].

Assuming the propellant depot has an elliptical shape the behavior of the drag force can be estimated if the dimensions of the specific ellipse are known.

Figure 4.22: Projected Area

Now we require a way of knowing the volume and effective area of the given elliptical cylinders. The formulas for calculating the volume and effective area are given by:

$$V = \frac{4}{3} \cdot \pi \cdot a \cdot b \cdot c \tag{4.114}$$

Also,

$$V = \frac{m_{prop}}{\rho_{prop}} \tag{4.115}$$

where a, b and c are the semi-axes of the respective elliptical cylinder. It is assumed that the 2-D semi-minor axis b is equal in length to the three-dimensional third semi-axis c. Then the projected area has a circular shape and is shown in fig. 4.22.

$$A_{pro} = \pi \cdot b \cdot c = \pi \cdot b^2 \tag{4.116}$$

Also, it is known that the ratio of the axes is related to the drag coefficient, so for a given $\tau = \frac{a}{b}$ the drag coefficient is known. Substituting this relation into 4.114 gives the following relation:

$$b = \left(\frac{3 \cdot m_{prop}}{4 \cdot \pi \cdot \rho_{prop} \cdot \tau} \right)^{1/3} \tag{4.117}$$

Since m_{prop} and ρ_{prop} are design parameters and are therefore known, the semi-minor axis, b, can be readily computed. The area A_{pro} follows directly and is then used in equation 4.116. Giving an approximation of the required force for station-keeping. Now an ion-thruster is used to counteract the drag given by:

$$F = \dot{m}_{ion} \cdot V_{e,ion} \tag{4.118}$$

Where $\dot{m}_{ion}$ and $V_{e,ion}$ are the mass flow and exhaust velocity of the ion engine. Attaching an ion-thruster, using krypton with a specific impulse, $I_{sp} = 2090$ s [71] gives the mass flow required for station-keeping, since the thrust generated by the ion engine should counteract the drag force acting on the propellant depot.

$$\dot{m}_{ion} = \frac{\frac{1}{2} \cdot \rho_{air} \cdot c_d \cdot v^2 \cdot A_{pro}}{I_{sp} \cdot g_0} = \frac{\frac{1}{2} \cdot \rho_{air} \cdot c_d \cdot v^2}{I_{sp} \cdot g_0} \pi \cdot \left(\frac{3 \cdot m_{prop}}{4 \cdot \pi \cdot \rho_{prop} \cdot \tau} \right)^{2/3} \tag{4.119}$$

Where g_0 is the gravity acceleration of the Earth. Also, the related energy requirement of the krypton thruster can be calculated using the thrust-to-power ratio, $\frac{T}{P}$, which is 42 $\frac{\text{mN}}{\text{kW}}$ [71]. Therefore, the electrical power requirement of the krypton thruster can be calculated using:

$$E_e = F \cdot \frac{P}{T} \tag{4.120}$$

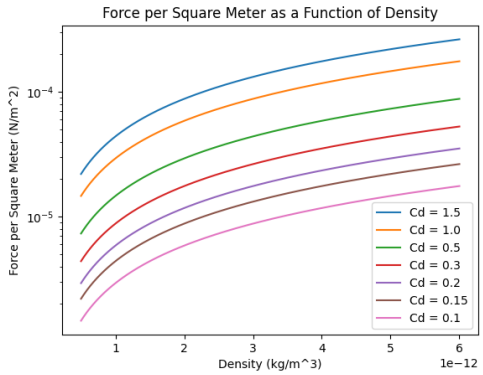

Figure 4.23: Force acting on the propellant depot per square meter of effective area as a function of air density for different drag coefficients

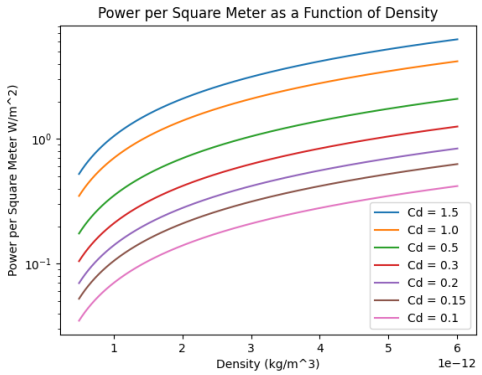

Figure 4.24: Power requirement of the ion thruster per square meter of effective area as a function of air density for different drag coefficients

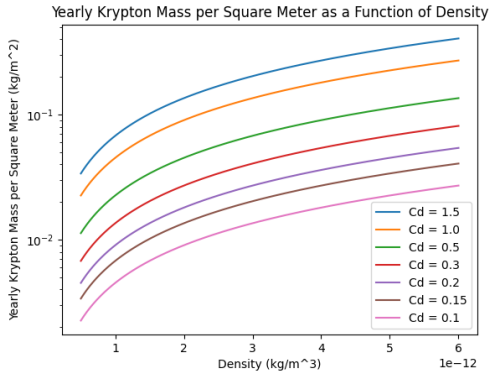

Figure 4.25: Propellant mass requirement of the ion thruster per square meter of effective area as a function of air density for different drag coefficients

The graphs depicted in figure 4.25 are expressed per square meter of effective area, this is done such that it can be applied to all designs of propellant depots. The expected force per square meter, power per square meter, and yearly krypton per square meter are in the ranges $10^{-6} - 3 \cdot 10^{-4}$ $\frac{\text{N}}{\text{m}^2}$, $3.5 \cdot 10^{-2} - 7$ $\frac{\text{W}}{\text{m}^2}$ and $2 \cdot 10^{-2} - 4 \cdot 10^{-1}$ $\frac{\text{kg}}{\text{m}^2}$ respectively. The drag coefficient and air density have a strong effect on the force, power, and krypton requirements which span over multiple orders of magnitude.

Looking at eq. 4.116, 4.117, 4.119. It can be seen that the required mass flow rate of the ion engine scales as given by:

$$\dot{m}_{ion} \sim m_{prop}^{\frac{2}{3}} \tag{4.121}$$

which means that the ratio behaves in the following manner:

$$\frac{\dot{m}_{ion}}{m_{prop}} \sim m_{prop}^{-\frac{1}{3}} \tag{4.122}$$

Therefore a bigger propellant depot is more beneficial in terms of the power-to-propellant and the krypton-to-propellant ratio.

Let us consider a propellant depot that has $\tau = 2$ and $m_{prop} = 500000$ kg, that follows the procedure as described in section 4.3.8.1.

	$\rho\ (\frac{kg}{m^3})$	$A_{pro}\ (m^2)$	$P\ (W)$	$P_J\ (\frac{J}{kg})$	$m_{krypton}\ (kg)$
Oxygen	1140	44.0	15.4	484.8	0.497
Hydrolox	363	94.3	32.9	1040	1.07
ALICE	1370	38.9	13.6	428.8	0.439

Table 4.8: Propellant depot characteristics for oxygen, hydrolox, and ALICE storage

Unsurprisingly, the propellant density is the biggest driver of the sizing, and thus the projected area, krypton mass, and power requirements. Note that the density of hydrolox is calculated using a mass mixture ratio of 6.03 and the densities of liquid oxygen and hydrogen respectively. Also, P was converted based on a half year of storage, T. Therefore, $P_J = \frac{P \cdot T}{m_{prop}}$, and are 0.423, 0.485 and 1.04 $\frac{\text{kJ}}{\text{kg}}$ for ALICE, oxygen and hydrolox, respectively. This corresponds to a krypton mass consumption of 0.439, 0.497 and 1.07 kg.

5

Environment and Thermodynamic Properties

5.1. Environment

The operating conditions of the Moon are of interest considering they are a key driver in the performance of a propellant-generating architecture on the Moon. The temperature and pressure as well as the mineralogical conditions in which a system has to operate greatly influence the design route and characteristics. Furthermore, the limited resources and harsh environmental conditions on the Moon present unique challenges for the design and operation of propellant-generating architectures. For instance, the absence of a significant atmosphere and magnetic field on the Moon exposes any infrastructure to high levels of radiation and micrometeoroid impacts, requiring systems to be designed with adequate shielding and protection.

In addition, the resource constraints on the Moon mean that any propellant-generating architecture must be able to operate using locally available materials, such as regolith or ice. These materials have distinct physical and chemical properties that affect the selection of processes and equipment used to extract and process them.

Overall, an understanding of the operating conditions on the Moon is essential for designing efficient and effective propellant-generating architectures. By accounting for the unique challenges presented by the Moon's environment and resource constraints, these architectures can help support sustained human presence on the Moon and beyond. Moreover, the operating conditions of the Moon also impact the reliability and longevity of propellant-generating systems. Extreme temperature fluctuations can cause material fatigue and wear, leading to system failure over time. Additionally, the low atmospheric pressure on the Moon can cause leaks and structural failures in propellant generation equipment, as well as affect the operation of pumps and valves.

Therefore, designing a reliable and robust propellant-generating architecture for the Moon requires careful consideration of the operating conditions, as well as the selection of appropriate materials, equipment, and design features that can withstand these conditions over extended periods.

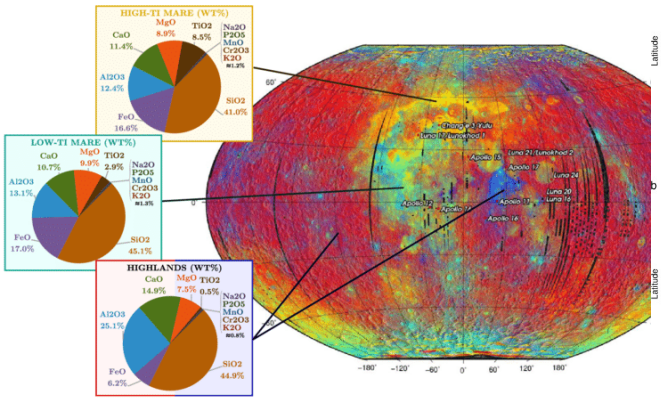

(a) Chemical composition of regolith on various locations on the Moon[88]

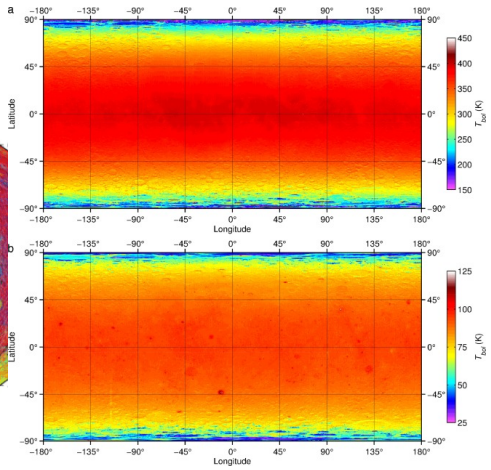

(b) a. Maximum and b. minimum global temperatures[104].

Name	Selenographic	Diameter (km)	Depth (km)
Shackleton	89.9° S 0.0° E	21	4.2
Shoemaker	88.1° S 44.9° E	50.9	2.5
Erlanger	86.94° N 28.62° E	9.9	
Sylvester	82.7° N 79.6° W	58	NA
Cabeus	84.9° S 35.5° W	98	4
Rozhdestvenskiy	85.2° N 155.4° W	177	NA

(c) Crater locations and dimensions[55]

Location	Selenographic	Relative Sunshine Duration
Shackleton crater rim, point A	89.68° S 166.0° W	162%
Shackleton crater rim, point B	89.44° S 141.8° W	164%
Gerlache crater rim	88.71° S 68.7° W	170%
Shackleton crater rim, point C	88.79° S 124.5° E	172%
Malapert mountain A	86.04° S 2.7° E	148%
Malapert mountain B	86.00° S 2.9° W	148%

(d) Relative Sunshine Duration and locations of peaks of eternal light [55]

Figure 5.1: Lunar Environment Specifications

The temperature of the lunar surface varies greatly depending on location and time. Latitude and temperature exhibit a strong correlation, as shown in figure 5.1b. The temperature on the Moon ranges from 40K to 350K [104], with some spots experiencing even more extreme temperatures, both hot and cold. At very high latitudes, the angle of incidence is so low that craters experience eternal darkness, creating energy-deprived spots where water has not escaped. Such spots are ideal for mining, as demonstrated in the bottom left figure. The bottom right corner shows the Peaks of Eternal Light, where relative sunshine duration varies from 148-172%, with 100% defined as the sunshine duration of one average lunar day [55]. The sunshine exposure ranges from 74-86%. The dimensions of the permanently shadowed regions (PSRs) and peaks of eternal light (PELs) are important factors to consider, as demonstrated in figure 5.1, as they offer potential storage and resource opportunities.

The Shackleton crater contains several PELs and a large PSR [55], making it a focus of lunar programs such as those of the United States and China [38, 64]. Local geography also plays a significant role in determining the temperature of each location on the Moon, as the heat capacity of soil and rock composition affects temperature.

As can be seen in fig. 5.1a the lunar environment consists almost exclusively of oxides, only the proportion of these oxides varies to a degree depending on the specific location on the Moon [88], it should be noted that there are some indications that both rare earth metals and helium-3 among others can be found on the Moon [21, 58]. For the purpose of propellant generation of both ALICE and hydrolox, water is required, therefore the lunar south pole is chosen. Currently, it is assumed that highlands regolith and regolith near the poles have comparable chemical composition. Additionally, it should be added that the PSRs contain water since the temperature is assumed to be 40 K and constant due to the lack of sunlight. The water content present in these PSRs varies as demonstrated by the LCROSS mission, however, the mean of the spectrometric data indicates that a weight percentage of 5.6 % should be expected [14].

	symbol	value
Environment Temperature	T_0	40K
Pressure	p_0	3e-15 bar
Composition of atmosphere	y_{atm}	N.A.
Compostion of lithosphere		
Water ice	y_{H_2O}	5.6 %
Highlands regolith	$y_{regolith}$	94.4 %

Table 5.1: Conditions an composition of the PSR environment

When looking at the composition of the lithosphere in terms of water and oxides the following distribution is expected.

	SiO_2	Al_2O_3	CaO	MgO	TiO_2	FeO	H_2O
$\%w$	42.8	23.9	14.2	7.14	0.476	5.91	5.60

Table 5.2: Composition of the regolith present in the PSRs

These values are based on the oxide concentrations for highlands regolith as depicted in figure 5.1a, it is thought that highlands regolith most resembles regolith present near the south pole. Combining the expected 5.6 % water ice with 94.4 % highlands regolith, the results in table 5.2 are found. The temperature, pressure, and composition in the tables above will be used in the calculations throughout this thesis.

5.2. THERMODYNAMIC PROPERTIES

The elements and weights of the environment are now known, therefore the molar fraction of each element in the lithosphere can be calculated:

$$n_{el} = \frac{\sum \eta_{el,m}\eta_{m,l}}{M_{el}} \tag{5.1}$$

Where $\eta_{el,m}$ is the weight percentage of the element in a molecule that contains that element and $\eta_{m,l}$ is the weight percentage of the molecule in the lithosphere, applying this principle to all molecules in the lithosphere containing the element of interest gives the expression $\sum \eta_{el,m}\eta_{m,l}$, which is the weight percentage of an element in the lithosphere. After dividing this number by the molar mass of the element the molar fraction can be derived. The molar mass will be applied to derive the chemical exergy of the oxides present in the reference environment.

	Si	O	Al	Ca	Mg	Ti	Fe	H
w% element	20.00	47.40	12.65	10.14	4.31	0.3	4.59	0.622
n_{el} $\frac{kmol}{kg}$	7.12e-3	2.96e-2	4.69e-3	2.53e-3	1.77e-3	5.96e-5	8.22e-4	6.22e-3

Table 5.3: Weight percentage of elements and molar concentration in the lithosphere

The standard specific chemical exergy of the oxides present in the lithosphere can be calculated as proposed by Szargut [95, 96], where the principle of an ideal mixture is applied to the solids in the lithosphere.

$$ex_m^{ch} = -RT_{env} \cdot ln(x_{in}) \tag{5.2}$$

where R is the gas constant, T_{env} is the temperature at the dead state and x_{in} is the mean molar fraction of the reference species in the lithosphere. This fraction can be calculated using an element present in the reference species.

$$x_{in} = \frac{1}{l_i} n_{el} c_i M_0 \tag{5.3}$$

Where l_i, is the number of atoms of the element in the reference species, c_i is the fraction of the element appearing in the form of the reference species, values where taken from Szargut [96], n_{el} ($\frac{kg}{mol}$)is the mean molar concentration of the element i and M_0 is the molar mass of the lithosphere ($\frac{mol}{kg}$). For example, let us

consider the case of silicon oxide. In the case of SiO_2, we look at silicon which has one atom in the molecule. Therefore, $l_i = 1$, $n_{el} = 7.12e-3$ $\frac{kmol}{kg}$, $M_0 = 151$ $\frac{kg}{kmol}$ and $c_i = 0.3$ taken from Szargut [96]. Plugging these values into eq. 5.3 and eq. 5.2 with $T_{env} = 40$ K gives $ex_0^{ch} = 0.375$ $\frac{kJ}{mol}$. Note that in the case where the composition is constant, the exergy scales only with temperature, Szargut has documented values for standard conditions on Earth, with a temperature of the environment of 298 K. Therefore the value of the chemical exergy should differ by a factor $\Phi = \frac{298}{40} = 7.45$. The chemical exergy of SiO_2 expected for the same composition on Earth would then be 2.79 $\frac{kJ}{mol}$, which is comparable to the 2.2 $\frac{kJ}{mol}$ tabulated by Szargut [96].

Using the values in table 5.3 and equations 5.2 and 5.3 gives the standard chemical exergy of the reference species present in the environment.

Reference species	ex_0^{ch} $\frac{\text{kJ}}{\text{kmol}}$	ex_0^{ch} $\frac{\text{kJ}}{\text{kg}}$
SiO_2	375.5	6.25
Al_2O_3	2106.4	20.66
CaO	1850.5	33.00
MgO	1738.4	43.13
TiO_2	3097.0	38.78
FeO	1458.7	20.30
H_2O	1016.1	56.45

Table 5.4: Standard Chemical Exergy of Oxides present in the regolith

For molecules not present in the environment the chemical exergy is obtained by analyzing a reaction of that molecule with a substance in the reference environment.

The values for latent heat, Gibbs free energy, viscosity, enthalpy entropy, heat capacity, and thermal conductivity of the chemical compounds can be found in the JANAF tables and NIST Webbook [12] in either thermodynamic tables or numerical approximations. These approximations are expressed as polynomials that take the form:

$$c_p(t) = A + B\cdot\theta + C\cdot\theta^2 + D\cdot\theta^3 + \frac{E}{\theta^2} \tag{5.4}$$

$$H(t) = A\cdot\theta + B\cdot\theta^2 + C\cdot\theta^3 + D\cdot\theta^4 - \frac{E}{\theta} + F - H \tag{5.5}$$

$$s(t) = A\cdot ln(\theta) + B\cdot\theta + C\cdot\frac{\theta^2}{2} + D\cdot\frac{\theta^3}{3} - \frac{E}{2\cdot\theta^2} + G \tag{5.6}$$

Where c_p, H and s are the heat capacity, enthalpy, and entropy respectively and θ is the temperature of the substance divided by 1000. The coefficients for a specified substance can be found in the NIST Webbook.

These might however in some specific cases not be sufficient because the values are not provided for very low temperatures. One such case is water where the value of water ice is not provided. This can be mitigated using the following procedure to approximate the values for both enthalpy and entropy.

In the case that there is no phase change the enthalpy change is:

$$\Delta H = c_p \Delta T \tag{5.7}$$

The equation above states that if the heat capacity remains constant between two temperatures the enthalpy change is proportional to that temperature change, ΔT and for the entropy:

$$\Delta S = c_p ln\left(\frac{T_2}{T_1}\right) \tag{5.8}$$

Again for a constant heat capacity the behavior of the entropy only depends on the initial, T_1 and final temperature, T_2 of the substance. The average heat capacity is found in literature and assumed to be constant for a given substance at a specified phase. The heat capacity used for a given substance depends on the magnitude of the temperature difference. For small ΔT, in the order of tens of kelvins, the lowest available heat capacity of the substance is taken. In the case of bigger ΔT, exceeding 100 K, heat capacity values for T_1 and T_2 are averaged and taken constant in the range ΔT.

In the case of a phase change, an additional term should be added.

$$\Delta H = c_p \Delta T \pm L \tag{5.9}$$

Where L is the latent heat of fusion, vaporization or both. For the entropy this the phase change affect the entropy in the following way:

$$\Delta S = c_p ln\left(\frac{T_2}{T_1}\right) \pm \frac{L}{T_p} \tag{5.10}$$

where T_p is the temperature at which the phase change occurs. It should be stressed that the heat capacity can greatly vary between phases and therefore also changes after the phase change.

The enthalpy of all substances of interest can now be calculated for a given state of which the most important one is the dead state where the substances are in thermomechanical and chemical equilibrium with the environment.

6

RADIATION

6.1. MULTI-LAYER INSULATION

Multilayer insulation (MLI) is a type of thermal insulation used in spacecraft and other applications where very low temperatures need to be maintained. It consists of alternating layers of reflective material and low-emissivity material, with the reflective layers facing outwards to reduce radiative heat transfer.

The absorptivity coefficient is a measure of how much radiation a material absorbs relative to how much it reflects. In the case of MLI, we want the absorptivity coefficient to be as low as possible, since any absorbed radiation will be re-radiated and can increase the temperature of the tanks. The emissivity and absorptivity of the MLI are important parameters for to calculate insulation capabilities and are depicted by α and ϵ, where α is the absorptivity coefficient and ϵ the emission coefficient. These coefficients can be determined experimentally or through theoretical calculations based on the optical properties of the materials used.

To calculate the overall absorptivity coefficient of the MLI, we need to take into account the multiple layers and their arrangement. This can be done using a mathematical model that takes into account the reflectivity and transmissivity of each layer, as well as the number and thickness of the layers.

It is important to note that the actual absorptivity coefficient of the MLI will also depend on factors such as the temperature and wavelength of the radiation, as well as the orientation of the insulation relative to the radiation source. Therefore, accurate calculations of the absorptivity coefficient of MLI require detailed knowledge of the application and its operating conditions.

Materials that are used for MLI applications include reflective materials such as aluminum, gold, and low-emissivity materials such as Mylar, Kapton, Bata cloth and quartz since they are lightweight and have low thermal conductivity [43] [56]. For an efficient production process, MLI is a vital component in the propellant-generating process in the harsh cold lunar environment.

6.2. PASSIVE COOLING

The lunar environment's lack of an atmosphere makes heat loss through convection without the use of an external fluid in addition to pump systems and heat exchangers impossible. Only radiation cooling is a feasible way of losing heat in a passive way. Radiation cooling follows a fourth power and is given by:

$$\frac{Q_r}{A_r} = \epsilon_r \sigma \cdot (T_r^4 - T_{env}^4) \tag{6.1}$$

Where $\sigma = 5.670374419 \cdot 10^{-8} \frac{W}{m^2 K^4}$ and A_r are the Stefan-Boltzmann constant and the radiator surface area. The emission coefficient of the radiating body, ϵ_r is set to 1 to analyze the case where the surfaces radiate the maximum amount of heat. Equation 6.1 is stating that the cooling of a body is proportional to the environment temperature T_{env}, the temperature of the radiating body, T_r, and the emission coefficient, ϵ_r and the surface area available for radiation cooling, A_r.

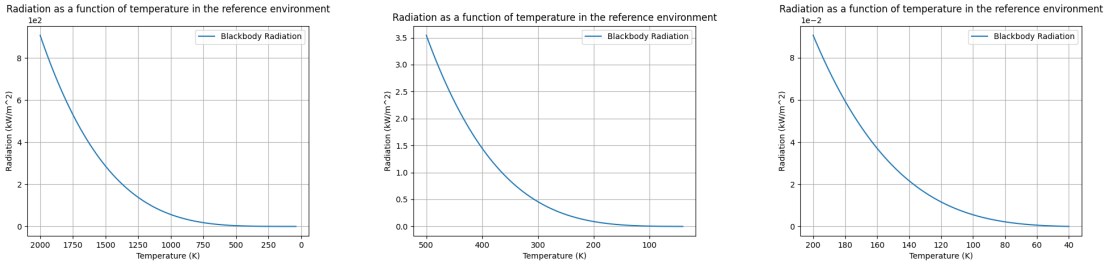

(a) Radiation flux between 40 and 2000 Kelvin (b) Radiation flux between 40 and 500 Kelvin (c) Radiation flux between 40 and 200 Kelvin

Figure 6.1: Radiation Cooling Behaviour

When looking at figure 6.1 it can be seen that the rate of radiation cooling exponentially decreases:

- Figure (a) depicts the radiation cooling behaviour in the temperature range $(2000-40\ K)$ where the rate of cooling varies by multiple orders of magnitude where the rate of cooling is around 900 $\frac{\text{kW}}{\text{m}^2}$ at 2000 K and has decreased to 100 $\frac{\text{kW}}{\text{m}^2}$ just above 1000 K. The cooling rate at these temperatures is relevant to the high temperature regolith melting processes during Molten Regolith Electrolysis and the subsequent treatment of the regolith products.
- Figure (b) depicts the radiation cooling behaviour in the temperature range $(500-40\ K)$, at 500 K the cooling rate approaches 3.5 $\frac{\text{kW}}{\text{m}^2}$ which is a 93 % decrease from 1000 K and then further decreases to about 1 $\frac{\text{kW}}{\text{m}^2}$ at 360 K. For most processes the operating temperatures fall within this range.
- Figure (c) depicts the radiation cooling behaviour in the temperature range $(200-40\ K)$, at 200 K the cooling rate is just under 0.1 $\frac{\text{kW}}{\text{m}^2}$ and decreases multiple orders of magnitude as it approaches the environment temperature. This is most relevant for the cooling of the propellant to cryogenic temperatures. The cooling rate at very low temperatures implies a longer cooling time required for the cooling of hydrogen in particular under the assumption that radiation surface remains constant.

The thermal modeling of cooling will not operate in a steady-state and is described in the following manner.

$$Q_j(t) = \epsilon_r \cdot \sigma \cdot A_{r,j} \cdot (T_r^4(t) - T_{env}^4) \cdot dt \tag{6.2}$$

Where $Q_j(t)$ is the energy that is radiated away between time t and t+dt. Time, t, corresponds to a certain temperature T_r. For a given mass with known thermodynamic properties, the energy heat energy between two states can be described as:

$$\Delta E_{dt} = m_m \cdot c_p \cdot dT \tag{6.3}$$

This energy difference should be equal to the radiation heat. Therefore, the temperature difference is found by combining equations 6.2 and 6.3:

$$dT = \frac{\epsilon_r \cdot \sigma \cdot A_{r,j} \cdot (T_r^4(t) - T_{env}^4) \cdot dt}{m \cdot c_p} \tag{6.4}$$

$$T_{t+dt} = T_t - dT \tag{6.5}$$

For a given starting temperature at t_0 the next temperature at $t + dt$ can be found as seen in equation 6.5.

Depending on the desired operating temperature of a specified system, a different engineering approach should be taken. For rapid cooling at already low temperatures such as the cooling of hydrogen and oxygen prior to storage, a high emission coefficient and big surface area are required because of the drastic decrease due to the fourth power relation between the temperature and the radiation. The rate of cooling between 90 and 370 K rises a factor 300 and between 370 and 2250 K a factor 1350. Meaning the difference between rate of cooling of the system can vary by a factor 400000. Depending on the purpose of the process the substances should be protected against heat loss or designed such that rapid heat loss is possible for cooling purposes.

7

PROCESSES

7.1. EXCAVATION

There are several reasons why common excavation methods used on Earth cannot be employed on lunar regolith. Firstly, many excavation methods require water. Water is used in hydraulic excavation to break up soil or rock, power the hydraulic system, and operate the digging arm. In dredging, water is used to create a slurry of sediment and debris that is pumped to a disposal site. Trenching involves using water to soften soil, making it easier to dig and preventing the sides of the trench from collapsing. In drilling, water is used to cool the drill bit and flush out rock cuttings. Also, the low gravity on the Moon, which is only 1/6th of Earth's gravity, requires the mass of the excavator to be adjusted in order to compensate for the reduced gravitational pull. The excavator's normal force, which is the force that allows it to operate on the lunar surface, is much lower on the Moon. It has been estimated that a rover weighing 700 kg is needed to produce a pulling force of just 239 N, making the required mass investment and the associated financial costs impractical. Additionally, the lunar environment's atmospheric conditions, temperature fluctuations, and solar radiation levels make conventional terrestrial approaches unsuitable[35]. There are numerous applications for lunar regolith in manufacturing, construction, and propulsion. However, the main focus of this thesis is the propellant acquisition process, with only a brief discussion of the benefits of by-products such as iron, titanium, and silicon. When excavating lunar regolith, the forces acting on the excavator can be categorized into vertical and horizontal forces. This vertical force can be countered by the weight of the excavator whereas the horizontal tractive force acts on the wheels. The magnitude of this force is dependent on several factors, including the weight of the excavator, the number of wheels, the degree of effective wheel contact, as well as the angle of internal friction and cohesion of the lunar soil.

It is anticipated that very dense and firm regolith will be located beneath the initial 15 cm layer of lunar soil. Several excavators have been developed and tested, but many have failed during operation because they were unable to endure the hard rock. Therefore, methods for reducing excavation forces must be implemented to facilitate the extraction of the regolith [35]. Various techniques have been suggested to extract regolith, such as utilizing explosives or tearing the surface with sharp tools to loosen the top layer. Nonetheless, comprehensive information on the composition, density, particle size distribution, and shear strength is lacking and necessitates on-site data sampling for accurate characterization.

The lunar crust's hard subsurface rock is challenging to penetrate, and the mechanical implications of low gravity and temperature variations present significant obstacles for creating a low-cost, low-mass, dependable, and effective excavator.

There are various core designs within the active field of research on lunar excavation. One common method involves using a vibratory actuator with an excavation tool to loosen the soil with percussive force, followed by the tool collecting the regolith. Research has shown that this method can reduce the necessary excavation force by up to 93 % for typical regolith and up to 50 % for frozen regolith[16, 45]. Excavation rates were amplified by a factor of 2 to 6, in addition to a decrease in the necessary force. An alternative approach is the continuous excavating technique, which employs excavators such as bucket-wheel, bucket drum, bucket ladder, and screw conveyor excavators. This type of excavation method generates lower resistive forces and

achieves high excavation rates for the designated size. The bucket drum subclass appears to have the most potential as it only necessitates a rotating motion to excavate, store, and unload. Although these excavators offer many benefits, they have a significant drawback: they are subject to considerable wear and tear. To address this issue, some have attempted to reduce the number of moving parts by employing pneumatic methods, which can greatly decrease the amount of force required to operate the excavator. It is unclear how much wear and tear the percussive systems experience, but it is anticipated to be less severe than in the case of continuous excavation. It is worth noting that the percussive mechanism used to loosen the lunar soil requires more power than the bucket drum excavator, making it less appealing from an energy efficiency standpoint. Additionally, excavating the deeper layers of the lunar soil necessitates pre-treatment or the use of heavier equipment. Currently, it is believed that extracting regolith up to a depth of 30 cm is economically feasible, as deeper layers require either heavier machinery or the incorporation of explosives or another supplementary system to increase the mass.

Discrete excavators possess excavation rates that range from 100-900 $\frac{kg}{h}$, power requirements ranging from 100-200 W, and excavator masses ranging from 76 kg to 300 kg. The most efficient discrete excavator requires a relatively low amount of power, at 400 J per kg of excavated material. However, it should be noted that the test soil used was sand, which is not representative of lunar regolith, and that the scraper design may be less adaptable to the changing rocky surface of the Moon [3, 99].

Various designs of continuous excavators were tested, and they demonstrated an excavation capacity ranging from 6-2400 $\frac{kg}{h}$, with energy requirements varying from approximately 20-470 W [89].

Apart from the horizontal resistive force, it's important to also investigate maintenance needs caused by wear and tear, as well as measures to reduce dust production for optimal performance.

Due to the numerous gaps in our understanding of the composition of lunar soil and the varying surface conditions across different locations, evaluating appropriate excavation methods poses a challenge. Nonetheless, the high transportation costs make it imperative to use a lightweight excavator. The low gravity of the Moon and mass limitations create difficulties in generating the necessary force to collect regolith. One potential solution lies in exploring low-mass excavation systems in the continuous category. Both bucket drums and bucket wheels can generate enough force and excavation rate to justify their use for lunar excavation. However, bucket drums have an advantage over bucket wheels due to their fewer moving parts, making them more reliable in the uncertain lunar environment. Bucket wheels, on the other hand, are more vulnerable to lunar dust and require an additional system to transport extracted regolith [39]. While current excavation methods for lunar regolith are still in the research and development stage, NASA's RASSOR is a tested low-mass continuous option that is considered the most viable short-term solution for lunar excavation [39]. It is worth noting that pneumatic and vibration methods may become valuable in future lunar missions where excavation depths exceed 30 cm. These methods can help loosen harder rock, reducing the force required for excavation. However, the consumable nature of these systems, which requires gas for operation, is a disadvantage. To sustain their use, it would be necessary to produce gas on the Moon or bring it from Earth.

Considering that the propellants to be compared are hydrolox, and ALICE the need for excavation and processing of water, oxygen, and aluminum is required. Where hydrolox needs both the hydrogen and oxygen that can be extracted by mining water in craters and Permanently Shadowed regions (PSRs) such that the water can subsequently be electrolyzed. Noting that lunar regolith consists of $40-45$ % oxygen by weight [69], it can be mined for the extraction of the oxidizer. This would be suitable in the case that the hydrogen part of hydrolox and the methane part of methalox would be carried from Earth.

Currently, NASA is developing an excavator called the Regolith Advanced Surface Systems Operations Robot (RASSOR) Excavator. RASSOR has a Technological Readiness Level (TRL) of about 4 which is state-of-the-art in the developing field of lunar technology. Considering NASA is behind the project and one of the major players in the field of Aerospace engineering, the further development, and deployment of RASSOR is considered likely. Therefore, RASSOR will be used as the main excavator for regolith mining, to this end the specifications as can be seen in table 7.1 will be used for further calculations.

Power Source	Li-ion battery	
Battery Capacity	1410	Whr
Max Driving Slope	20	deg
Max Obstacle Height	75	cm
Regolith Delivered/Trip	90	kg
Max Speed	49	cm/s
Trips/Charge (100m)	20	Trips
Dry Mass	67	kg
Energy/Delivered Regolith	0.761	Whr/kg

Table 7.1: Specifications of RASSOR [66]

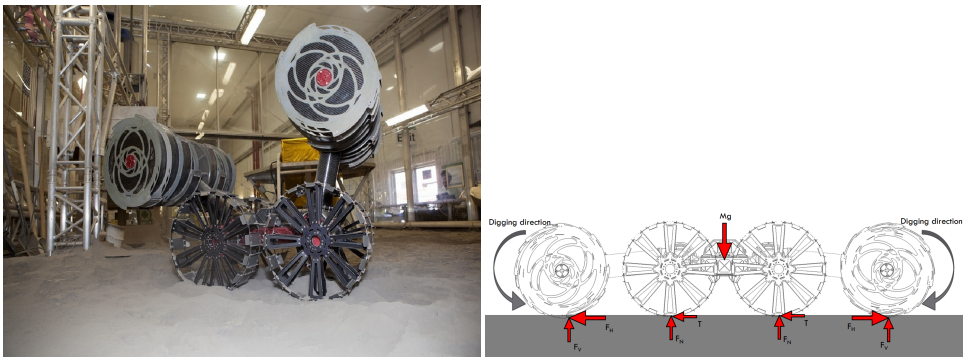

(a) RASSOR excavator [NASA]

(b) Acting Forces [90]

Figure 7.1: Regolith Advanced Surface Systems Operations Robot (RASSOR) Excavator

It can be seen in figure 7.1a that the bucket drums that are used to excavate the regolith are twofold and attached to the axes of the wheels such that they can move around these axes. This allows the excavator to alter its position relative to the ground by using the bucket drums as an extra set of wheels to and to of mass which helps to pass obstacles [66]. Since the precise conditions and local topology. In the low gravity environment of the Moon friction forces are lower, thus making it more difficult for low mass machinery to operate. To mitigate this problem the two bucket drums excavate in parallel while both rotating in opposite directions such that a net-zero reaction force remains as can be seen in 7.1b [90]. Excavators that are capable of on the spot processing of the regolith to extract the desired elements are not examined since the low mass, low cost and easy design of RASSOR allows for a scalable excavator system. The additional systems that should be incorporated on all the excavators to directly process the regolith makes the system more complex, high mass and expensive.

NASA's RASSOR excavator can be employed to collect the regolith which gives the following exergy expressions. This excavator was tested in icy simulant [39] and will be used for both regolith and icy regolith. The power required for the excavation operation can be found in table 7.1. Considering the composition, pressure, and temperature of the regolith remain constant, since the regolith is only transported, the exergy the system has before and after excavation is 0 because the regolith remains in the dead state. The exergy input and destruction however are related to the exergy input for the excavation itself and are given below.

$$Ex_{in} = -W = 2.74 \frac{kJ}{kg} \tag{7.1}$$

Where $-W$ is the exergy input of the excavator expressed per kg of excavated material.

$$Ex_{out} = 0 \tag{7.2}$$

The regolith is incapable of doing work after excavation since it is still in equilibrium with the environment, therefore $\dot{E}x_{out}$ is 0.

$$Ex_{d} = -W = 2.74 \frac{kJ}{kg} \tag{7.3}$$

The exergy destruction of the excavation process is equal to the work input of the excavator.

Ex_{in}	Ex_{out}	Ex_d
2.74 $\frac{kJ}{kg}$	0	2.74 $\frac{kJ}{kg}$

Table 7.2: Exergy input, output and destruction for excavation

7.2. PEM ELECTROLYZER

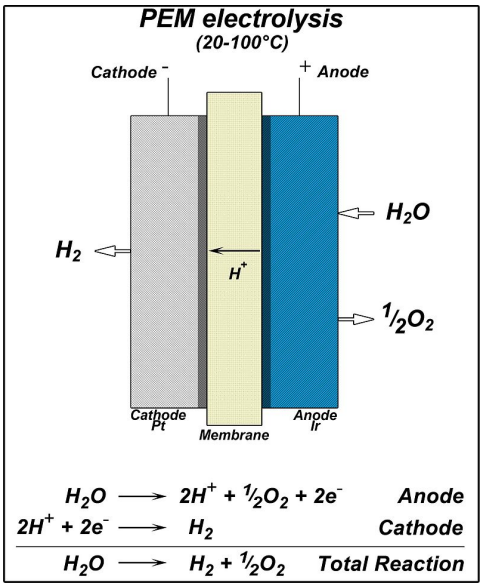

Figure 7.2: Proton exchange membrane electrolyzer

As can be seen in figure 7.2, a PEM (Proton Exchange Membrane) Electrolyzer separates the hydrogen and oxygen of the water. The figure consists of the fundamental principle where the hydrogen ions can move through the membrane due to the voltage that is being applied to the system. Also, the cathode and anode are displayed and are made out of platinum and iridium respectively [9]. Other materials have been proposed because the choice of the anode and cathode material plays a crucial role in the efficiency of the reactor. For the anode materials such as platinum or a platinum-ruthenium alloy [8], but different anode materials are being explored due to the high cost of platinum.

PEM electrolyzers have some adavantages:

- High efficiency: Typically around 70 % however some models have achieved efficiencies of up to 80 % [65].
- PEM electrolyzers have a rapid response time meaning they can start and stop quickly.
- Low Maintenance: Very few moving parts are needed for a PEM electrolyzer.
- Compact: PEM electrolyzers are relatively small compared to other electrolyzers.
- Low pressure: Water does not require to be pressurized to very high pressure, whereas alkaline electrolyzers sometimes operate at 30 bar. A PEM electrolyzer operates between 1 and 2 bar [65].

The efficiency in combination with the compact, low pressure, and low maintenance characteristics of the PEM electrolyzer make it a suitable option for lunar use. However, PEM electrolyzers are costly and depend on catalysts such as platinum, platinum alloys, palladium, and ruthenium [9, 59]. The durability of the ion exchange membrane is an obstacle since it degrades over time, this means that the membrane, which is made of Nafion [97], needs to be replaced after some time.

Before the electrolyzer can be used some steps regarding the pretreatment of the regolith needs to be done.

For the extraction of water, the regolith needs to be heated up to at least 220 K for the water to sublimate, note that the water phase diagram tells us that no liquid water is formed only gas. The sublimation rate of water at 220 K is relatively slow, therefore the regolith is heated to 360 K to increase the sublimation rate. After extraction, the water goes into the PEM electrolyzer which operates at 360 K. The heat input for the heating of the regolith and water can be described by:

$$Q_{in} = \int_{40\ K}^{360\ K} \eta_w \cdot c_{p,w}(T) + (1-\eta_w) \cdot c_{p,r}(T) dT + \eta_w \cdot L_{sub} \tag{7.4}$$

Where the first term describes the heat needed for the heating of water per kg of excavated material. The water concentration in the regolith, η_w, is 5.6 %. This is then multiplied by the integral of temperature-dependent heat capacity. The second term considers the pure regolith in the 1 kg of excavated material which has a concentration of 94.4 %. The last term is the latent heat, L_{sub} for the sublimation of water. Where $c_{p,r}(T)$ is described in appendix B, section 12.In the case of water, a temperature-independent heat capacity is taken for both the solid and gas phase, which are $c_{p,ice} = 1.6\ \frac{kJ}{kg}$ and $c_{p,vapor} = 2.1\ \frac{kJ}{kg}$, respectively. The heat of sublimation that is required for the ice-to-gas phase change is $L_w = 2837\ \frac{kJ}{kg}$. The exergy input can now be computed, such that:

$$Ex_{in} = Q \cdot \left(1 - \frac{T_e}{T_s}\right) \tag{7.5}$$

The total exergy input is only dependent on the heat flow considering no work is done by or to the system and the chemical and thermomechanical components are 0.

$$Ex_{out} = \eta_w \cdot \left((H_{w_{360,v}} - H_{w_0}) - T_0 (S_{w_{360,v}} - S_{w_0}) + Ex_{ch}^{H_2O} \right) \tag{7.6}$$

The regolith in the reactor is discarded and therefore is not considered a part of the exergy output of the system.

$$Ex_d = Q \cdot \left(1 - \frac{T_e}{T_s} \right) - \eta_w \cdot \left((H_{w_{360,l}} - H_{w_0}) - T_0 (S_{w_{360,l}} - S_{w_0}) + Ex_{ch}^{H_2O} \right) \tag{7.7}$$

where H_w, H_{w_0}, S_w, S_{w_0}, η_w and $Ex_{ch}^{H_2O}$ are the enthalpy of water at 360 K and at the ambient temperature, the entropy of water at 360 K and at the ambient temperature, the water yield per kg of regolith and the standard chemical exergy of water as given in table 5.4.

Ex_{in}	Ex_{out}	Ex_d
311 $\frac{kJ}{kg}$	167.4 $\frac{kJ}{kg}$	152.8 $\frac{kJ}{kg}$

Table 7.3: Exergy input, output and destruction for heating

The water vapor is now compressed to 2 bar before the water is going through the PEM electrolyzer. The required work done by the compressor can be expressed by:

$$W_{c,theoretical} = U_{w_{360,v}} - U_{w_{360,l}} + p_c \cdot \left(v_{w_{360,v}} - v_{w_{360,l}} \right) \tag{7.8}$$

The variables $U_{w_{360,v}}$, $U_{w_{360,l}}$, $v_{w_{360,v}}$, $v_{w_{360,l}}$ and p_c represent the internal energy and specific volume of the water vapor and liquid, as well as the pressure to which the vapor is compressed. The work required to be performed by compressors is not expected to reach the theoretical minimum due to various inefficiencies in the compression process. An efficiency, η_c of approximately 80% can be anticipated for typical compressor systems. The exergy equations then become:

$$Ex_{in} = \eta_w \cdot \left(-\frac{W_{c,theoretical}}{\eta_c} + \left((H_{w_{360,l}} - H_{w_0}) - T_0 (S_{w_{360,l}} - S_{w_0}) + Ex_{ch}^{H_2O} \right) \right) \tag{7.9}$$

The exergy input into the compressor consists of the work required for the compression and the thermomechanical and chemical exergy that is being carried by the water.

$$Ex_{out} = \eta_w \cdot \left((H_{w_{360,l}} - H_{w_0}) - T_0 (S_{w_{360,l}} - S_{w_0}) + Ex_{ch}^{H_2O} \right) \tag{7.10}$$

The remaining exergy is the sum of the thermomechanical and chemical exergy of the liquid water.

$$Ex_d = Ex_{in} - Ex_{out} \tag{7.11}$$

Ex_{in}	Ex_{out}	Ex_d
361.9 $\frac{kJ}{kg}$	54.6 $\frac{kJ}{kg}$	307.3 $\frac{kJ}{kg}$

Table 7.4: Exergy input, output and destruction for compression

This means that the required exergy input for the production of 1 kg of water at 2 bar from excavation to compression is 9240 $\frac{kJ}{kg}$.

In the context of a Proton Exchange Membrane electrolyzer, the enthalpy of formation of water must be overcome in order to carry out the electrolysis process. The enthalpy of formation is defined as the theoretical minimum energy input required to split a molecule into its constituent atoms, and is determined by the Gibbs free energy and entropy of the system.

$$\Delta H = \Delta G + T\Delta S \tag{7.12}$$

The irreversible losses $T\Delta S$ require heat input however, after the electrolysis has begun the process releases heat that greatly exceeds the the entropy term. The energy and exergy efficiency of the PEM electrolyzer is the same since they now both depend on the electrical energy input which is 100 % exergy and the potential chemical output of the hydrogen and oxygen. This means that the Gibbs free energy divided by the exergy efficiency as given by [65]. The exergy efficiency varies with operating temperature, current density and the anode exchange current density. For a typical electrolyzer, the exergy efficiency is in the range of 60 – 80 %. A conservative estimate of 65 % seems reasonable. Now a problem arises in terms of exergy interpretation, normally hydrogen is seen as the carrier of the energetic potential of the oxygen-hydrogen chemical reaction since the release of hydrogen into the environment causes it to react with the oxygen molecules in the atmosphere, however, the combination oxygen and hydrogen should be considered together as the carriers of the combustion potential, also it should be noted that if these molecules are now compared only to the environment, the combustion potential would be lost meaning that the exergy efficiency of the electrolyzer would be greatly underestimated.
At a pressure of 2 bar and a temperature of 360 K, the heat generated during electrolysis is believed to exceed the heat input related to entropy, and thus the entropy term can be neglected. As such, the work performed by the electrolyzer can be expressed using the Gibbs free energy[65].

$$W_{PEM} = -\frac{\Delta G_w}{\eta_{PEM}} \tag{7.13}$$

The Gibbs free energy of water, ΔG_w, at 360 K is given by JANAF and equals $-225.7\ \frac{\text{kJ}}{\text{mol}}$ or $-12539\ \frac{\text{kJ}}{\text{kg}_{\text{water}}}$. Therefore the exergy input becomes:

$$Ex_{in} = \eta_w \cdot \left(-W_{PEM} + \left((H_{w_{360,l}} - H_{w_0}) - T_0(S_{w_{360,l}} - S_{w_0}) + Ex_{ch}^{H_2O}\right)\right) \tag{7.14}$$

The exergy output consists first of the thermomechanical potential of the hydrogen and oxygen, secondly the chemical exergy of combustion and lastly, the standard chemical exergy of the water that would be formed. The amount of oxygen and hydrogen are given by their respective mass fraction in the water molecule, H_2O. The molar mass of a single hydrogen atom is, $1.01\frac{g}{mol}$ and the for an oxygen atom $16\ \frac{g}{mol}$, the mass fraction of hydrogen, δ_h, and oxygen, δ_o, in a water molecule is, therefore, 11.11 % and 88.88 %.

$$Ex_{out} = \eta_w \cdot \left(\delta_h\left((H_{h_{360}} - H_{h_0}) - T_0(S_{h_{360}} - S_{h_0})\right) + \delta_o\left((H_{o_{360}} - H_{o_0}) - T_0(S_{o_{360}} - S_{o_0})\right) - \Delta G_w + Ex_{ch}^{H_2O}\right) \tag{7.15}$$

$$Ex_d = Ex_{in} - Ex_{out} \tag{7.16}$$

Ex_{in}	Ex_{out}	Ex_d
$1223\ \frac{kJ}{kg}$	$752.8\ \frac{kJ}{kg}$	$470.4\ \frac{kJ}{kg}$

Table 7.5: Exergy input, output and destruction for water electrolysis

7.3. LIQUEFACTION

Considering the great decrease in density when hydrogen and oxygen change phases, it is compelling to liquefy it for mass reduction reasons related to the storage system. In order to liquefy the hydrogen it needs to be brought to a temperature below 20 K. This can be done by using a throttling process where a Joule–Thomson effect is used. This effect is the phenomenon where the temperature of a gas changes when it is allowed to rapidly expand when pushed through a throttling valve or a porous plug where the enthalpy remains, it is an isenthalpic, entropic process. When a gas undergoes a throttling process, it expands and the temperature and pressure drop according to the ideal gas law. However non-ideal gasses can exhibit temperature changes where the ideal gas law does not hold and a decrease in pressure results in a temperature increase. The Joule-Thomson effect that states that a real gas or liquid changes temperature when forced through a valve, which is dependent upon the initial temperature, this temperature ought to be below a certain temperature for a given substance, known as the inversion temperature. Below the inversion temperature, the substance decreases in temperature when forced through the valve, however above this temperature, it increases. For hydrogen, this inversion temperature is below 200 K [26].

There is a variety of methods that can be applied to liquefy hydrogen [6]:

- Joule-Thomson Expansion: This is the most used process for the commercial liquefaction of hydrogen. The process uses high-pressure hydrogen gas that is passed through a throttling valve after nitrogen pre-cooling to achieve the critical temperature.
- Claude Process: This process uses high-pressure hydrogen gas and a series of turbines, compressors, and heat exchangers and then uses a J-T valve to liquefy the hydrogen where the cold gaseous part of the hydrogen after throttling is again pumped through the system.
- Linde-Hampson: Similar to the Claude cycle but requires less equipment and the cycle uses a multi-stage refrigeration process involving compression, cooling, and expansion.
- Magnetic Refrigeration: This relatively new technology uses a magnetic field to cool the hydrogen gas. During this process, the gas is passed through a magnetic field.

The methods described above have advantages and disadvantages, magnetic refrigeration is a highly efficient process that is environmentally friendly and produces no heat or vibrations. It has a low maintenance and compact size, it is, however, a method that is relatively new and has not yet proved itself so will not be employed. The other methods are based on the same principle but vary in terms of the number of compressors, heat exchangers, expanders, and valves. The low temperature of the lunar environment allows for the passive cooling of hydrogen far below the inversion temperature which means that no active nitrogen or helium pre-cooling is required for the use of the Joule-Thomson effect. Therefore only a single compressor, heat exchanger, and JT-valve are sufficient to generate the desired hydrogen. This cycle is selected and depicted in 7.4 and will be used for the exergy calculation of the liquefaction of the hydrogen. Hydrogen cooling has an additional problem that ought to be looked at. Hydrogen can exist in two quantum states as seen in figure 7.3b, which are defined as orthohydrogen and parahydrogen. The natural fraction of the two is a function of temperature and has an asymptote for orthohydrogen and parahydrogen of 75% and 25%, respectively. It can be seen in fig. 7.3a that parahydrogen is the preferred state of hydrogen below 80 K. Considering hydrogen is stored at 20 K the required fraction of parahydrogen for storage is 99.8 % [108]. To achieve a rapid conversion of the hydrogen, such that it does not happen during storage where the orthohydrogen will flip its spin to form parahydrogen and thereby release heat, a catalyst, such as ironoxide and chromium oxide, should be added during the liquefaction process [17, 57]. This does require more work and thus energy but it is necessary to prevent boil-off [108]. An advantage of the liquefaction of hydrogen in the lunar environment is that the hydrogen starts at 40 K meaning the natural fraction of orthohydrogen is just 10 % as compared to 75 % on Earth. This is a considerable difference in conversion energy since the latent heat related to the ortho-para conversion is 525 kJ per kilogram of ortho-hydrogen[42].

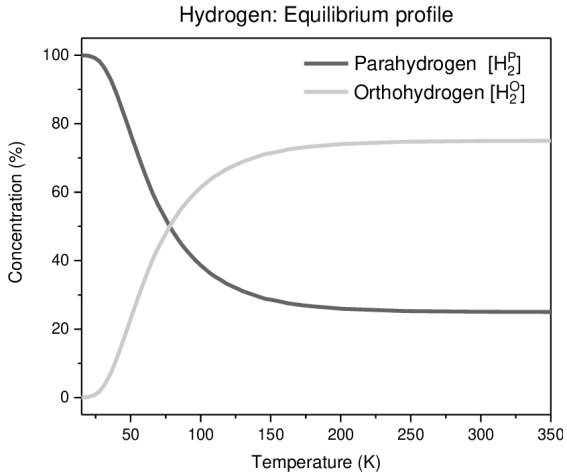

(a) naturally occurring ortho- and parahydrogen concentrations at different temperatures.[42]

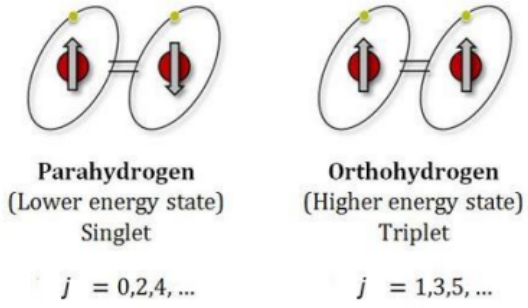

(b) Parahydrogen and Orthohydrogen nuclear spin isomers of the hydrogen molecule. Parahydrogen occupies even rotational energy levels and orthohydrogen occupies odd rotational energy levels [42]

Figure 7.3: Para-to-ortho conversion of hydrogen

The cycle operates in the following manner hydrogen gas is compressed then it is transferred through a heat exchanger lowering the temperature further, the highly compressed hydrogen is then pushed through a JV-

throttling valve where the temperature will rapidly decrease to produce partly liquid and partly gaseous hydrogen, the liquid will be transported away and the gas will go through the heat exchanger and will be added to the hydrogen supply as can be seen in fig. 7.4.

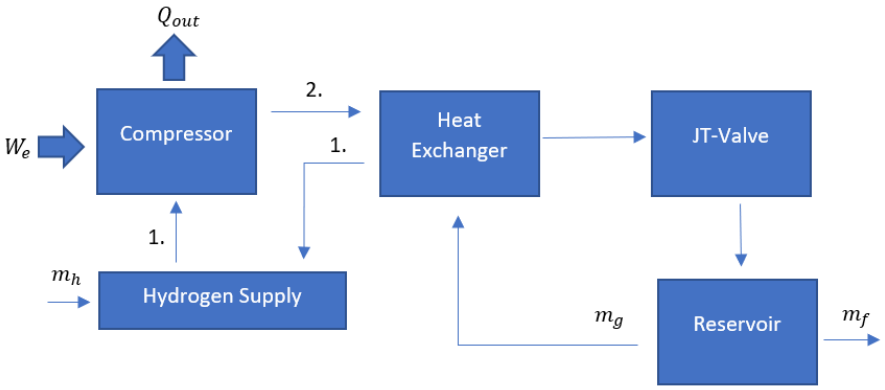

Figure 7.4: Linde-Hampson liquefaction cycle

A Linde-Hampson cycle operating in steady-state follows, where $m_f = m_h$ and the enthalpy of the hydrogen after the heat exchanger is equal to that of the hydrogen supply:

$$W_e - Q_{out} + (h_1 - h_2) = 0 \tag{7.17}$$

The equation states that the difference in enthalpy of the hydrogen before, 1, and after, 2, the compressor is equal to the difference of work for compression and the heat loss during the isothermal compression. The heat of entropy related to this compression is given by:

$$Q = T_1 \cdot (s_1 - s_2) \tag{7.18}$$

The entropy values for states 1 and 2 are now added to get an expression for Q_{out}. The energy related to the compression is then:

$$W_e = T_1 \cdot (s_1 - s_2) - (h_1 - h_2) \tag{7.19}$$

Where T_1 is the temperature at which the isothermal compression is done, in the case of the lunar architecture this is equal to the ambient temperature.

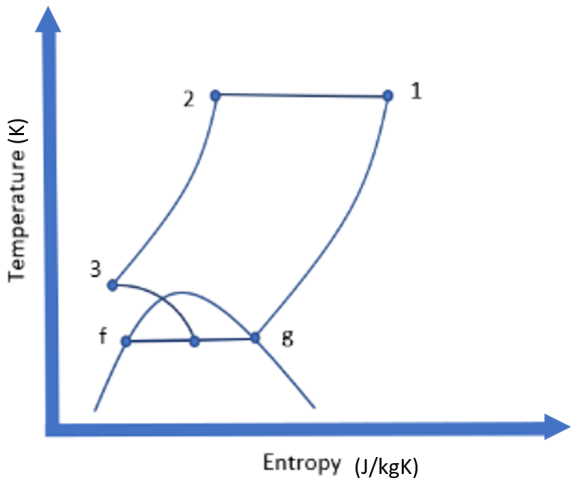

Figure 7.5: T-s diagram of the Linde-Hampson process

Fig. 7.5 shows the Linde-Hampson process:

- 1-2: First, isothermal compression of the hydrogen gas lowers the entropy by increasing the pressure at constant temperature.
- 2-3: Secondly, The isobaric heat exchange with the cold hydrogen gas lowers the temperature before it goes through the J-V throttling valve.
- 3-f/g: The isenthalpic throttling of the hydrogen gas, increases the entropy and lowers the temperature. The hydrogen is partly liquefied and partly remains in the gas phase.
- g-1: The isobar shows the hydrogen gas goes through the heat exchanger, lowering the temperature of the compressed gas coming out of the isothermal compressor.

The yield related to the cycle working in steady-state depends on the enthalpy of the liquid after throttling.

$$Y = \frac{h_1 - h_2}{h_1 - h_f} \tag{7.20}$$

Where Y and h_f are the yield after throttling and the enthalpy of liquid hydrogen. Therefore the work needed per kg of hydrogen is found by combining eq. 7.19 and eq. 7.20:

$$W_{LH_2} = (T_1 \cdot (s_1 - s_2) - (h_1 - h_2)) \cdot \frac{h_1 - h_2}{h_1 - h_f} \tag{7.21}$$

However, some adjustments to this estimate are required considering the liquefied hydrogen reaches a temperature where the para-ortho conversion of the hydrogen atoms spin results in an exothermal reaction heating the neighboring hydrogen such that it will evaporate again. The equation 7.21 does not take into account the heat that is released during the spin conversion of the remaining 10 % naturally present orthohydrogen at 40 K. For every 1 kg of hydrogen, this conversion results in 51.5 $\frac{\text{kJ}}{\text{kg}}$, assuming a comparable efficiency as for the cycle where the spin is not considered, the total work required for the liquefaction to 20 K hydrogen can be estimated.

The cooling, liquefaction, and storage exergetic costs depend on hydrogen and oxygen respectively. For the liquefaction and cooling of hydrogen, hydrogen is first cooled down to a temperature of 40 K and subsequently liquefied using a J-V throttling process. During the initial cooldown, catalysts, such as iron-oxide or chromium silica, are added to increase the rate of ortho-to-parahydrogen conversion to reduce the required work needed for the liquefaction process because of the exothermic nature of the conversion. This means that the cooling down of oxygen to 96 K, at which it liquefies, and cooling down water to 40 K, the ambient temperature, is first done passively. Subsequently, the oxygen is stored in a big tank that has a large volume-to-surface area ratio and thus a large mass-to-surface area ratio. The work required for the liquefaction of hydrogen from 40 K to 16 K is explained in section 7.3 with values that can be found in Appendix C. Where the pressure of the hydrogen after liquefaction is 2 bar and after compression 30 bar. The resulting work required for the liquefaction of 1 kg of hydrogen taking into account the ortho-para conversion using a Joule-Thompson valve is $W_{JT} = 2202.2\ \frac{\text{kJ}}{\text{kg}_{(\text{H}_2)}}$.

$$Ex_{in} = \eta_w \cdot \left(\delta_h \left(-W_{JT} + (H_{h_{360}} - H_{h_0}) - T_0(S_{h_{360}} - S_{h_0})\right) + \delta_o \left((H_{o_{360}} - H_{o_0}) - T_0(S_{o_{360}} - S_{o_0})\right) - \Delta G_w + Ex_{ch}^{H_2O}\right) \tag{7.22}$$

The exergy that goes into the system is the sum of the thermomechanical exergy potentials of both oxygen and hydrogen at 360 K and the corresponding combustion potential and chemical potential.

$$Ex_{out} = \eta_w \cdot \left(\delta_h \left((H_{h_{20}} - H_{h_0}) - T_0(S_{h_{20}} - S_{h_0})\right) + \delta_o \left((H_{o_{90}} - H_{o_{40}}) - T_0(S_{o_{90}} - S_{o_0})\right) - \Delta G_w + Ex_{ch}^{H_2O}\right) \tag{7.23}$$

After the liquefaction, the storage of hydrogen and oxygen is also taken into account as the hydrogen and oxygen are placed into storage tanks at 15 and 96 K. The enthalpy change due to radiation heating and cooling for hydrogen and oxygen respectively over the storage period is taken into account as the values for 20 K and 90 K are used in the equation above. This enthalpy difference for hydrogen between 15-20 K and for oxygen between 90-96 K should be enough to prevent the hydrogen from evaporating and thus increasing the pressure in the storage tank and the oxygen from getting too cold which would reduce the energy that can be used during combustion.

$$Ex_d = Ex_{in} - Ex_{out} \tag{7.24}$$

Ex_{in}	Ex_{out}	Ex_d
855.1 $\frac{kJ}{kg}$	808.5 $\frac{kJ}{kg}$	46.66 $\frac{kJ}{kg}$

Table 7.6: Exergy input, output and destruction for oxygen and hydrogen liquefaction and storage

7.4. STORAGE

Let us now consider the case where hydrogen and oxygen are stored. The energy difference is related to the enthalpy difference between two states and is given by:

$$E_{\Delta H,j} = m_{p,j} \cdot \Delta H_j \tag{7.25}$$

Where j denotes the type of propellant, and ΔH_j the enthalpy difference between two specified states of the given propellant.

Absorption and emissivity are important factors to consider when looking at the net radiation of a body. The power emitted by the body per unit area is equal to:

$$P_e = \epsilon_b \cdot \sigma \cdot T_b^4 \tag{7.26}$$

Where ϵ_b and T_b are the emission coefficient and temperature of the body. The power absorbed is a fraction of the radiation emitted to the body and is given by:

$$P_a = \alpha_b \cdot \epsilon_{env} \cdot \sigma \cdot T_{env}^4 \tag{7.27}$$

Where α_b is the absorption coefficient of the body and ϵ_b and T_{env} are the emission coefficient and temperature of the environment.

Since we are only considering the radiation as a factor for either cooling or heating the upper bound for the heat transfer is given by:

$$Q_{ox}(t_{storage}) = \left(\epsilon_b \cdot \sigma \cdot T_{b,ox}^4 - \alpha_b \cdot \epsilon_{env} \cdot \sigma \cdot T_{env}^4\right) \cdot A_{r,ox} \cdot t_{storage} = q_{ox} \cdot A_{r,ox} \cdot t_{storage} \tag{7.28}$$

$$Q_{ox}(t_{storage}) = \left(\epsilon_b \cdot \sigma \cdot T_{b,h}^4 - \alpha_b \cdot \epsilon_{env} \cdot \sigma \cdot T_{env}^4\right) \cdot A_{r,h} \cdot t_{storage} = q_h \cdot A_{r,h} \cdot t_{storage} \tag{7.29}$$

Where T_{min}, T_{max} are the lowest temperature of hydrogen, the highest temperature of oxygen. The following can be said:

$$E_{max} = Q_j(t_{storage}) \tag{7.30}$$

The upper bound of the energy that can be added or absorbed to or by the system through radiation is a function of the highest temperature difference with the environment and the duration, $t_{storage}$, of storage. For the very small temperature difference, the difference in radiation heating or cooling between the highest and lowest temperature under consideration are given by:

$$\nu = \frac{(T_{max}^4 - T_{env}^4)}{(T_{min}^4 - T_{env}^4)} \tag{7.31}$$

In the case of hydrogen and oxygen operating within the temperature ranges 16 to 19 K and 94 to 97 K. The values for ν are 1.02 and 1.10 this means that the rate at which the hydrogen is warmed up is too high and the rate at which the oxygen is cooled down is also too high. However, in the case of oxygen, the estimation has a bigger error due to the 10 % difference. The minimum amount of time it takes to heat or cool the mass is therefore given by:

$$t_{storage} = \frac{E_{\Delta H,j}}{q_j} \tag{7.32}$$

Note that $Q_j(t_{storage})$ is also a function of the tank surface area, for a spherical tank the following can be said:

$$A_{r,j} = 4 \cdot \pi \left(\frac{3m_{p,j}}{4\pi\rho_j}\right)^{\frac{2}{3}} \tag{7.33}$$

Therefore the temperature gradient for a given time step can be calculated as:

$$t_{storage} = \frac{m_{p,ox} \cdot \Delta H_{ox}}{q_{ox} \cdot \left(\frac{3m_{p,ox}}{4\pi\rho_{ox}}\right)^{\frac{2}{3}}} \tag{7.34}$$

$$t_{storage} = \frac{m_{p,h} \cdot \Delta H_{h}}{q_{h} \cdot \left(\frac{3m_{p,h}}{4\pi\rho_{h}}\right)^{\frac{2}{3}}} \tag{7.35}$$

	α_r/ϵ_r	mass (kg)	ρ $\frac{kg}{m^3}$	T_{start}	T_{end}	R (m)	ΔH $\frac{kJ}{kg}$	$t_{storage}$ (years)
Oxygen	0.005 / 0.0131	875000	1140	97	94	5.68	5.14	5.64
Hydrogen	0.005 / 0.0131	125000	71	16	19	7.49	24.9	1440

	α_r/ϵ_r	mass (kg)	ρ $\frac{kg}{m^3}$	T_{start}	T_{end}	R (m)	ΔH $\frac{kJ}{kg}$	$t_{storage}$ (years)
Oxygen	0 / 1	875000	1140	97	94	5.68	5.14	0.073
Hydrogen	1 / 0	125000	71	16	19	7.49	24.9	6.7

Table 7.7: Storage of the elements of water in lunar PSRs based on 1 million kg of electrolyzed water; top table is based on the use of MLI; the bottom table is based on maximum absorption and maximum emission

The radiation heating that occurs due to the temperature difference heats up or cools down the respective propellant. As seen in table 7.7, The large difference in storage time between oxygen and hydrogen can be explained by the much higher radiation heat flow between the two systems due to the fourth power in the radiation equation. Also, the enthalpy difference between the two states is much higher for hydrogen the very limited radiation heat that flows to the hydrogen and the very high enthalpy difference that needs to be overcome to increase its temperature means that a liquid hydrogen tank does not require any MLI to be able to store the hydrogen long-term in the PSRs. A storage system capable of storing oxygen for half a year without the temperature dropping below 94 K requires an emission coefficient in the order of 0.15 which can be achieved by choosing a coating with that property. The saving in cost for the massive insulation equipment. Note that the wall temperature for oxygen is overestimated since the thermal conductivity through the shell wall has not been included, for hydrogen, it is somewhat higher. Also, the conduction from the mechanism that stabilizes and connects the tank to the ground has not been considered. The main advantage is the large mass-to-radiation area ratio and the low temperature making radiation a slow means of heat transport.

7.5. MRE REACTOR

A molten regolith electrolyzer reactor is a device designed to extract oxygen and metals through the electrolysis of the lunar soil. The regolith is first heated such that it melts, the electrons can now move and the same basic principle of electrolysis of a solution can be applied. The metal and oxygen ions cluster together at the cathode and anode respectively which creates pure metal and oxygen. The oxygen that is formed is a gas that can be separated out. The solution consists of multiple metals, however, these metals have different voltages at which electrolysis occurs. Therefore the metals are electrolyzed in a subsequent manner starting with the lowest voltage. The reason for this approach is to prevent the formation of alloys at the cathode, considering pure metals are more useful in many applications since they are customizable.

	Ti	Al	Si	Fe
Highlands	<1	13.3	21.0	4.8
High-Ti Mare	5.1	6.6	19.2	12.9

Table 7.8: Weight percentage of metals in regolith

The maximum yield for metals if all of the oxides are perfectly electrolyzed is given in table 7.8. Highlands regolith has very low concentrations of titanium present in the minerals and is therefore not suitable for the extraction of titanium, however High-Ti mare regolith is suitable but not present in the south pole environment. For other applications where titanium is needed another processing site should be chosen.

In 2015, Schreiner [87] has optimized an MRE reactor where the leading design parameter was the temperature such that the reactor would not melt. The energy consuming processes related to the regolith reactor are the regolith heating, the endothermic heat required during electrolysis and the electrolysis itself given by equations 1, 2 and 3, respectively.

1. $\dot{Q}_{regolith-heating} = \dot{m}_{reg}\left(\int_{40K}^{T_{op}} C_p(T)dT + L\right)$
2. $\dot{Q}_{endothermic} = \dot{n}_{O_2} \cdot avg[\Delta H - \Delta G] = \dot{n}_{O_2} \sum_i \Delta H_i(T) - \Delta G_i(T)\left(\frac{c_i(T)}{C}\right)$
3. $P_{\Delta G} = \dot{n}_{O_2} avg[\Delta G]$

Where $\dot{m}_{reg}$ is the mass of the regolith, $\dot{n}_{O_2}$ is the molar flow rate of the produced oxygen. T_{op} is the operating temperature and C_p is the heat capacity. The endothermic heat is described by $\dot{Q}_{endothermic}$ and is based on the entropy term that is calculated by looking at the average of the difference between the enthalpy and Gibbs free energy. For each oxide, these values are looked up in JANAF for the given operating temperature. For the estimation of the heat flow, the coulomb concentration of each species in the regolith is looked at, where c_i is the number of coulombs needed for the species i and C is the total number of coulombs per batch.

Products	O_2	Si	Fe	Al	Ti	Waste
Highlands	43.3	19.5	4.32	8.66	0	24.2
Mare	41.7	16.7	12.5	4.17	5.42	19.6

Table 7.9: Production results of reactor operating at 2300 K for the extraction of metals and oxygen for High-Ti Mare and Highlands regolith[87]

The expected yield of each element is depicted in table 7.9 as calculated by Schreiner. The energy input per kg of regolith for a reactor that is operating at 2250 K, was given and is 19000, 54000, and 34000 $\frac{kJ}{kg}$ for regolith heating, the endothermic reaction and the electrolysis, respectively. Lower temperatures are also feasible considering regolith melts at lower temperatures however the electrolysis of aluminum is not possible at these temperatures.

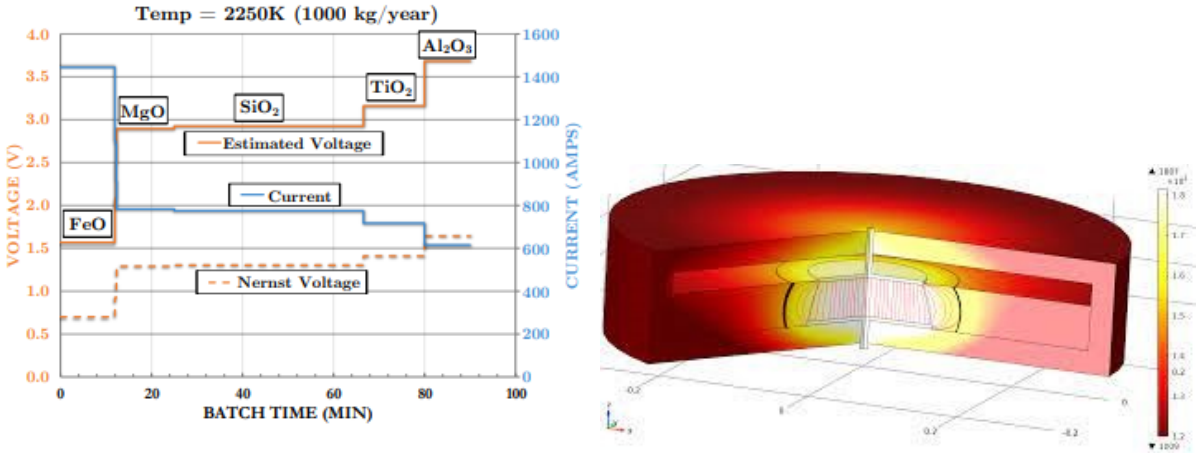

(a) Current and Voltage for the reduction of oxides at 2250 K [88]

(b) MRE reactor [88]

Figure 7.6: MRE reactor: voltage and temperature distribution

To prevent the mixing of the metals, the current and voltage are considered for each oxide as seen in fig. 7.6a. First iron oxide is reduced, then magnesium, which is will not be considered but does pose some challenges since it is being electrolyzed along with the silicon oxide. Then titanium is reduced and finally the aluminum that is required for the ALICE grain.

The reactor depicted in fig. 7.6b shows that the core of the reactor is very hot, this is where the liquid regolith is present. The neighboring regolith functions as a heat shield that gradually decreases in temperature thereby maintaining the structural integrity of the reactor.

MRE	Si	Al	Fe	O_2
Yield	18.8	9.1	4.6	41.7

Table 7.10: Yield of metals and oxygen as a percentage of regolith mass

The ALICE grain also requires oxygen to be added to the aluminum particle to create a small layer of oxide to prevent spontaneous combustion of the ALICE grain as described in section 7.7. This results in the corrected yield as given in table 7.11.

	Al	Al_2O_3	O_2
Yield	8.09	2.02	40.6

Table 7.11: Yield of aluminum and oxygen after aluminum powder manufacturing as a percentage of regolith mass

The incoming regolith for the MRE reactor is in the dead state when to the MRE reactor since it has only been excavated and transported.

$$Ex_{in} = \left(1 - \frac{T_0}{T_{MRE}}\right) Q_{MRE} - W_{MRE} \tag{7.36}$$

The required exergy that needs to be put into the system to get the desired products is equal to the exergy of heat and work that is put into the system for the electrolysis.

$$\begin{aligned} Ex_{out} = {} & \eta_{al} \cdot \left((H_{al_{2250}} - H_{al_0}) - T_0 \cdot (S_{al_{2250}} - S_{al_0})\right) \\ & + \eta_{si} \cdot \left((H_{Si_{2250,g}} - H_{Si_0}) - T_0 \cdot (S_{Si_{2250,g}} - S_{Si_0})\right) \\ & + \eta_{Fe} \cdot \left((H_{Fe_{2250,g}} - H_{Fe_0}) - T_0 \cdot (S_{Fe_{2250,g}} - S_{Fe_0})\right) \\ & + \eta_{O_2} \cdot \left((H_{o_{2250,g}} - H_{o_0}) - T_0 \cdot (S_{o_{2250,g}} - S_{o_0})\right) \\ & + \eta_{Al_2O_3} \cdot (-\Delta G_{Al_2O_3} + Ex_{ch}^{AL_2O_3}) + \eta_{SiO_2} \cdot (-\Delta G_{SiO_2} + Ex_{ch}^{SiO_2}) + \eta_{FeO} \cdot (-\Delta G_{FeO} + Ex_{ch}^{FeO}) \end{aligned}$$

The remaining exergy is equal to the sum of the thermomechanical and chemical components of the products of the electrolysis.

$$Ex_d = Ex_{in} - Ex_{out} \tag{7.37}$$

Ex_{in}	Ex_{out}	Ex_d
90698 $\frac{kJ}{kg}$	10499 $\frac{kJ}{kg}$	80199 $\frac{kJ}{kg}$

Table 7.12: Exergy input, output and destruction of the MRE reactor

7.6. YSZ SEPARATOR

A YSZ separator is a ceramic material that is used as a solid-state electrolyte in high-temperature electrochemical devices such as solid oxide fuel cells, SOFCs, and solid oxide electrolysis cells, SOECs, [67, 105]. The material of the separator is a combination of zirconia, ZrO_2 and yttria, Y_2O_3, that stabilizes the crystal structure of zirconia and promotes the formation of oxygen vacancies.

One important property that is considered when dealing with high-temperature environments is the resistance to thermal shock, which allows for rapid heating and cooling cycles, which is to be expected in the lunar environment.

Furthermore, YSZ separators can be formed such that they consist of thin and dense films, this improves the performance of the ion transport [36]. Overall, the YSZ separator is a very useful component of high-temperature electrochemical devices. The high ionic conductivity, mechanical strength, and chemical stability make it an interesting material for the use in the lunar architecture [110].

In order to estimate the exergy flow through the YSZ separator, the electrical work required for the separation should be calculated.

This is done by estimating the resistance electrical power equation using the equation:

$$P = I^2 \cdot R_{YSZ} \tag{7.38}$$

Where P, I, and R_{YSZ} are the power, current, and resistance, respectively. Expressions for the current and resistance are also needed. First, the current can be estimated using Faraday's law, which is given by:

$$I = \dot{n}_{O_2} \cdot z \cdot F \tag{7.39}$$

Where $\dot{n}_{O_2}$, z and F are the molar flow rate of oxygen through the separator, the number of electrons per diatomic oxygen molecule, and the Faraday constant, which is equal to 96485.33 $\frac{\text{sA}}{\text{mol}}$. The resistance of the YSZ separator is proportional to the thickness, and an inverse function of the electrical conductivity, $\sigma_e(T)$, and cross-sectional area, S.

$$R_{YSZ} = \frac{\Delta YSZ}{\sigma_e(T)S} \tag{7.40}$$

The electrical conductivity (in $\frac{S}{cm}$) of the separator is a function of temperature[102]:

$$\sigma_e = e^{A \cdot e^{B \cdot T}} \tag{7.41}$$

Where A and B are constants with values -23.4 and -0.00259, respectively. The value for S is given by, [32]:

$$S = \frac{I}{j} \tag{7.42}$$

Where j is the current density. Selecting reasonable values for the thickness, ΔYSZ, the current density, j, and operating temperature T_{YSZ}, the power demand for the separator can be estimated.

$$Ex_{in} = \eta_{ox}\left(-W_{YSZ} + \left((H_{O_{2250,g}} - H_{O_0}) - T_0 \cdot (H_{O_{2250,g}} - S_{O_0})\right)\right) \tag{7.43}$$

$$Ex_{out} = \eta_{ox} \cdot \left((H_{O_{1600,g}} - H_{O_0}) - T_0 \cdot (H_{O_{1600,g}} - S_{O_0})\right) \tag{7.44}$$

The exergy output consists of the thermomechanical exergy of the gaseous oxygen.

$$Ex_d = Ex_{in} - Ex_{out} \tag{7.45}$$

Ex_{in}	Ex_{out}	Ex_d
1601 $\frac{\text{kJ}}{\text{kg}}$	667 $\frac{\text{kJ}}{\text{kg}}$	933 $\frac{\text{kJ}}{\text{kg}}$

Table 7.13: Exergy input, output and destruction YSZ separator

7.7. ALUMINUM POWDER MANUFACTURING

There are multiple methods for the manufacturing of aluminum powder, the reasons for the selection of a specific method for lunar implementation are the amount of energy consumption, the infrastructure needed and the expandable materials that are being depleted during the manufacturing process. Another major factor that affect the selection process is the grain size and grain size distribution of the respective method. For ALICE [81] rocket propellant a grain size of 80 nm is required for reasons that will be elaborated on, also the distribution is of interest to predict combustion behavior.

- Mechanical ball milling: Mechanical ball milling is a common technique used to produce fine powders in various industries, including metallurgy, chemical engineering, and materials science. The process involves placing a mixture of powders into a milling chamber, which is then rotated at high speeds, causing the balls inside to impact and grind the powders, resulting in a fine powder.
  To begin the process of mechanical ball milling, the powders are usually mixed in a predetermined ratio and placed in the milling chamber along with the milling balls. The milling chamber can be sealed to prevent contamination from the outside environment, and the milling can be carried out under various conditions, such as in air, under inert gas, or in a liquid medium.
  The milling time can range from a few minutes to several hours, depending on the desired particle size and the properties of the powders. After milling, the powders are typically removed from the milling chamber and can be further processed, such as by annealing or sintering, to produce a final product with the desired properties.

- Mechanochemical synthesis: Mechanochemical synthesis makes use of the ball milling method. However, a solid-state displacement reaction is introduced resulting in very fine powder down to 5 nm [29].

- Exploding wire: The exploding wire technique is a method of producing aluminum powders that involves the use of high-voltage electricity to vaporize a thin wire made of aluminum. The vaporized aluminum is then rapidly cooled, resulting in the formation of fine aluminum powder.

  The process of exploding wire begins by attaching a thin wire made of aluminum to two electrodes. When a high-voltage electrical discharge is passed through the wire, it rapidly heats up and vaporizes the aluminum, forming a plume of aluminum vapor. The vapor cools rapidly as it expands, condensing into fine particles of aluminum powder.

  The size and morphology of the aluminum powder produced by the exploding wire technique can be controlled by varying the voltage and current used, as well as the diameter of the wire. The process can also be carried out in a controlled atmosphere, such as under inert gas, to prevent oxidation of the aluminum powder [29] [103]. Expected particle sizes are in the range 20-100 nm and require about 25 $\frac{\text{kWh}}{\text{kg}}$ [46].

- Solution reduction: Solution reduction is a chemical process used for the reduction of metal ions in a solution, where a reducing agent is employed to reduce Al+3 ions in solution. This method is simple, not time-consuming, and has the potential to be scaled up for mass manufacturing needs. One example of this process involves treating aluminum chloride with lithium aluminum hydride in mesitylene at 164°C to produce aluminum nanoparticles. However, this method is inconvenient for scale-up and nanoparticles produced using this method may still contain measurable levels of carbon, oxygen, and chlorine.

  Benzildiethylenetriamine was successfully used as a reducing agent in various solvents such as methanol, ethanol, water, acetonitrile, cyclohexane, and dimethylsulphoxide to synthesize aluminum nanoparticles in the range of 4-13 nm [68]. Additionally, aluminum nanoparticles with sizes ranging from 5-8 nm have been synthesized using NaBH4 or LiAlH4 as reducing agents. Bimetallic Al/Au nanoparticles have also been synthesized in a water solution using Al+3 and Au+3 metal salts and reducing solutions containing sodium citrate, tannic acid, and sodium carbonate.

  In 2012, a study investigated the synthesis of aluminum nanoparticles in a polypropylene (PP) matrix by a sol-gel process in the melt, demonstrating that it is possible to produce inorganic nanoparticles in a polymeric matrix without solvents. Generally, chemical reduction methods employ reducing agents such as benzildiethylenetriamine or lithium aluminum hydride in a chemical solution.

- Gas-phase synthesis: The most common method for synthesizing aluminum nanoparticles involves evaporating aluminum from a molten state into a chamber filled with an inert gas, where the gaseous metal condenses. However, the purity of the starting material and the type and purity of the inert gas atmosphere used can strongly affect the properties of the resulting aluminum nanoparticles. Cryomelting, a modified inert gas evaporation method, can also be used to produce aluminum nanoparticles by rapidly condensing the evaporated metal in a region cooled to about 70 K. This method can produce nanoparticles ranging from 20 to 500 nm in size, with 60% of the particles smaller than 70 nm.

  In other research, the thermal behavior of aluminum nanoparticles prepared using the inert gas con-

densation process was investigated, while Fernández et al. used this method to produce aluminum nanoparticles with a diameter of 23 nm, which were found to be covered by an alumina overlayer of approximately 4 nm.

A novel electromagnetic levitational gas condensation (ELGC) system was designed and manufactured for synthesizing aluminum nanoparticles. The optimal argon flow rate for producing aluminum nanoparticles was found to be between 10-15 L/min [44].

- Liquid-phase synthesis: Laser ablation is a method capable of manufacturing aluminum nanoparticles with a narrow size distribution. Liquid-phase laser ablation is a three-step process. First, the laser beam heats up the surface of interest to create a plasma plume with vapor particles, then the plasma plume expands adiabatically and finally, the particles condense. Laser ablation material was placed into ethanol, acetone, and ethylene glycol to create particles of 30 nm with a distribution between 10 and 100 nm [7].
- Laser ablation: The pulsed laser ablation (PLA) method is known for its ability to produce nanoparticles with a narrow size distribution. This process can be divided into two stages: evaporation of the target material and hydrodynamic expansion of the ablated plume into the ambient gas. Nanoparticle formation involves two critical stages: homogeneous nucleation and particle growth, where supersaturated vapor atoms produced by laser ablation form critical nuclei that capture atoms on their surfaces and transition into large particles.

  Synthesized aluminum nanoparticles can be manufactured using the laser ablation method in argon gas as the ambient gas. They discovered that controlling the ambient gas temperature enables control over the particle size. In addition, introducing ethylene to the argon quench flow allows for the coating of aluminum nanoparticles generated by laser ablation with carbon, resulting in an average mobility diameter of 80 nm.

  The nanoparticle generation process was investigated during nanosecond and picosecond laser ablation of various metals (Ni, Al, W, and stainless steel) in ambient air and argon gas. It was found that the size distribution and number concentration of generated metal particles during laser ablation in ambient air differed from those in argon gas medium. The number concentrations of generated nanoparticles during laser ablation in argon gas were up to 100 times higher than those produced in ambient air [29, 53, 109].

Due to the narrow size distribution and capability of making 80 nm aluminum nanoparticles and the continuous operation without requiring replenishment of materials from Earth, the laser ablation method is selected for the production of the aluminum fuel particle.

In order to create a solid rocket grain for ALICE rocket propellant, it is necessary to manufacture aluminum nanopowder which must be mixed with water before use. However, there is a trade-off involved in manufacturing these nanoparticles for the purpose of combustion.

On the one hand the relative volume and mass of an oxide layer for a given thickness decrease as the diameter of the total particle increases. This is described in fig. 7.8a where the oxide percentage of the particle is depicted as a function of the thickness as given by equations, 7.46, 7.47, 7.48 and 7.49. It can be seen that the percentage of non-reactive aluminum oxide for a particle with an oxide layer thickness of 2 nm is 2, 8 and 20 % for a total particle diameter of 80, 200 and 1000 nm, respectively. A thickness of 2 nm is required to prevent spontaneous combustion of the ALICE grain where the aluminum would react with the neighbouring water. This means that a bigger particle size results in a higher percentage of combustible aluminum.

$$V = \frac{\pi \cdot d^3}{6} \tag{7.46}$$

Where V and d are the total volume and the total diameter of the particle, respectively.

$$V_{al} = \frac{\pi \cdot (d - 2 \cdot t)^3}{6} \tag{7.47}$$

Where t is the thickness of the oxide layer

$$V_{alox} = V - V_{al} \tag{7.48}$$

With V_{alox}, the volume of the outer oxide layer.

$$\xi_{alox} = \frac{\rho_{alox} \cdot V_{alox}}{\rho_{alox} \cdot V_{alox} + \rho_{al} \cdot V_{al}} \tag{7.49}$$

Where ξ_{alox}, ρ_{alox} and ρ_{al} are the mass fraction of the oxide in the particle, the density of the aluminum-oxide and the aluminum, respectively.

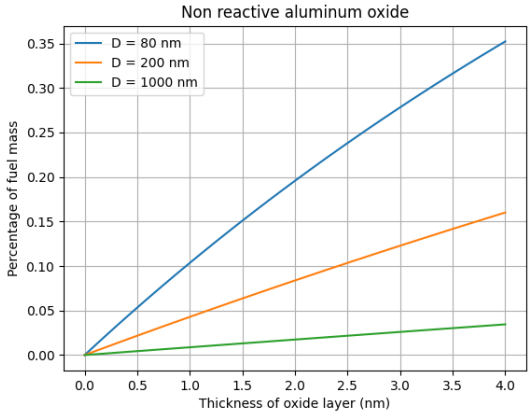

(a) Percentage oxide of the fuel particle for multiple total diameters

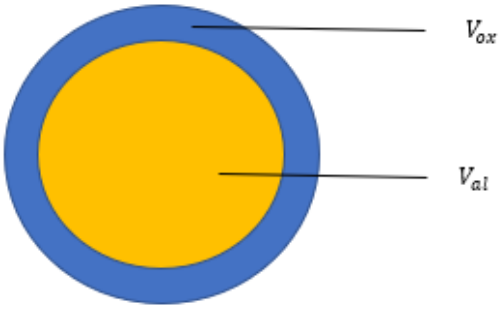

(b) Intersection of an aluminum/aluminum-oxide particle

Figure 7.7: Aluminum nanoparticle oxide layer behavior and figure

Figure 7.8a aims to explain the effect of the oxide layer on the usable mass of the fuel. It is clear that smaller oxide layers and bigger particles have the advantage.

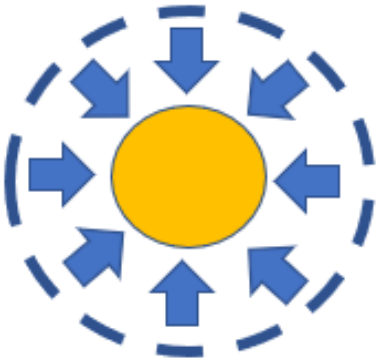

(a) Burning direction

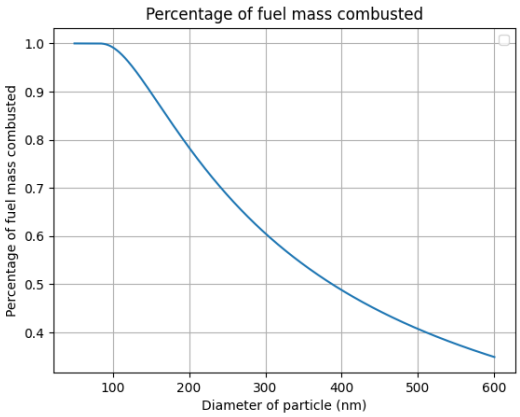

(b) Combusted percentage in combustion chamber dependent on diameter

Figure 7.8: Effect of particle size on amount of fuel burnt

The volume of the aluminum particle that remains at the end of the combustion chamber can be described by the regression rate,r, initial diameter, d, and time, t_{end}. For a given regression rate and burning time the expected remaining diameter of the particle can be described by equation 7.50.

$$V_{al} = \frac{\pi \cdot (d_s - 2 \cdot r \cdot t_{end})^3}{6} \geq 0 \tag{7.50}$$

The combusted aluminum mass can be described by:

$$\xi_c = 1 - \frac{V_{al}}{V_p} \tag{7.51}$$

Where the volume of the V_p is defined as the inner aluminum sphere that provides fuel for the combustion reaction.

For a 80 nm particle it can be concluded that the expected fraction of the particle mass is 20 %, The mass fraction of oxygen and aluminum in Al_2O_3 are 47% and 53%, respectively. In addition, the mass mixture ratio of ALICE, $\frac{O}{F}$, is 1. Therefore the mass fraction of oxygen in the fuel and propellant are 9.4 % and 4.7 %, respectively.

The estimated exergy related to the fabrication of laser-ablated aluminum nanoparticles is in the order of 25 kWh per kg of nanoparticles.

$$\begin{aligned} Ex_{in} = \eta_{al} \cdot \Big((H_{al_{2250}} - H_{al_0}) - T_0 \cdot (S_{al_{2250}} - S_{al_0}) - W_{ANP} \Big) \\ + \eta_{APox} \cdot \Big((H_{o_{2250,g}} - H_{o_0}) - T_0 \cdot (S_{o_{2250,g}} - S_{o_0}) \Big) \end{aligned}$$

The exergy that goes into the lased ablation is the exergy related to the

$$\begin{aligned} Ex_{out} = &\eta_{alox} \cdot ((H_{alox_{1600,g}} - H_{alox_0}) - T_0 \cdot (S_{alox_{1600,g}} - S_{alox_0})) \\ &+ \eta_{alox} \cdot ((H_{alox_{1600,g}} - H_{alox_0}) - T_0 \cdot (S_{alox_{1600,g}} - S_{alox_0})) \end{aligned}$$

The exergy output consists of the thermomechanical exergy of the gaseous oxygen.

$$Ex_d = Ex_{in} - Ex_{out} \tag{7.52}$$

Ex_{in}	Ex_{out}	Ex_d
9801 $\frac{kJ}{kg}$	1305 $\frac{kJ}{kg}$	8496 $\frac{kJ}{kg}$

Table 7.14: Exergy input, output and destruction aluminum particle manufacturing

8

POWER

The power consumption can be fundamentally divided into heat requirement, Q_H, and electrical demand, P_E. In order to provide these systems with the necessary energy a variety of options will be presented that can be classified as either solar energy conversion or nuclear energy. Both these power systems can provide the desired, Q_H and P_E. For solar power, solar concentrators and photovoltaic cells will be considered for heat and electricity generation. Whereas the nuclear option is focusing on nuclear reactors and RTG's (Radioisotope generators).

8.1. NUCLEAR REACTOR

Since the 1960s, the United States has invested billions of dollars into the development of space fission power through the Systems for Nuclear Auxiliary Power (SNAP) program, but with no tangible results, making it a failure. The main reason behind these failures is that the programs attempted to take on an overly difficult first step, rather than following a sufficiently simple path towards success. The key to success in any initial engineering project is simplicity, not necessarily in finding the simplest design, but in finding the easiest path through the design, development, fabrication, safety, and testing stages. Fission reactors have been proposed for space applications but pose and posed some problems. During the launch, a rocket could explode and thereby contaminating the atmosphere with radioactive substances. Also, many space applications require power in the order of magnitude of a few kilowatts meaning that small reactors capable of such energy production had to be constructed, this is being done by the Kilopower project done by NASA. In 2018 the KRUSTY (Kilopower Reactor Using Stirling Technology). The reactor is still being researched and developed for utilization. The energy output depends on the mass of the reactor, the KRUSTY prototypes are a 1 kW_e and a 10 kW_e reactor, with specifications as depicted in table 8.1. Krusty makes use of a titanium/water heat pipe radiator, Stirling power conversion, sodium heat pipes, heat shielding guilt from tungsten and lithium [74].

kW_e	kW_{th}	Reactor Mass (kg)	Mass ^{235}U (kg)	Cycle
1	4.3	134	28	Stirling
10	43.3	1500	43.7	Stirling

Table 8.1: KRUSTY: Specifications[73]

After the initial mass investment the bigger reactor is more efficient when looking at the use of the uranium isotope fuel mass, with power densities corresponding to 190 $\frac{W}{kg_{^{235}U}}$ and 1220 $\frac{W}{kg_{^{235}U}}$.

The reactor uses a uranium-molybdenum alloy as fuel and is encapsulated by a beryllium oxide reflector preventing neutrons to escape and continue the reaction. The radioactive energy generates heat that is partially converted into electric energy, the remaining thermal energy can be applied for other space systems.

The reliable year-round power that can be provided by the KRUSTY reactor makes it an attractive option for space usage, however the radioactive nature of the technology could be a problem during launch, landing, and operation. The reactor can provide both heat and electrical power to ISRU systems and the reactor efficiency does not decrease over time as with photovoltaics.

8.2. SOLAR CONCENTRATORS

Solar concentrator mirrors are a technology used to enhance the efficiency of solar energy collection. These mirrors are designed to concentrate sunlight onto a smaller area, increasing the intensity of the solar radiation. By focusing sunlight onto a receiver or photovoltaic cells, solar concentrator mirrors allow for more effective capture of solar energy. This concentration of sunlight can significantly boost the power output of solar systems and make them more cost-effective, particularly in applications where high temperatures or concentrated light are required. Solar concentrator mirrors are employed in various solar power systems, including solar thermal power plants and concentrated photovoltaic systems, contributing to the advancement of sustainable energy solutions.

First the solar intensity of the Moon ought to be calculated using:

$$I_{sol} = \frac{L_{sol}}{4\pi d^2} \tag{8.1}$$

Where L_{sol} and d are the solar luminosity and distance to the sun respectively. Where $L_{sol} = 3.828 \cdot 10^{26}$ W and the distance from the sun, d, is close to one astronomical unit throughout the year and varies between $147 - 152 \cdot 10^9$ km. Imagine the sun is a power source radiating its energy equally in all directions, for a given distance one can image a sphere with a radius equal to that distance. Dividing the power by the total area of the sphere gives the power per square meter that can be expected at that given distance from the power source, this is given by eq. 8.1.

The varying distance results in a power range known as the solar intensity of $1318.5 - 1409 \frac{\text{W}}{\text{m}^2}$, an increase of 6.86 % can be expected between the minimum and maximum values of the distance to the sun.
Solar concentrators are an area of interest since they require no consumables and make use of ISRU in the form of solar energy. Firstly the maximum amount of useful work to solar radiation energy and thus the exergy-to-energy ratio $\psi = \frac{Ex_{in}}{E_{in}}$ is given by [72]:

$$\psi(T_e) = 1 + \frac{1}{3}\left(\frac{T_e}{T_s}\right)^4 - \frac{4}{3}\left(\frac{T_e}{T_s}\right) \tag{8.2}$$

Given that $T_0 = 40\ K$ and $T_s = 5800\ K$, Therefore the useful exergy from solar radiation is about 99.1 %.

Solar concentrators can provide energy needed for the heating of ISRU processes, the heat it can transfer depends on the efficiency, η_t, the area of the lens and solar irradiance at that location.

$$Q_r = \eta_t \cdot I_{sol} \cdot A_c \tag{8.3}$$

It has been estimated that the efficiency η_t can calculated using:

$$\eta_t = \left(\eta_0 - \frac{1}{I_{sol} \cdot C} \cdot \epsilon_d \cdot \sigma \cdot (T_r^4 - T_e^4)\right) \tag{8.4}$$

Where the first term, η_0 is the optical efficiency of the solar concentrators and the second term is the loss of radiation.

$$\eta_{ex} = \frac{\left(\eta_0 - \frac{1}{I_{sol} \cdot C} \cdot \epsilon_d \cdot \sigma \cdot (T_r^4 - T_e^4)\right)}{\psi(T_e)} \cdot \left(1 - \frac{T_e}{T_r}\right) \tag{8.5}$$

η_0, I_{sol}, C, σ, ϵ_d are the optical efficiency, solar intensity, concentration ratio, Stefan-Boltzmann constant and emissivity respectively [50] and the energy loss can be described by the radiation of the solar concentrator, no heat transfer is done by convection since the lenses are operating in near vacuum conditions.

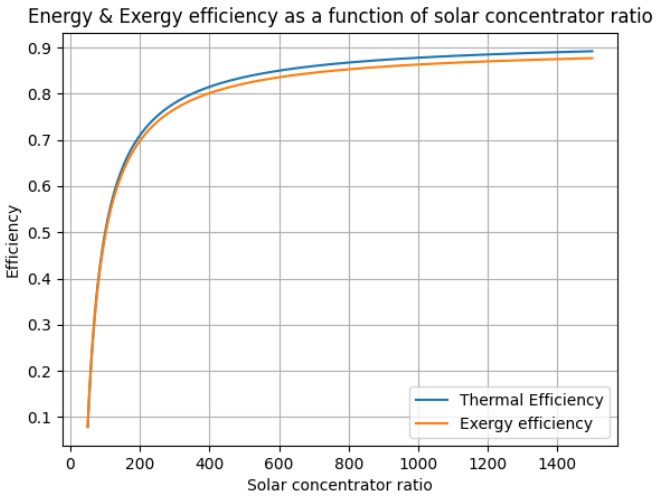

Figure 8.1: Energy and Exergy Efficiency as a function of solar concentrator ratio

Figure 8.1 explains the energy and exergy efficiency using equations 8.5 and 8.4. The behavior of the energy and exergy is very similar considering that the graph depicts the effect of the solar concentrator ratio C on the efficiency of the system. As C increases the fraction $\frac{1}{C}$ decreases, which means that the efficiency η_t approaches η_0, the reason is that the radiation surface remains the same but the concentration on it increases, the energy is added faster than it can be radiated away. The exergy efficiency is related to the energy, however, it needs to be multiplied by $\frac{1-\frac{T_e}{T_r}}{\psi(T_e)}$ which is kept constant for fig. 8.1, for a steady-state operating temperature and environment temperature.

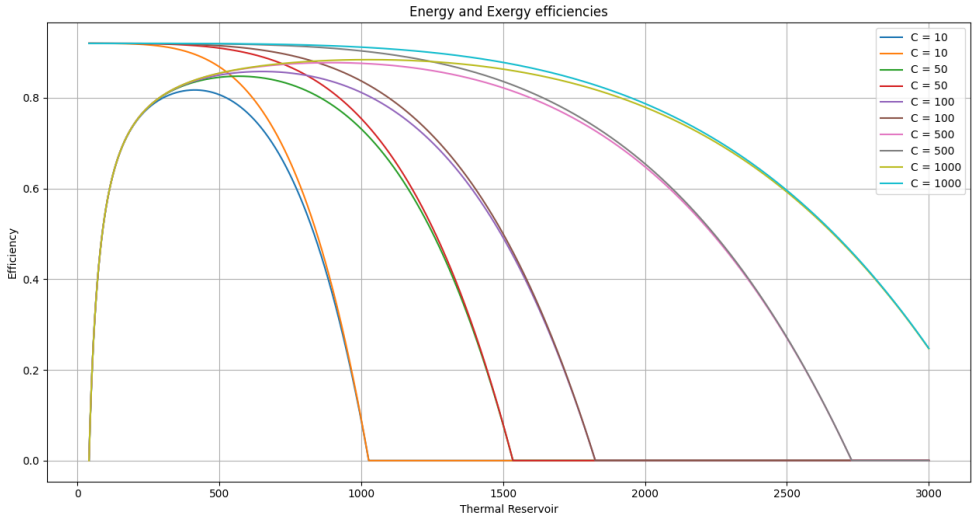

Figure 8.2: Efficiency of solar concentrators depending on solar concentrator ratio

Again equations 8.5 and 8.4 are considered. This time however the parameters that is changed is the temperature of the thermal reservoir that is being warmed up by the solar concentrators. A variety of solar concentrator ratio are looked at ranging from 10 to 1000. The effect of the temperature of thermal reservoir can be seen for these solar concentrator ratio's. Both the energy and exergy efficiency of the system decrease with increasing temperature and increase with a higher concentrator ratio. Interestingly, the energy and exergy ef-

ficiency converge as the temperature increases which is again due to the factor $\frac{1-\frac{T_e}{T_r}}{\psi(T_e)}$ because as T_r increases, this factor goes to 1. Also, the exergy efficiency has a very different behavior compared to the energy efficiency when considering lower temperatures because the factor starts at 0 for 40 K and then gradually increases. The energy efficiency starts at its peak and then only goes down, whereas the exergy efficiency has an optimum for a given solar concentration ratio, C. This behavior can be explained by the following: At low temperatures the maximum efficiency for the Carnot cycle, $1-\frac{T_e}{T_r}$, is close to 0. As the temperature increase the maximum work that can be extracted from a heat reservoir increases, however the radiation increases with increasing temperature. At some temperature T_r the optimum combination is found such that if it would increase the radiation term would result in a decrease of efficiency because the Carnot efficiency term cannot compensate for it any longer. If the temperature would decrease the radiation would decrease too but the reduction in the Carnot efficiency would be greater, meaning a greater decrease in overall efficiency.

8.3. PHOTOVOLTAICS

In the past few decades, technological advancements have led to the emergence of more efficient technologies, resulting in opportunities for more reliable and profitable energy sources. Solar cells, in particular, have piqued interest in space applications due to the consistent availability of solar power. Although PV-cells have a high specific power, the inclusion of all the necessary infrastructure for mounting and operating them leads to a reduction in specific power.

PV cells operating in space face a significant challenge due to the continuous cosmic radiation that damages the cells and reduces their efficiency. The issue is more severe in space than on Earth because the Earth's magnetic field bends particles towards the poles, whereas the high-energy particles from the sun are do reach the lunar surface as it lacks a magnetic field. The efficiency of the PV cells is influenced depending on the severity of the event. The severity of an event can impact the efficiency of PV cells. In particular, constant exposure to relatively weak radiation has been linked to an annual efficiency reduction of around 2- 3% [40]. Solar radiation poses a significant challenge in the form of strong proton events (SPEs), which result from solar storms - massive ejections of solar mass from the sun. These plumes of high-energy particles can cause damage to electronics and hardware that are exposed to space. The efficiency of monocrystalline silicon solar cells could be reduced by 20-25%, while the efficiency of multi-junction cells could be reduced by 5-10%, due to the presence of the ionized particles.

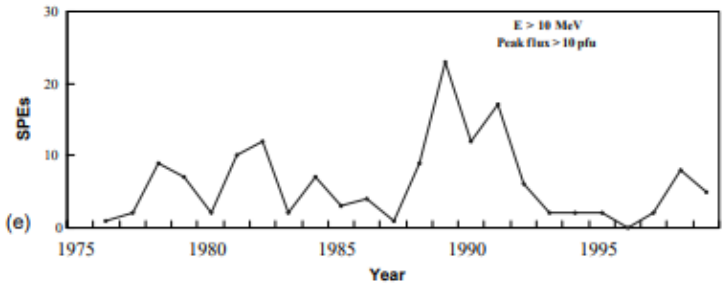

Figure 8.3: Frequency of Single Proton Events[27]

As can be seen in 8.3, an SPE is an event that is to be expected every year. The lunar architecture in general ought to be designed such that it can withstand the occurrence of an SPE, this can be done by radiation shielding or shutting the operation down to protect the hardware.

The amount of energy that would be possible to generate is given by:

$$P_{system} = \eta_{PV} \cdot S_{local} \cdot A_{panels}$$

Where η_{PV} is the efficiency of the solar panels, currently standing at 32 %.

9

RESULTS

	Ex_{in} $\frac{kJ}{kg}$
Excavator	2.74
Heating	320
Compressor	195
Electrolyzer	1130
Liquefaction	13.7
	1661

Table 9.1: Hydrolox Production

	Ex_{in} $\frac{kJ}{kg}$
Excavator	2.74
MRE reactor	90698
Laser Ablation	8190
YSZ Separator	1747
Water Extraction	928
	101566

Table 9.2: ALICE production

The tables above depict the flow of a single kg of regolith through the system. First, it is excavated, then heated and the water is sublimated out and the rest of the regolith is discarded. The water vapor is compressed, electrolyzed, and liquefied. Note that liquefaction is dependent on both the water fraction in the regolith (5.6 %) and the mass percentage of hydrogen in water (11 %). The number that is given here is the required exergy for the liquefaction of just 6.2 g of hydrogen. The same applies for all other systems meaning that in the case of the MRE the laser ablation and YSZ separator are based on the aluminum and oxygen yield, respectively.

	Hydrolox	Surplus Oxygen
Yield (g)	43.7	12.3

Table 9.3: Hydrolox Production based on a mass mixture ratio of 6.03

	ALICE	Surplus Oxygen	Silicon	Iron
Yield (g)	200	406	188	46

Table 9.4: ALICE production

After 1 kg of regolith has been fully processed, only 43.7 g of hydrolox has been produced and only 12.3 g of oxygen. For the MRE reactor this is 200 g of ALICE, 406 g of oxygen, 188 g of silicon and 46 g of iron. Note however that the water is added and based on excavation, heating and compression as done in the hydrolox process. Meaning that the 100 g of water that were added to the system were separately extracted.

The total exergy needed for the manufacturing and transportation of a payload can be calculated:

$$Ex_t = (PTP)^{-1} \cdot Ex_{prop} + Ex_{payload} \tag{9.1}$$

Note that $Ex_{payload}$ is 0 in the case of oxygen since no additional exergy is put into the system to produce it considering it is a byproduct in both architectures.

MRE	ALICE	Surplus Oxygen	Silicon	Iron	Exergy Input
Yield	1.00 kg	2.03 kg	0.940 kg	0.230 kg	508 MJ

Table 9.5: Yield and Exergy input for the production of 1 kg of ALICE propellant

PEM	Hydrolox	Surplus Oxygen	Exergy Input
Yield	1.00 kg	0.28 kg	38 MJ

Table 9.6: Yield and Exergy input for the production of 1 kg of Hydrolox propellant

ALICE Rocket	ALICE	Oxygen	Hydrolox
PTP	2.23 %	2.17 %	1.89 %
PTP-inverse	44.8	46.0	52.9

Table 9.7: Payload-to-Propellant ratio of the ALICE rocket for multiple payloads

Hydrolox Rocket	ALICE	Oxygen	Hydrolox
PTP	2.93 %	2.87 %	2.24 %
PTP-inverse	34.2	34.8	42.2

Table 9.8: Payload-to-Propellant ratio of the hydrolox rocket for multiple payloads

The exergy input of the entire process was calculated using the inverse of the payload-to-propellant ratio. As can be seen, the ALICE rocket is less efficient in terms of payload-carrying capabilities than the hydrolox rocket. For all rockets, hydrolox transportation was the least efficient, which can be explained by the low density of hydrogen requiring more and bigger tanks than oxygen of ALICE.

	ALICE	Oxygen	Hydrolox
Exergy ALICE Rocket ($\frac{GJ}{kg}$)	23.3	23.4	26.9
Exergy Hydrolox Rocket ($\frac{GJ}{kg}$)	1.81	1.32	1.64

Table 9.9: Exergy input for the transportation of 1 kg of the desired payload into LEO

The exergy input for the two rockets and three payloads are given above. The big difference between the ALICE and hydrolox rocket can be explained by the high exergetic cost of producing metals through molten regolith electrolysis.

Oxygen into LEO is the most efficient payload for both systems, albeit a small difference in the case of the ALICE rocket. In the case of the hydrolox rocket ALICE is the most costly propellant from regolith to propellant depot. The cost of manufacturing ALICE cannot be compensated for by transportation efficiency.

The exergy related to the station-keeping is so small that it will be neglected, enough krypton should be supplied from Earth to maintain the orbit.

10

Discussion

The south pole of the Moon with the presence of water, PSR, and PELs is an interesting place to start lunar space missions considering water is an essential resource and solar power is almost continuously available. South pole regolith is said to most resemble Highlands regolith and seems to be the best option for current analyses. However, the environment used in this study is based on spectrometric data acquired during space missions and studies on lunar rocks that were collected during a hand full of space missions, the reliability of any specific location on the Moon is therefore very low, it is rather a general overview of the minerals present and an indication of the expected composition. Pressure and temperature in the operating PSRs are relatively reliable since the pressure in the almost perfect vacuum on the Moon remains constant for all practical purposes. The temperature variations in the PSRs are also negligible since they appear to be in steady-state and do not depend on the night and day cycle. A deviation from these PSRs would result in a greatly fluctuating environment temperature that is highly dependent on the period of the lunar night and day cycle, making the exergy calculations more dynamic. The specific location where the operation will be effectively implemented is dependent on the local mineralogical composition of the environment. Throughout the study the water concentration was assumed to be just 5.6 % however, some locations indicated percentages of up to 30 % meaning that the environment should be redefined depending on the specified location.

Currently, many excavation methods are under consideration, mainly focused on the extraction of the relatively loose upper layer of the lithosphere which is expected to be relatively loose due to micro impact of meteorites, in later stages more specified excavation methods could be applied depending on the properties of the minerals that are being mined. Pneumatic drills could be beneficial for many excavation processes by loosening the soil before using mechanical excavators to collect the minerals. The NASA RASSOR excavator chosen for the purposes of this study remains to be tested in the lunar environment and could not be able to collect the very cold rocks present in the PSRs. The continuous operation in the PSRs may prove difficult because the harsh environment affects both the mechanical properties of the excavators and the battery that is currently used. Additionally, radiation shielding in the PSRs may not be required however for locations that do experience solar radiation it is a serious factor that must be considered.

Currently, PEM electrolyzers operating currently do have decent energy and exergy efficiency and are a good way to make pure hydrogen. The exact performance in the lunar environment remains to be seen, the operating temperature and pressure are lower than in other applications making the insulation requirement lower. However, some replenishment for the membrane, anode, and cathode is still required from Earth. The compact PEM electrolyzer is also interesting from a mass perspective considering the equipment needed for a PEM electrolyzer is lower than other industry alternatives. The exergy input of the PEM electrolyzer is the highest in the hydrolox-generating architecture, however, much of that exergy is preserved in the hypothetical reaction of oxygen and hydrogen, which is exactly what happens during the refueling operation, the non-stochiometric mass mixture ratio does lower the exergy that can be extracted leaving some of the oxygen on the Moon.

Liquefaction of hydrogen is much easier on the Moon due to the very low temperatures at which the hydrogen is stored. Passive cooling of the hydrogen until it reaches the PSR temperature has multiple advantages. It

both lowers the temperature below the critical temperature that is needed for the use of J-T throttling as well as reducing the natural para-ortho hydrogen concentration of hydrogen. No precooling from nitrogen is required and the loss due to para-ortho conversion can be reduced.

One of the major advantages of MRE reactors is that the regolith itself serves as the reactor, thus reducing the need for mass from Earth. Pure metals such as aluminum, magnesium, silicon, and titanium can be extracted through sequentially electrolyzed oxides. However, electrolyzing silicon and magnesium requires further research to prevent mixing as they operate at the same current and voltage. The extremely hot reactor operating in the lunar environment is prone to high radiation losses and requires regular replenishment of the anode and cathode. The process of heating the regolith poses several challenges, such as mitigating radiation loss and utilizing solar concentrators for heating, considering the core is the hottest place in the reactor. To address this issue, preheating the regolith and using Joule-heating during the reactor operation have been proposed as possible solutions. The required heat for the heating and melting of the regolith, the big endothermic heat requirements for the electrolysis and electrolysis itself at 2250 K and radiation losses make the MRE reactor an energy and exergy-consuming process. However, for long-term ISRU, the system is interesting from a mass injection and metal extraction point of view.

From an exergy point of view, excavation, heating and sublimation, and subsequent compression are inefficient, because the heat of sublimation is high and lost once the water is liquefied and during excavation, the material remains in the dead state. If the operation is done in a higher-pressure environment the water can be melted without the need for sublimation heat increasing the efficiency of the process. The YSZ-separator and the laser ablator are also inefficient when looking at them from an exergetic point of view, during laser ablation, the chemical potential is lost when the aluminum and oxygen are combined to form a small oxide layer around the aluminum particle, in addition to the chemical exergy loss all the exergy required for operating the laser is lost because the thermomechanical capabilities to do work w.r.t. the environment do not change and the chemical potential reduces. Passive storage of ALICE, hydrolox, and oxygen in the PSRs on the Moon is generally feasible. This is due to the very low-temperature gradient between the tanks and the environment, as well as the low absolute temperature, which directly determines radiation heating and cooling over extended periods of time. This is especially important when considering the large enthalpy difference between two temperatures for hydrogen, making temperature changes slow because much energy is needed. The contact with the lunar surface needs to be considered for a corrected estimation of the heat flow in the tanks. Although liquid oxygen remains in a liquid state when left unattended, the decrease in temperature and its associated enthalpy change reduces its combustion efficiency.

Creating a propellant depot in Low Earth Orbit (LEO) is a challenging and expensive endeavor, particularly due to the size of the depot. The construction of such a facility on the Moon or Earth would also pose significant engineering and logistical difficulties. However, using an ion engine to maintain orbit in the thin upper atmosphere of the Earth would be less challenging. A basic ion engine could keep the depot in orbit with only a limited amount of propellant mass injections needed from Earth.

Reliable power generation depends on the illumination factor of the selected location, for solar concentrator mirrors the solar concentration ratio of the lens and emission coefficient of the thermal reservoir. For each concentration ratio and emission coefficient of the thermal reservoir that is being heated an optimum in exergy efficiency exists that balances the Carnot efficiency of a heat reservoir and the thermal radiation losses. The efficient use of heat provided by the solar concentrators could prove to be difficult in the case of the MRE reactor since the MRE reactor is warmest at the core where the electrolysis happens. A higher concentration ratio translates to a higher energy and exergy efficiency since the radiation losses are lower. For increasing operating temperatures higher concentration ratios are required because the heat flow needs to be able to counter the increasing radiation losses. PV-cells are an essential part of most space missions since they use the only abundant resource that is almost always present, starlight. PV-cells for space application have efficiencies above 30 %, the magnitude of the operation however begs the question of whether the highly specialized and costly space-grade PV-cells are the best choice for the lunar architecture. The PV-cells that operate at the rim of PSRs are subjected to radiation and are expected to decrease in efficiency during their operating time. Single Proton Events can be predicted considering solar activity is being monitored, PV-cells should be protected when such an event is imminent or permanent shielding should be provided, which is difficult considering PV-cells are places such that solar radiation can be used to generate electricity. Nuclear energy has a high specific energy and can provide both heat and electricity, it is the most reliable option since it can be used irrespective of the lunar day and night cycle, KRUSTY the nuclear reactor currently in use

shows promising characteristics. For the operation that has been proposed many of these reactors should be brought to the Moon, the mass investment for the mirrors, PV-cells, and nuclear reactors will be substantial. A combination of these technologies should be used for a resilient, fault-tolerant, efficient lunar architecture.

For a high-level study to gain insight in the overall mechanics of the mission however the patched conics. Although the estimated ΔV's for the specified space mission is in the neighborhood of the values that can be found in literature, the exact staging of the two-stage rockets should be looked at again to optimize the best decoupling point. The increase in ΔV at which decoupling occurs increases the structural and propellant mass of the lower stage, an increase in ascending stage propellant mass naturally means an increase in descending stage propellant mass of the lower stage because the structure is bigger and the ΔV is higher. The lower stage ascending phase, however, affects the upper stage mass inversely, because the remaining ΔV is lower than it would otherwise be, and both the structural mass and required thrust decrease since the amount of propellant that needs to be contained decreases, which has a rippling effect through the other systems such as a decrease in nozzle mass and shell mass.

The algorithm proposed for the estimation of the total, propellant, and structural mass does converge to a unique solution for initial values that satisfy the constraints. Sometimes, however, the python package 'SciPy' iterates to impossible values of the structural mass ratio which results in negative roots or a negative value for the propellant mass, when this happens the program crashes and a new initial guess must be chosen. The subsystem structural masses that must be summed are a gross estimate and real values and additional smaller systems might influence the mass estimation.

For hydrolox rockets, values for the payload-to-propellant ratios are, 3.13, 3.77 and 3.84 percent for hydrolox, oxygen and ALICE respectively. Whereas this is The only factor that influences the difference in payload-carrying capabilities between the respective payloads is the payload structural mass which is dependent upon the density of the propellant, and the number of tanks. It is somewhat unfair to compare oxygen to the other two payloads since ALICE and hydrolox are both directly usable whereas oxygen is only the oxidizer part of a propellant. This means that the fuel part of the propellant is brought from Earth, this is interesting for both methane and hydrogen since the mass mixture ratios in methalox and hydrolox are 3.8 and 6.03 which translates to fuel mass percentages of 20.8 and 14.2 %. The vast majority of the propellant mass in both cases consists of oxygen.

For the hydrolox rocket, the numerical approximations used for the mass of the tank and the volume of the tank are independent as they are both scaled based on the propellant mass and volume. This means that it is assumed that the mass of the tank does not depend on the specific shape but only on the inner volume. The length of the cylindrical shell is a strong function of the diameter of the rocket, even though it has no direct effect on the tank mass. Extracting shape relations from the numerical data is therefore not possible because only data on the masses of propellant tanks were used in the regression analysis, typical values for diameter and rocket shapes should therefore be assumed to justify the use of these equations. The shape does however influence the insulation required to prevent heating of the liquid oxygen and hydrogen. The engine mass is the most reliable since it only depends on the GLOM of the rocket. The fairing mass of the lower stage and the upper stage are both modeled as two cylinders staked on top of each other, the relation used is however not a linear relationship this means that as the rocket gets longer the fairing mass should increase exponentially. Also, the top part of the upper stage is not a cylinder but one or two smaller payload-carrying tanks which means that the shape resembles a truncated cone and not a cylinder. The formula to estimate the structural mass of the fairing is based on a fairing structure that is required to withstand higher thrusts, about 6 times, because of the launch constraint in the gravitational field of the Earth, the fairing could therefore very well be lighter. The results of the hydrolox rocket indicate that the payload-to-propellant ratio is not affected by the diameter to a very large extent. The reason for this is that some numerical relations used for the mass estimations do not depend on the shape but are a function of the propellant mass alone, the small variation that is observed can be mainly contributed to the decrease of the fairing and avionics mass. The fairing is a function of the surface area of the rocket and the avionics depend on the length of the rocket. The increase in diameter results in a wider body of the rocket which causes a reduction in rocket length reducing the avionics mass and fairing mass. In general, the method that uses relations from regression analyses is a good first-design approximation of a rocket system's mass distribution and generally built. The approach is however more limited to the inclusion of specific rocket geometry than expected.

The most important driver scaling the ALICE rocket is the shell mass as it constitutes the biggest part of the structural mass. Unlike the case of the hydrolox rocket, the model strongly depends on the chosen diameter

of the rocket, as the diameter of the rocket increases the length can decrease however the thickness also scales with the diameter which strongly influences the mass of the rocket shell. In practice, often a configuration of multiple rocket boosters is used instead of just one, this could influence the performance of the rocket but is not taken into consideration in this study. The values derived from Ideal Rocket Theory are an indication of the real performance of the rocket, these derived values could however deviate in reality. Furthermore, the temperature and pressure in the rocket chamber are assumed to be independent of the combustion chamber geometry and constant for all rocket designs, and compatible with the chosen grain geometry. Solid rockets use inner heat control using ablation or sacrificial cooling, to prevent the melting of an Epoxy-kevlar and even steel shell. These materials have melting temperatures at which the heat flow either destroys or jeopardizes the structural integrity of the spacecraft. Some insulators could prevent steel from melting however the increase in spacecraft mass would make the design undesirable. Thermal heat flow from the combustion gases to the chamber wall is a function of the diameter, an increase reduces heat flow and thus required ablation cooling, the lack of lunar ablation materials means they need to be imported from Earth. The shell mass increases faster with an increasing diameter than the ablation mass decreases, this means that from a payload-to-propellant perspective, the overall mass ought to be minimized. However the import of ablation mass is very costly, overall the lower efficiency of the rocket compared to the hydrolox rocket in addition to the ablation mass difficulties make the ALICE refueling rocket less attractive. Unless ablative materials can be manufactured on the Moon the use of this rocket is not feasible.

In this preliminary analysis, the hydrolox rocket performs better in terms of payload-to-propellant ratio and its propellant is easier to make making the hydrolox rocket carrying oxygen to LEO the most efficient process in terms of exergy input. It should be noted that this is a very high-level analysis therefore a more synthesized design of a specific rocket can have different mission efficiencies. However, the edge the hydrolox rocket and the hydrolox propellant generation processes have over ALICE is a gap that cannot be closed in terms of exergy or rocket efficiency with current technologies. A major advantage of ALICE is the additional materials that are being produced during the propellant generation process in the MRE reactor.

ALICE rockets are in their infancy and require much more research to increase the specific impulse to make them more attractive as a propellant, the parameters used in this study were taken from literature but are based on a much smaller combustion chamber. The performance of larger ALICE rockets ought to provide insight into the feasibility of using them in missions such as the one proposed here. This study assumes the use of multiple burns in the same solid rocket combustion chamber, solid rocket grains generally burn up once ignited. However, inhibitors can be used to end a burn and restart the combustion chamber later on. Otherwise, each burn for a solid rocket requires a separate combustion chamber. The use of multiple burns in solid rockets is a field of research and is generally not done in the current space industry. The use of a bigger combustion chamber also allows for the reconsideration of bigger aluminum-powder particles since the bigger and thus longer combustion chamber allows for a longer presence in the chamber meaning that a particle has a longer time to burn up. A bigger particle means a smaller mass percentage of the oxide coating resulting in a mass reduction of redundant material in the propellant.

Hydrolox rockets are well-known rockets of which the engineering aspects and design characteristics are well documented making them attractive options for direct implementation. Even though the presence of water on the Moon is estimated to be in the $600 \cdot 10^9$ kg, this is still a small number when looking at human colonization over a period of decades or centuries, the use of propellants that do not use water or its elements is preferable in order to prevent wasting the valuable water that is available on the Moon.

11

Conclusion

When examining the research questions, the project had a dual focus. Firstly, it assessed the exergy destruction associated with logistic and technological processes for in-situ lunar propellant generation and transportation to a refueling orbit. This involved investigating the lunar environment's characteristics, including available resources, thermodynamic properties, potential power sources, and ambient conditions. The project also analyzed feasible logistical and technological processes, calculated the exergy requirements for propellant acquisition, transportation, and processing, evaluated exergy storage needs, and determined exergy losses during refueling operations. Secondly, the project aimed to identify the most exergy-efficient propulsion system for refueling operations. This was achieved by analyzing critical factors like spacecraft dimensions, propellant selection, and technological considerations, while also exploring the exergetic efficiency of different propellant transportation methods using various rocket systems. Additionally, the project sought to determine the exergy requirements of a propellant depot, further enhancing the understanding of overall exergy utilization.

One of the aims was to define the lunar environment. It can be concluded that further research on the lunar environment is necessary to obtain reliable results, this is required for the development of specialized equipment tailored to the unique conditions of the Moon. Solar energy availability, operating conditions, and mineralogical and chemical composition are all affected by the location on the lunar surface.

Estimations of the thermodynamic characteristics of lunar regolith have been provided, revealing that the chemical composition of the lunar environment exhibits some variation across different latitudes. This environment can be categorized into three distinct types: low-Ti Mare, High-Ti Mare, and Highlands regolith. Each of these categories represents a unique combination of the minerals plagioclase, pyroxene, olivine, and ilmenite, which vary in concentration. By identifying the thermodynamic properties and densities of these minerals, we can employ them for thermodynamic analyses.

The ambient conditions on the Moon are strongly influenced by the latitude and time of day, encompassing a temperature range of 40-350 K. By considering these ambient conditions and the chemical composition of the lunar environment, we can establish the standard chemical exergies of the substances present in the lunar environment. Some places near the South Pole are especially interesting because of their almost continuous exposure to sunlight.

Radiative losses in the lunar environment pose a significant challenge that must be addressed to optimize the utilization of lunar power resources. Of particular concern are the solar concentrator mirrors required for regolith heating, which are highly susceptible to radiation-induced energy losses to the point that some operating temperatures are no longer feasible. The high radiation losses in the lunar environment make processes operating at lower temperatures more preferable from an energy perspective. This underscores the need for careful consideration and mitigation of radiation losses in the design and operation of lunar power systems. The PSRs on the lunar surface offer favorable conditions for the liquefaction and cryogenic storage of oxygen and hydrogen, considering the influence of radiation is thousands of times less prevalent than on Earth and no convection occurs in the vacuum of the Moon.

Based on a careful review of existing literature, two specific processes have been identified as capable of producing ALICE and hydrolox propellant. However, it is important to note that there are numerous other techniques and methodologies that remain unexplored and may potentially offer greater efficiency. Long-term storage of cryogenic propellants and liquefaction processes benefit from the cold lunar environment because the required work that needs to be put into the system is much lower compared to Earth.

To assess the energy efficiency of the chosen processes, the exergy cost has been estimated by considering factors such as the required heat and work, as well as the changes in enthalpy and entropy relative to the environment. These considerations provide insights into the overall energy expenditure associated with these processes.

Importantly, both the ALICE and hydrolox manufacturing processes offer the advantage of producing surplus oxygen that can be efficiently utilized for various purposes. This surplus oxygen can be directly utilized to refuel rockets without necessitating additional energy consumption or exergy expenditure. This characteristic significantly enhances the overall efficiency of these processes.

Moreover, in the case of molten regolith electrolysis employed for ALICE production, the process yields additional byproducts in the form of silicon and iron. These byproducts have considerable potential for applications beyond the immediate production of propellant. Their utilization can contribute to the development of diverse technological advancements and further enhance the overall value and versatility of the process.

The analysis shows that for 80 nm aluminum particles, the expected fraction of non-reactive aluminum oxide is 20 %. This information is essential for understanding the composition of the ALICE rocket propellant. The mass fraction of oxygen and aluminum in aluminum oxide is 47 % and 53 %, respectively. Considering the mass mixture ratio of ALICE, the fuel and propellant have calculated mass fractions of oxygen of 9.4 % and 4.7 %, respectively.

In conclusion, the analysis emphasizes the importance of particle size and oxide layer thickness in manufacturing aluminum nanoparticles for the ALICE rocket propellant using the laser ablation method. However, it is necessary to navigate a trade-off. Larger particle sizes result in a higher proportion of combustible aluminum and a reduced percentage of non-reactive aluminum oxide. Yet, these larger particles also have an extended burn time, increasing the risk of incomplete combustion if they leave the chamber prematurely.

To optimize the manufacturing process and ensure efficient propellant performance, striking a balance between particle size, oxide layer thickness, and burn time is crucial. It is recommended to conduct further research to refine manufacturing parameters and gain a better understanding of ALICE propellant combustion. Notably, it should be acknowledged that the nanoaluminum particle manufacturing process is highly destructive from an exergy perspective.

The production of ALICE and hydrolox propellants are exergy-consuming processes requiring 508 MJ and 38 MJ for a single kg, respectively. MRE reactors can produce multiple metals for ISRU use and do not require much equipment from the Earth. At other locations, it can also extract titanium. Solar radiation and Strong Proton Events are expected to reduce the efficiency of PV cells, which is difficult to mitigate since PV cells require solar radiation to generate electricity. Hydrolox has a clear advantage over ALICE in terms of exergy input per kg of propellant. The payload-to-propellant ratios are comparable for the optimized case of both rocket systems. The optimal case for the payload-to-propellant ratio of the ALICE rocket requires more ablative material than a less optimal one, the ablative material mass remains a major problem and makes the whole operation unfeasible. MRE can produce aluminum, iron, silicon and oxygen and remains an interesting option for the extraction of resources required for longer human presence.

The selected refueling orbit is located at a Low Earth Orbit (LEO) of 420 km. This choice aims to minimize the energy required for the initial orbit insertion of spacecraft departing from Earth. By positioning the refueling orbit at a relatively low altitude, the spacecraft leaving Earth can efficiently rendezvous and dock with the refueling station, reducing the fuel and energy expenditure needed to reach their desired destination or higher orbit. This strategic decision optimizes the overall mission efficiency and enables more effective utilization of resources during space operations.

An ion thruster is utilized to counteract the orbital decay of the propellant depot. The mass and power requirements of the ion thruster are influenced by the propellant density, as well as the specific characteristics of the propellant being used.

The propellant density, as mentioned earlier, plays a significant role in determining the size, projected area, krypton mass, and power requirements of the thruster. It should be noted that the density of hydrolox is determined based on a mass mixture ratio of 6.03 and the densities of liquid oxygen and hydrogen. The exergy cost to maintain ALICE, oxygen and hydrolox propellant are 0.423 $\frac{kJ}{kg}$, 0.485 $\frac{kJ}{kg}$, and 1.04 $\frac{kJ}{kg}$. Consequently, the ion thruster would consume approximately 0.439 kg of krypton for ALICE, 0.497 kg for oxygen propellant, and 1.07 kg for hydrolox propellant.

A combination of nuclear and solar will be used for power, the reliable continuous power provided by nuclear reactors make them an interesting option for space implementation, solar concentrators are relatively easy low-cost options to acquire power, however radiation losses and the efficiency of PV cells reduce the attractiveness of solar power, batteries that would be needed to store solar energy would greatly reduce the specific power of the system. Very high-temperature operation of solar concentrator mirrors limit their efficiency since radiation losses can no longer be mitigated.

The numerical relations used for the estimation of the subsystem masses of the hydrolox rocket are only weakly related to the shape of the rocket, for more specific designs another approach must be taken. Ablative material increases with a smaller diameter whereas shell thickness and mass increase which creates a trade-off. Ablative material ought to be manufactured on the Moon to reduce the mass injection from Earth, otherwise, the ALICE rocket is very expensive and dependent on supplies from Earth. The expected payload-to-propellant ratio for the fully reusable two-stage rockets for ALICE and hydrolox is in the range of 1.89-2.23 % and 2.24-2.93 % percent, making the hydrolox rocket more efficient. The exergy input for the transportation of a single kg of payload range from 1.32-1.81 $\frac{\text{GJ}}{\text{kg}}$ for the hydrolox rocket and from 23.3-26.9 $\frac{\text{GJ}}{\text{kg}}$ which is a difference of one order of magnitude. The hydrolox rocket is more interesting from an exergy point of view. Oxygen remains a good option because of its abundance in space, transportation efficiency, and use in multiple propellants. It also requires a smaller propellant depot.

12

RECOMMENDATIONS

Comparing the refueling rockets for propellant transportation from Earth and the Moon to Low Earth Orbit (LEO), it becomes apparent that the respective ΔV values of 9.3 km/s and 6.1 km/s for Earth and the Moon strongly suggest that propellant transportation from the Moon is more efficient. This implies that conducting mass estimates and initial investment analyses for building the required infrastructure is crucial in determining the project's payback period.

In the space environment, systems operating at approximately 298 K face increased energy losses compared to their counterparts on Earth. Despite this challenge, numerous devices are specifically designed to function optimally at such temperatures. Moreover, high-temperature applications in space encounter faster power dissipation rates compared to similar processes on Earth. Therefore, mitigating radiation losses becomes imperative to ensure the overall efficiency and effectiveness of propellant manufacturing and other high-temperature operations in space.

Apart from the initial heating of the regolith and the lower power requirement of liquefaction and cooling on the moon, the processes on the Moon and Earth are comparible.

In space, there is no atmosphere to provide insulation or regulate temperature, which means that thermal management becomes more challenging. The absence of ambient heat and the extreme temperature conditions in space necessitates careful design considerations to mitigate energy losses during propellant manufacturing processes.

However, cryogenic cooling is relatively easier in space due to the absence of ambient temperature. Cryogenic systems can take advantage of the cold environment in space to reduce power requirements for cooling. By leveraging the low temperatures of space, cryogenic systems can achieve more efficient cooling and minimize energy losses.

To enhance spacecraft performance during the two stages, the decoupling phase should be optimized, this is done by optimizing the ΔV's using a more advanced method for orbital mechanics than the currently used patched conics method, considering the Earth-Moon reference frame is a strong restricted three-body problem for Earth-Moon trajectories. This involves a comprehensive analysis of the spacecraft's trajectory and the forces acting upon it, along with precise calculations of the necessary ΔV's required to achieve the desired maneuver.

To enhance the performance of ALICE propellants, it is crucial to conduct a scientific investigation on increasing their specific impulse. This research aims to improve the efficiency and effectiveness of the ALICE propellants. By focusing on increasing the specific impulse of ALICE propellants, it is possible to achieve higher thrust and thus reduce propellant mass, which are critical factors in enabling long-duration space missions. Therefore, an in-depth exploration of the methods and techniques for enhancing the specific impulse of ALICE propellants is essential in advancing the field of space propulsion and enabling future space exploration and habitation. It is recommended to research the effects of varying mass mixture ratio and the effects of nanoparticle size. A different mass mixture ratio could have better performance, also the reduction in nanoparticle size minimizes the percentage of aluminum-oxide in propellants. Maybe, this could be

achieved by employing aluminum particle sizes tailored to the length of the solid rocket combustion chamber, as the propellant is further away from the exhaust nozzle the time in the combustion chamber is longer, thus increasing the time a nanoparticle has to fully combust. To ensure optimal performance and feasibility of a propellant depot in low Earth orbit, it is imperative to conduct a detailed design process that accounts for factors such as shape and drag. Additionally, this design process should consider the engineering possibilities constructing such a depot in-space and of accommodating multiple propellants within the same depot. A comprehensive approach to propellant depot design would enable the aerospace industry to establish a reliable and efficient method for storing and accessing propellants in space, once the specific design is known the energy and mass input related to station-keeping can be deduced. The preliminary design of the two rockets is only an indication, a specialized design with in-depth engineering of all rocket components for the specified mission characteristics ought to be conducted. The use of different materials could be explored to reduce overall mass as well as different shapes considering the rocket does not require an aerodynamically efficient shape because it operates in the vacuum of space. Other mission parameters such as the payload mass could be looked at to increase the payload-to-propellant ratio directly reducing the exergy destruction and increasing the overall efficiency of any space mission that would be conducted using the lunar rocket module. Exploring alternative propellants that do not rely on water is necessary due to the scarcity of this resource. water should be prioritized in the long-term towards its utilization for human space colonization rather than using them for propellant purposes. Further investigation into the development of ablative materials capable of being produced on the lunar surface could enhance mission effectiveness and reduce the amount of payload required from Earth.

To obtain a more accurate assessment of the energy potential of the lunar environment, we propose updating the values for the standard chemical exergy based on a deeper understanding of the mineral distribution on the Moon and the specific concentration of respective elements within those minerals, once more mineralogical research has been conducted. This will allow for a more precise measurement of the maximum amount of useful work that can be extracted from substances within the lunar environment, taking into account the temperature and pressure of the specified location.

To optimize the mining of regolith on the Moon, we propose adopting a more selective approach that takes advantage of the ability to melt water at higher pressures instead of sublimating it. By redirecting the resulting molten water, the energy required for sublimation and compression could be reduced, making it more efficient to extract water from the regolith. This approach could also facilitate the collection and utilization of water, enabling more effective resource utilization on the Moon. To gain a more comprehensive understanding of the lunar environment, further investigation into the thermodynamic properties of regolith is essential. By expanding our knowledge of these properties, we can better evaluate the feasibility of various resource extraction and utilization techniques, and develop more effective strategies for sustainable exploration and development of the Moon. To ensure accurate assessments of the efficiency and feasibility of MRE electrolysis, it is crucial to incorporate radiation losses into calculations and develop methods to mitigate these losses. This is particularly important given the high operating temperatures of MRE electrolysis, which can lead to significant energy losses if not properly accounted for. By identifying and implementing strategies to reduce these losses, we can improve the overall efficiency and sustainability of lunar resource utilization, paving the way for long-term exploration and development of the Moon.

To advance our understanding and capability in lunar aluminum production, further investigation into alternative methods is imperative. The development of novel techniques for the manufacturing of aluminum on the lunar surface is critical in overcoming the inherent challenges of extraterrestrial manufacturing, such as the lack of resources, harsh environmental conditions, and high cost. As such, a scientific exploration into alternative approaches to lunar aluminum production may yield more efficient, sustainable, and cost-effective methods that can be applied for future space exploration and habitation missions.

Further investigation into refined options for the separation of metals from the MRE reactor is recommended to optimize the process. This would facilitate the efficient extraction of pure metals from the molten regolith mixture.

A comprehensive and systematic trade-off analysis should be conducted to facilitate the selection of appropriate power systems for specific applications. This analysis should consider factors such as energy output, efficiency, cost-effectiveness, and technological feasibility, as well as unique requirements and constraints of each application, such as power demand, geographic location, and regulatory frameworks. The results of this analysis can guide decision-making and inform the selection of optimal power systems for sustainable

energy generation and utilization on the Moon.

APPENDIX

A: PATCHED CONICS & ΔV

Now the parking orbit around Earth is kept constant at 420 km. The trajectory ΔV is minimized using the 'SciPy' package in Python that optimizes ΔV_0, δ_0 and λ_0 is used to minimize the following objective function:

$$\Delta V_{tot} = \Delta V_0 + \Delta V_p + \Delta V_{Hohmann} + \Delta V_{landing} \tag{12.1}$$

ΔV_0	ΔV_p	$\Delta V_{Hohmann}$	$\Delta V_{Landing}$	ΔV_{tot}
3.140 $\frac{km}{s}$	0.643 $\frac{km}{s}$	0.478 $\frac{km}{s}$	1.678 $\frac{km}{s}$	5.939 $\frac{km}{s}$

Table 12.1: ΔV requirements for mission stages

Parameters	ΔV_0	δ_0	λ_0
Values	3.140 $\frac{km}{s}$	13.59 °	59.72 °

Table 12.2: Optimized variables for a lunar trajectory

B: Regolith Properties

Density approximation for various types of regolith

$$\rho = \frac{r_1}{r_2 + r_3 \cdot (T - 1873)} \tag{12.2}$$

where the coefficients r_1, r_2 and r_3 are dependent on the type of regolith and tabulated below:

	r_1	r_2	r_3
Highlands	6.345e4	24.11	12.06e-3
High-Ti Mare	6.333e4	22.48	19.82e-3
Low-Ti Mare	6.384e4	23.01	16.12e-3

Heat capacity model for various types of lunar regolith

1.

$$c_p = \begin{cases} -2.32 \cdot 10^{-2} + 2.13 \cdot 10^{-3} \cdot T + 1.50 \cdot 10^{-5} \cdot T^2 - 7.37 \cdot 10^{-8} \cdot T^3 + 9.66 \cdot 10^{-11} \cdot T^4 & if \quad T < 350K \\ 8.820 \cdot 10^{-1} + 0.3083 \cdot 10^{-3} \cdot T - \frac{2.278 \cdot 10^4}{T^2} & if \quad 350K < T < 1500K \\ 1.531 & if \quad T > 1500K \end{cases} \tag{12.3}$$

2.

$$c_p = \begin{cases} -2.32 \cdot 10^{-2} + 2.13 \cdot 10^{-3} \cdot T + 1.50 \cdot 10^{-5} \cdot T^2 - 7.37 \cdot 10^{-8} \cdot T^3 + 9.66 \cdot 10^{-11} \cdot T^4 & if \quad T < 350K \\ 9.093 \cdot 10^{-1} + 0.2870 \cdot 10^{-3} \cdot T - \frac{2.469 \cdot \cdot 10^4}{T^2} & if \quad 350K < T < 1500K \\ 1.539 & if \quad T > 1500K \end{cases} \tag{12.4}$$

3.

$$c_p = \begin{cases} -2.32 \cdot 10^{-2} + 2.13 \cdot 10^{-3} \cdot T + 1.50 \cdot 10^{-5} \cdot T^2 - 7.37 \cdot 10^{-8} \cdot T^3 + 9.66 \cdot 10^{-11} \cdot T^4 & if \quad T < 350K \\ 9.530 \cdot 10^{-1} + 0.2524 \cdot 10^{-3} \cdot T - \frac{2.645 \cdot 10^4}{T^2} & if \quad 350K < T < 1500K \\ 1.565 & if \quad T > 1500K \end{cases} \tag{12.5}$$

Where (1.), (2.), and (3.) are the models for the heat capacity ($\frac{kJ}{kg}$) of High-Ti Mare, Low-Ti Mare, and Highlands regolith respectively [33, 92]. The polynomial to define the regolith below 350 K is independent of regolith type whereas the type does influence the heat capacity above 350 K. This is simply because, during the study of the low-temperature heat capacity, no distinction was made between regolith types.

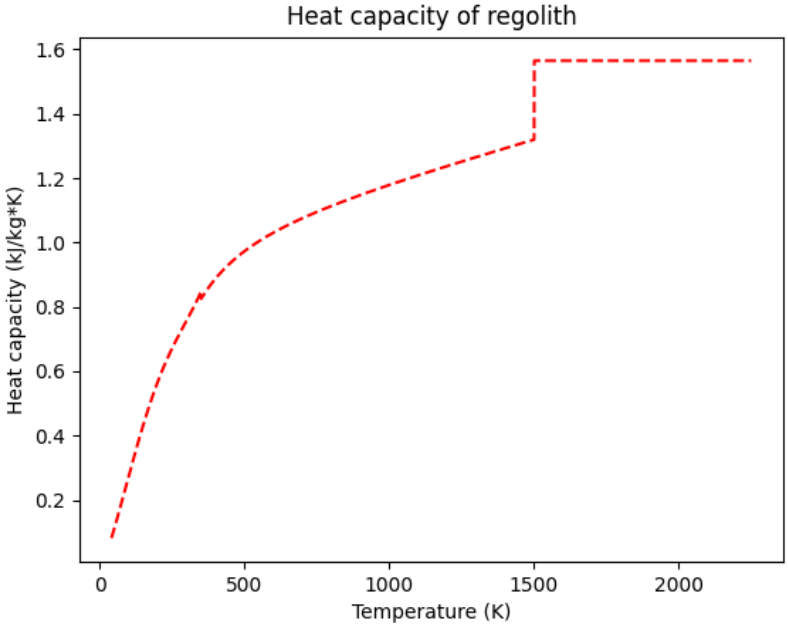

Figure 12.1: Heat capacity of Highlands regolith as a function of temperature

In fig. 12.1 it can be clearly seen that the heat capacity of regolith changes as the regolith is heated up. At 1500 K a sudden jump can be seen, this jump is related to the melting of the regolith, meaning that the solid regolith changes phase to a liquid.

LATENT HEAT FOR VARIOUS TYPES OF LUNAR REGOLITH AND MINERALS

	Highlands	High-Ti Mare	Low-Ti Mare	Latent Heat ($\frac{kJ}{mol}$)
Plagioclase	0.7320	0.2830	0.2875	134.3
Pyroxene	0.2440	0.5945	0.5890	65.1
Olivine	0.0230	0.0465	0.0880	83.2
Ilmenite	0.0010	0.0760	0.0355	21.7
Latent Heat ($\frac{kJ}{kg}$)	478.6	449.2	457.7	

Table 12.3: Latent heat and molar concentration of multiple minerals in different types of regolith

C: Thermodynamic Properties

Fe	H ($\frac{kJ}{kg}$)	S ($\frac{kJ}{kgK}$)
40 K	-98.50	-0.2127
2250 K	1439.0	1.967

Si	H ($\frac{kJ}{kg}$)	S ($\frac{kJ}{kgK}$)
40 K	57.09	2.87
2250 K	1890	3.540

Table 12.4: Iron and Silicon properties

H_2O	p (bar)	H ($\frac{kJ}{kg}$)	S ($\frac{kJ}{kgK}$)		
40 K	$3 \cdot 10^{-15}$	-703.15	-4.283		
260 K	2	-351.1	-1.289	U ($\frac{kJ}{kg}$)	v ($\frac{m^3}{kg}$)
360 K	0.01	2662.4	8.381	2496.5	16.586
360 K	2	363.90	1.156	363.69	0.0010336

Table 12.5: Properties of water

O_2	H ($\frac{kJ}{kg}$)	S ($\frac{kJ}{kgK}$)
40 K	36.06	8.17
90 K	-128.5	2.99
360 K	363.90	1.1562
1600 K	1383.3	8.138
2250 K	2146.3	8.538

Table 12.6: Properties of oxygen

H_2	p (bar)	H ($\frac{kJ}{kg}$)	S ($\frac{kJ}{kgK}$)	c_p ($\frac{kJ}{kgK}$)
17 K	2	-28.964	-1.6225	8.0954
40 K	$3 \cdot 10^{-15}$	670.57	86.608	10.313
40 K	2	656.47	26.541	10.848
40 K	30	357.49	9.9202	32.829
360 K	2	4822.2	53.282	14.446

Table 12.7: Properties of hydrogen

FLOW DIAGRAMS

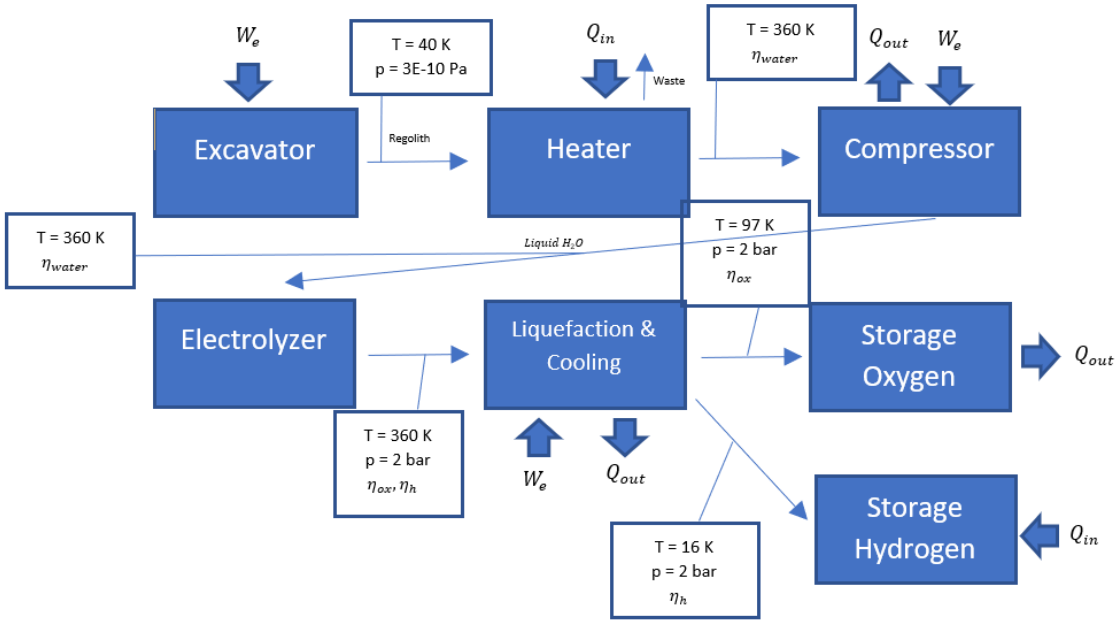

Figure 12.2: The schematic process of oxygen and hydrogen extraction through water electrolysis for hydrolox production

Figure 12.2 illustrates the processes involved in the production of hydrolox rocket propellant. First, the regolith is extracted and heated, during heating the water sublimates and is subsequently directed to the compressor whereas the rest of the regolith is discarded. Then the water is isothermally compressed to 2 bar before it continues to the electrolyzer. The stoichiometric ratio of hydrogen and oxygen is then liquefied using passive cooling and a J-T valve. The products are then transported to the storage tanks.

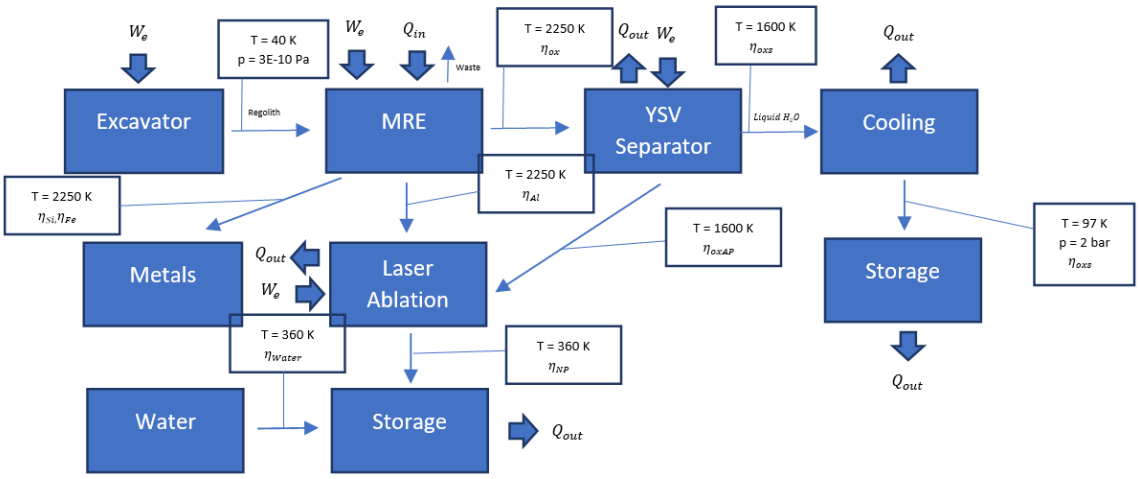

Figure 12.3: The schematic process of oxygen and aluminum extraction through molten regolith electrolysis for ALICE production

Figure 12.3 illustrates the processes involved in the production of ALICE rocket propellant. First, the regolith is extracted and heated, the molten regolith is then electrolyzed where the metals and oxygen of the oxides

making up the regolith are separated. During this process the respective yields for oxygen, iron, silicon and aluminum are given by η_{ox}, η_{Fe}, η_{Si}, η_{Al}. The oxygen is separated from other trace volatiles in the mixture by a YSZ-separator, it is partly redirected, η_{oxAP}, to the laser ablator to produce the oxide layer around the aluminum nanoparticles. The remaining oxygen, η_{oxs}, is cooled and stored. The iron, η_{Fe}, and silicon, η_{Si}, are separated and stored. The aluminum nanoparticles, η_{NP}, are created by laser ablation and then added to the water, η_{water}.

D: Rocket Materials and Characteristics

	ΔV_a	ΔV_d
Stage 1	2155 $\frac{\text{m}}{\text{s}}$	2155 $\frac{\text{m}}{\text{s}}$
Stage 2	3784 $\frac{\text{m}}{\text{s}}$	5939 $\frac{\text{m}}{\text{s}}$

Table 12.8: Ascend and descent ΔV's for the respective stages of the two-stage rocket

Hydrolox

I_{sp}	$\frac{O}{F}$	ρ_h	ρ_{ox}	$m_{payload}$	g_0	g_{Moon}
432 s	6.03	71 $\frac{\text{kg}}{\text{m}^3}$	1140 $\frac{\text{kg}}{\text{m}^3}$	50000 kg	9.8065 $\frac{\text{m}}{\text{s}^2}$	1.62 $\frac{\text{m}}{\text{s}^2}$

Table 12.9: Propellant properties of hydrolox and gravitational parameters of the Earth and Moon

The values above were used as input parameters for the proposed algorithm for the estimation of the hydrolox performance.

ALICE

R_M	I_{sp}	ρ_{ALICE}	T_c	p_c	ξ_{nozzle}	c^*	C_F	γ	μ
307.9 $\frac{\text{J}}{\text{kgK}}$	284.7 s	1370 $\frac{\text{kg}}{\text{m}^3}$	3084 K	69 bar	0.94	1361 $\frac{\text{m}}{\text{s}}$	1.93	1.32	$9 \cdot 10^{-5}$ Pa·s

Table 12.10: Combustion chamber and propellant performance characteristics for the ALICE rocket optimization algorithm

σ_{yield}	ρ_{shell}	S	f
$1350 \cdot 10^6$ Pa	1350 $\frac{\text{kg}}{\text{m}^3}$	1.4	0.95

Table 12.11: Mechanical Properties and propellant filling factor of the Epoxy Kevlar Shell

T_{abl}	c_p	ρ_{abl}	C_{abl}
835 K	1110 $\frac{\text{J}}{\text{kgK}}$	513 $\frac{\text{kg}}{\text{m}^3}$	47 $\frac{\text{MJ}}{\text{kg}}$

Table 12.12: Ablative properties and density of Avcoat39-5026

t_{nozzle}	ρ_{nozzle}	$\frac{A_e}{A_t}$
5 cm	2500 $\frac{\text{kg}}{\text{m}^3}$	40

Table 12.13: Nozzle shape parameters and density

E: Atmospheric Model

The following model can be used to estimate the density of the atmosphere, this model can be used to calculate the orbital decay [63].

$$\begin{aligned} T &= -131.21 + 0.00299 \cdot h \quad h > 25000 \\ p &= 2.488 \cdot \left(\tfrac{T+273.1}{216.6}\right)^{-11.388} \quad h > 25000 \end{aligned} \tag{12.6}$$

$$\begin{aligned} T &= -56.46 \quad 11000 < h < 25000 \\ p &= 22.65 \cdot e^{1.73 - 0.000157 \cdot h} \quad 11000 < h < 25000 \end{aligned} \tag{12.7}$$

$$\begin{aligned} T &= 15.04 - 0.00649 \cdot h \quad h < 11000 \\ p &= 101.29 \cdot \left(\tfrac{T+273.1}{288.08}\right)^{-11.388} \quad h < 11000 \end{aligned} \tag{12.8}$$

with the density function of air described as:

$$\rho_{air} = \frac{p}{0.2869 \cdot (T + 273.1)} \tag{12.9}$$

Where T, p, h and ρ are temperature, pressure, altitude and density in °C, kPa, m and $\frac{kg}{m^3}$.

F: SANKEY-DIAGRAMS

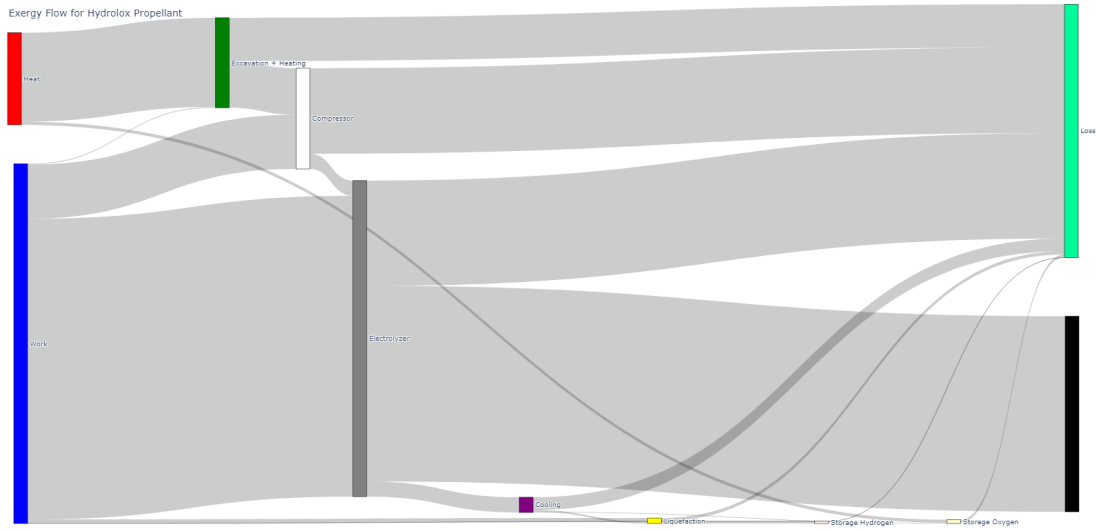

Figure 12.4: Sankey-diagram of hydrolox production

To get an understanding of the exergy flow related to the manufacturing of hydrolox figure 12.5 can be used. On the left the total exergy input is clarified and divided up into heat and work for clarification. The regolith travels through the process, the excavation, heating and phase change uses heat and very little work for excavation. It can be seen that half the exergy remains, then the water is fed into a compressor where it is prepared for the electrolyzer. This compression is a highly exergy-inefficient process where the latent heat related to the vaporization is lost. The exergy that remains is related to the enthalpy of the heated water, this then goes through the electrolyzer, which requires a lot of work. This step splits the oxygen and hydrogen, when this is reversed the combustion of the propellant happens. When looking at the diagram, the exergy that flows out of the electrolyzer is either lost, stored in propellant or passed on to the next process, only the thermomechanical exergy is considered now for the further processes, whereas the exergy of combustion is kept aside. The thermomechanical exergy of the oxygen and hydrogen reduces as they get closer to the ambient conditions. The liquefaction process is only a small part of the exergy budget. The liquefied fuel and oxidizer are stored. During the storage period, exergy is lost because of the temperature change of hydrogen and oxygen, since they get closer to ambient conditions.

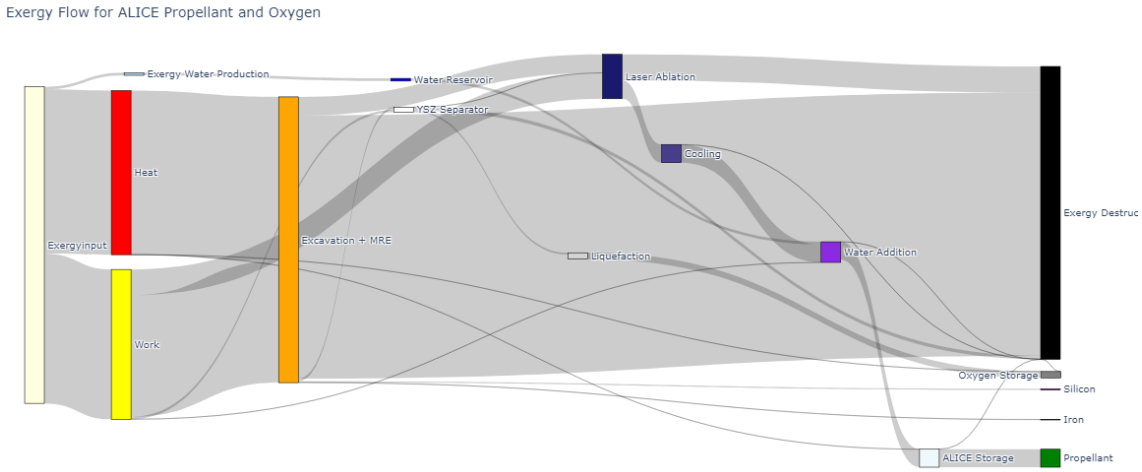

Figure 12.5: Sankey-diagram of ALICE production

When examining Figure 12.5, we can observe the exergy flow within the ALICE production system. The exergy input is divided into heat and work components, accompanied by an additional exergy-consuming process for water production. This process relates to the production of liquid water from the icy regolith. It is evident that the exergy input is substantial during the electrolysis of the regolith. The heat required for the endothermic electrolysis reaction is notably high due to the elevated operating temperature. Additionally, a considerable amount of exergy input is needed for heating the regolith and carrying out the electrolysis.

The MRE reactor experiences a significant exergy loss; however, the remaining exergy can be extracted from the thermomechanical and chemical exergy of oxygen and aluminum. The MRE reactor yields silicon and iron, which are subsequently stored. Nevertheless, both oxygen and aluminum undergo processes that are inefficient in terms of exergy. In the case of the YSZ-separator and the laser ablator, the work required for their operation is lost, leading to a decrease in chemical exergy as well. The oxygen and aluminum are cooled, and the oxygen is further liquefied before being stored. Meanwhile, the aluminum fuel particles are mixed with water and subsequently stored.

G: YSZ-SEPARATOR

n	F	I	T	ΔYSZ	j	S
4	96485.33 $\frac{sA}{mol}$	7643 A	1600 K	0.25 cm	0.4 $\frac{A}{cm^2}$	1.9 m^2

Table 12.14: YSZ separator variables

BIBLIOGRAPHY

[1] A. Adami, M. Mortazavi, and M. Nosratollahi. A new approach to multidisciplinary design optimization of solid propulsion system including heat transfer and ablative cooling. *Journal of Aerospace Technology and Management*, 9:71–82, 2017.

[2] D. Akin. Mass estimating relations, September 2021.

[3] J. Akyeampong, S. J. Udoka, G. Caruso, and M. Bordegoni. Evaluation of hydraulic excavator human–machine interface concepts using nasa tlx. *International Journal of Industrial Ergonomics*, 44: 374–382, 2014.

[4] G. Andreatta and K. Tessmar-Raible. The still dark side of the moon: Molecular mechanisms of lunar-controlled rhythms and clocks. *Journal of Molecular Biology*, 432:3525 – 3546, 2020.

[5] ArianeGroup. Vulcain® 2.1 engine, solutions for commercial and scientific payloads. 2019.

[6] M. Aziz. Liquid hydrogen: A review on liquefaction, storage, transportation, and safety. *Energies*, 2021.

[7] A. Baladi and R. S. Mamoory. Investigation of different liquid media and ablation times on pulsed laser ablation synthesis of aluminum nanoparticles. *Applied Surface Science*, 256:7559–7564, 2010.

[8] M. Bellini, J. Bösken, F. Bartoli, and F. Vizza. Remarkable stability of a molecular ruthenium complex in pem water electrolysis. *Chemical Science*, 13, March 2022.

[9] M. Bernt, M. Singer, and H. A. Gasteiger. Analysis of voltage losses in pem water electrolyzers with low platinum group metal loadings. 2017.

[10] S. Boldyrev, G. Ivanov-Kholodnu, O. Kolomiitsev, and A. Osin. Influence of solar activity on variations in the density of the earth's upper atmosphere. 51, July 2011.

[11] J. Carvill. Mechanical engineer's data handbook. 1993.

[12] M. W. Chase. Nist-janaf thermochemical tables fourth edition. 1998.

[13] Y. Choi. Review of space industry and technology for asteroid mining. *Journal of the Korean Society of Mineral and Energy Resources Engineers*, 2021.

[14] A. Colaprete, P. Schultz, J. Heldmann, and D. Wooden. Detection of water in the lcross ejecta plume. October 2010.

[15] J. T. Costa, C. T. Lang, P. Corrigan, J. W. Emery, L. A. Thomnson, N. A. Jensen, H. T. Rideout, S. J. Indyk, B. Yen, K. Zacny, M. Mullin, F. Cattani, E. A. Frese, P. Stysley, and B. A. Cohen. Development and testing of a sample handling system for in-situ lunar geochronology with karle. *2022 IEEE Aerospace Conference (AERO)*, pages 1–12, 2022.

[16] J. Craft, J. J. Wilson, P. Chu, K. Zacny, and K. Davis. Percussive digging systems for robotic exploration and excavation of planetary and lunar regolith. *2009 IEEE Aerospace conference*, pages 1–7, 2009.

[17] T. Das, J.-G. Choi, and I. H. Oh. Synthesis of highly effective α-fe2o3 catalyst for the spin conversion of liquid hydrogen. *Proceedings of the National Academy of Sciences, India Section A: Physical Sciences*, pages 1–11, 2020.

[18] J. C. Drake, C. Frondel, J. Itô, and C. Klein. Mineralogical and chemical studies of apollo 11 lunar fines and selected rocks. 1970.

[19] K. Dresia, S. Jentzsch, G. Waxenegger-Wilfing, J. Deeken, M. Oschwald, and F. Mota. Multidisciplinary design optimization of reusable launch vehicles for different propellants and objectives. February 2021.

[20] E. Economics. What is exergy?, Jan 2016. URL https://exergyeconomics.wordpress.com/exergy-economics-101/what-is-exergy/.

[21] ESA. Helium-3 mining on the lunar surface. https://www.esa.int/Enabling_Support/Preparing_for_the_Future/Space_for_Earth/Energy/Helium-3_mining_on_the_lunar_surface, May 2007.

[22] ESA. ISS: International space station. https://www.esa.int/Science_Exploration/Human_and_Robotic_Exploration/International_Space_Station/ISS_International_Space_Station, October 2022.

[23] ESA. Atmosphere-breathing electric propulsion systems for very low orbit. https://www.esa.int/Enabling_Support/Space_Engineering_Technology/Shaping_the_Future/Atmosphere-breathing_electric_propulsion_systems_for_very_low_orbit, October 2022.

[24] S. Fereres and M. Morales. Payload concept evaluation for water/oxygen production on the moon based on thermo- or electro-chemical reduction of lunar regolith. July 2021.

[25] L. A. G. Filho and S. da Silva Fernandes. Preliminary analysis of optimal round trip lunar missions. *Journal of Physics: Conference Series*, 641, 2015.

[26] J. Garche. Encyclopedia of electrochemical power sources. 2009.

[27] M. Gerontidou, A. Vassilaki, H. Mavromichalaki, and V. Kurt. Frequency distributions of solar proton events. October 2002.

[28] F. Ghaffari-Tabrizi, J. Haemisch, and D. Lindner. Reducing hydrogen boil-off losses during fuelling by pre-cooling cryogenic tank. *Hydrogen*, 2022.

[29] H. R. Ghorbani. A review of methods for synthesis of al nanoparticles. *Oriental journal of chemistry*, 30:1941–1949, 2014.

[30] B. Gumusel, L. Kavurmacioglu, and C. Camci. Aerodynamic drag characteristics and shape design of a radar antenna used for airport ground traffic control. 10, December 2010.

[31] S. S. Gursu, M. Lordgooei, S. A. Sherif, and T. N. Veziroglu. An optimization study of liquid hydrogen boil-off losses. *International Journal of Hydrogen Energy*, 17:227–236, 1992.

[32] S. Heiroth, T. Lippert, A. Wokaun, and M. Döbeli. Microstructure and electrical conductivity of ysz thin films prepared by pulsed laser deposition. *Applied Physics A*, 93:639–643, 2008.

[33] B. Hemingway, R. Robie, and W. Wilson. Specific heats of lunar soils, basalt, and breccias from the apollo 14, 15, and 16 landing sites, between 90 and 350 k. 1973.

[34] K. Holste, P. Dietz, S. Scharmann, K. Keil, T. Henning, D. Zschätzsch, M. Reitemeyer, B. T. Nauschütt, F. Kiefer, F. Kunze, J. B. Zorn, C. Heiliger, N. Joshi, U. Probst, R. Thüringer, C. Volkmar, D. M. Packan, S. Peterschmitt, K. T. Brinkmann, H. G. Zaunick, M. H. Thoma, M. Kretschmer, H. J. Leiter, S. Schippers, K. Hannemann, and P. J. Klar. Ion thrusters for electric propulsion: Scientific issues developing a niche technology into a game changer. *The Review of scientific instruments*, 91 6:061101, 2020.

[35] B. S. Jayathilake, I. Ilankoon, and M. Dushyantha. Assessment of significant geotechnical parameters for lunar regolith excavations. *Acta Astronautica*, 2022.

[36] J. Jiang, X. Hu, W. Shen, C. Ni, and J. L. Hertz. Improved ionic conductivity in strained yttria-stabilized zirconia thin films. *Applied Physics Letters*, 102:143901, 2013.

[37] H. Johnston, K. W. E., and A. Friedman. The compressibility of liquid normal hydrogen from the boiling point to the critical point at pressures up to 100 atmospheres. 1954.

[38] A. Jones. China unveils ambitious moon mission plans for 2024 and beyond. https://www.space.com/china-planning-future-moon-missions-change-7, 2020.

[39] G. Just, K. Smith, K. Joy, and M. Roy. Parametric review of existing regolith excavation techniques for lunar in situ resource utilisation (ISRU) and recommendations for future excavation experiments. 180, January 2020.

[40] M. Kaczmarzyk and M. Musial. Parametric study of a lunar base power systems. 2021.

[41] A. Kamran and L. Guozhu. An integrated approach for optimization of solid rocket motor. *Aerospace Science and Technology*, 17:50–64, 2012.

[42] E. Karlsson. Catalytic ortho- to parahydrogen conversion in liquid hydrogen. 2017.

[43] J. Ke, N. Williamson, S. W. Armfield, A. Komiya, and S. Norris. High grashof number turbulent natural convection on an infinite vertical wall. *Journal of Fluid Mechanics*, 929, 2021.

[44] A. Kermanpur, M. R. Dadfar, B. N. Rizi, and M. J. Eshraghi. Synthesis of aluminum nanoparticles by electromagnetic levitational gas condensation method. *Journal of nanoscience and nanotechnology*, 10 9:6251–5, 2010.

[45] J. L. Klosky, S. Sture, H. Y. Ko, and F. S. Barnes. Vibratory excavation and anchoring tools for the lunar surface. 1996.

[46] Y. A. Kotov. Electric explosion of wires as a method for preparation of nanopowders. *Journal of Nanoparticle Research*, 5:539–550, 2003.

[47] R. Kumar, R. P. Singh, A. K. Chinnappan, and A. Appar. Simulation of the orbital decay of a spacecraft in low earth orbit due to aerodynamic drag. *The Aeronautical Journal*, 2021.

[48] B. Lamboray, M. G. Link, and G. Martin. The luxembourg perspective on isru and the development of a commercial space ecosystem. 2019.

[49] J. W. Leachmana. Fundamental equations of state for parahydrogen , normal hydrogen , and orthohydrogen. 2009.

[50] X.-B. Li, R. Li, L. Hu, S. Zhu, Y. Zhang, X. K. Cui, and Y. Li. Performance analysis of a dish solar thermal power system with lunar regolith heat storage for continuous energy supply of lunar base. *Energy*, 2022.

[51] B. A. Lomax, M. Conti, N. Khan, N. Bennett, A. Ganin, and M. Symes. Proving the viability of an electrochemical process for the simultaneous extraction of oxygen and production of metal alloys from lunar regolith. 2020.

[52] A. Mahjub, N. M. Mazlan, M. Z. Abdullah, and Q. Azam. Design optimization of solid rocket propulsion: A survey of recent advancements. *Journal of Spacecraft and Rockets*, 57:3–11, 2020.

[53] V. R. Manikam, K. Y. Cheong, and K. A. Razak. Chemical reduction methods for synthesizing ag and al nanoparticles and their respective nanoalloys. *Materials Science and Engineering B-advanced Functional Solid-state Materials*, 176:187–203, 2011.

[54] J. Matchett. In-situ production of oxygen through lunar regolith pyrolysis. January 2006.

[55] E. M. Mazarico, G. A. Neumann, D. E. Smith, M. T. Zuber, and M. H. Torrence. Illumination conditions of the lunar polar regions using lola topography. *Icarus*, 211:1066–1081, 2011.

[56] L. C. A. Mazzone, G. A. Ratcliffe, J. M. Rieubland, and G. Vandoni. Measurements of multi-layer insulation at high boundary temperature, using a simple non-calorimetric method. 2002.

[57] G. E. Mcintosh. Applications of ortho-para hydrogen catalyst. *IOP Conference Series: Materials Science and Engineering*, 101, 2015.

[58] C. L. McLeod and M. P. S. Krekeler. Sources of extraterrestrial rare earth elements: To the moon and beyond. *Resources*, 6:40, 2017.

[59] H. Meng, D. Zeng, and F. Xie. Recent development of pd-based electrocatalysts for proton exchange membrane fuel cells. *Catalysts*, 5:1221–1274, 2015.

[60] C. Meyer. The lunar petrographic educational thin section set. September 2003.

[61] D. W. Ming. Lunar sourcebook. a user's guide to the moon. *Endeavour*, 16:96, 1992.

[62] D. R. Morris and J. T. Szargut. Standard chemical exergy of some elements and compounds on the planet earth. *Energy*, 11:733–755, 1986.

[63] NASA. Earth atmosphere model - metric units. URL https://www.grc.nasa.gov/www/k-12/airplane/atmosmet.html.

[64] NASA. Nasa's plan for sustained lunar exploration and development. 2019.

[65] M. Ni, M. Leung, and D. Leung. Energy and exergy analysis of hydrogen production by a proton exchange membrane (pem) electrolyzer plant. 49, October 2008.

[66] W. Notardonato, A. Swanger, J. Fesmire, K. Jumper, W. Johnson, and T. Tomsik. Lunar ISRU 2019: Developing a new space economy through lunar resources and their utilization. July 2019.

[67] S. Ohara, K. Mukai, T. Fukui, Y. Sakaki, M. Hattori, and Y. Esaki. A new sealant material for solid oxide fuel cells using glass-ceramic. *Journal of the Ceramic Society of Japan*, 109:186–190, 2001.

[68] M. Oliveira, R. Nogueira, and A. V. Machado. Synthesis of aluminium nanoparticles in a pp matrix during melt processing: Effect of the alkoxide organic chain. *Reactive & Functional Polymers*, 72:703–712, 2012.

[69] J. J. Papike, S. B. Simon, and J. C. Laul. The lunar regolith: Chemistry, mineralogy, and petrology. *Reviews of Geophysics*, 20:761–826, 1982.

[70] C. Pardini and L. Anselmo. Monitoring the orbital decay of the chinese space station tiangong-1 from the loss of control until the re-entry into the earth's atmosphere. *Journal of Space Safety Engineering*, 6: 265–275, 2019.

[71] M. J. Patterson and G. J. Williams. Krypton ion thruster performance. 1992.

[72] R. Petela. Exergy analysis of the solar cylindrical-parabolic cooker. *Solar Energy*, 79:221–233, 2005.

[73] D. I. Poston, M. A. Gibson, T. J. Godfroy, and P. R. McClure. Krusty reactor design. *Nuclear Technology*, 206:S13 – S30, 2020.

[74] D. I. Poston, M. A. Gibson, R. Sanchez, and P. R. McClure. Results of the krusty nuclear system test. *Nuclear Technology*, 206:S117 – S89, 2020.

[75] T. Pourpoint, T. Sippel, C. Zaseck, and T. Wood. Detailed characterization of al/ice propellants. In *46th AIAA/ASME/SAE/ASEE Joint Propulsion Conference Exhibit*, 2010.

[76] T. Pourpoint, T. Wood, M. Pfeil, J. Tsohas, and S. Son. Feasibility study and demonstration of an aluminum and ice solid propellant. 2012.

[77] L. Rabagliati, M. Devecchi, A. Lovagnini, P. Pino, and G. Thirion. Regolith mining in shackleton crater on the moon: Propellant, building materials and vital resources production for a long duration manned mission. 2021.

[78] Z. Rant. Exergie, ein neues wortfur 'technishe arbeitsfahigkeit'. 1956.

[79] G. V. R. Rao. Exhaust nozzle contour for optimum thrust. *Journal of Jet Propulsion*, 28:377–382, 1958.

[80] J. Rasera, J. J. Cilliers, J. Lamamy, and K. Hadler. The beneficiation of lunar regolith for space resource utilisation: A review. *Planetary and Space Science*, 186:104879, 2020.

[81] G. A. Risha, T. L. Connell, R. A. Yetter, V. Yang, T. D. Wood, M. A. Pfeil, T. L. Pourpoint, and S. F. Son. Aluminum-ice (alice) propellants for hydrogen generation and propulsion. 2009.

[82] R. Rivero and M. A. A. Garfias. Standard chemical exergy of elements updated. *Energy*, 31:3310–3326, 2006.

[83] H. Sargeant, S. Barber, M. Anand, F. Abernethy, S. Sheridan, I. Wright, and A. Morse. Feasibility studies for hydrogen reduction of ilmenite in a static system for use as an isru demonstration on the lunar surface. 180, January 2020.

[84] H. Sargeant, S. Barber, M. Anand, F. Abernethy, , S. Sheridan, I. Wright, and A. Morse. Hydrogen reduction of lunar samples in a static system for a water production demonstration on the moon. 205, October 2021.

[85] H. M. Sargeant, S. Barber, M. Anand, F. A. J. Abernethy, S. Sheridan, I. P. Wright, and A. D. Morse. Hydrogen reduction of lunar samples in a static system for a water production demonstration on the moon. *Planetary and Space Science*, 205:105287, 2021.

[86] C. J. Schaschke. A dictionary of chemical engineering. 2014.

[87] S. Schreiner. Molten regolith electrolysis reactor modeling and optimization of in-situ resource utilization systems. January 2015.

[88] S. Schreiner, L. Sibille, J. Dominguez, and J. Hoffmann. A parametric sizing model for molten regolith electrolysis reactors to produce oxygen on the moon. 57, April 2016.

[89] K. Skonieczny, T. J. Carlone, W. Whittaker, and D. S. Wettergreen. Considering the effects of gravity when developing and field testing planetary excavator robots. In *International Symposium on Field and Service Robotics*, 2015.

[90] D. Smith, R. Mueller, J. Schuler, A. Nick, A. Langton, B. Buckles, and K. Leucht. Rassor excavator for ISRU lunar mining. July 2019.

[91] J. V. Smith and I. M. Steele. Lunar mineralogy; a heavenly detective story; part ii. *American Mineralogist*, 61:1059–1116, 1976.

[92] J. F. Stebbins, I. Carmichael, and L. Moret. Heat capacities and entropies of silicate liquids and glasses. *Contributions to Mineralogy and Petrology*, 86:131–148, 1984.

[93] E. Stoll, P. Härke, S. Linke, F. Heeg, and S. May. The regolith rocket—a hybrid rocket using lunar resources. *Acta Astronautica*, 179:509–518, 2021.

[94] V. Sundararajan and I. Introduction. Indian lunar space exploration program - chandrayaan i and ii missions. 2012.

[95] J. Szargut. Chemical exergies of the elements. volume 32, 1989.

[96] J. T. Szargut. Chemical exergies of the elements. *Applied Energy*, 32:269–286, 1989.

[97] H. Tang, S. Pei-kang, S. P. Jiang, F. Wang, and M. Pan. A degradation study of nafion proton exchange membrane of pem fuel cells. *Journal of Power Sources*, 170:85–92, 2007.

[98] E. Turan, S. Stein, R. Maharaj, and K. Möller. A flow sheet for the conversion of lunar regolith using fluorine gas. April 2020.

[99] P. J. van Susante and C. B. Dreyer. Lunar and planetary excavation prototype development and testing at the colorado school of mines. 2010.

[100] S. Vijapur, T. Hall, H. Garich, M. Inman, S. Snyder, and H. Nulwala. Ionic liquid-assisted electrochemical extraction of oxygen from lunar regolith. March 2021.

[101] K. F. Wakker. Fundamentals of astrodynamics. 2015.

[102] J. Wang, Z. Lü, X. Huang, K. Chen, N. Ai, J. Hu, and W. Su. Ysz films fabricated by a spin smoothing technique and its application in solid oxide fuel cell. *Journal of Power Sources*, 163:957–959, 2007.

[103] K. Wang, Z. Shi, Y. Shi, and Z. Zhao. Characteristics of the electrical explosion of fine metallic wires in vacuum. *AIP Advances*, 7:095002, 2017.

[104] J. Williams, D. Paige, and B. Greenhagen. The global surface temperatures of the moon as measured by the diviner lunar radiometer experiment. 2017.

[105] B. Yu, W. Zhang, J. Xu, J. Y. Chen, X.-Z. Luo, and K. Stephan. Preparation and electrochemical behavior of dense ysz film for soec. *International Journal of Hydrogen Energy*, 37:12074–12080, 2012.

[106] B. Zandbergen. Simple mass and size estimation relationships of pump fed rocket engines for launch vehicle conceptual design. June 2015.

[107] B. Zandbergen. i ae4-s01 thermal rocket propulsion. 2020.

[108] Y. Zhang, G. Bhattacharjee, R. K. Kumar, and P. Linga. Solidified hydrogen storage (solid-hystore) via clathrate hydrates. *Chemical Engineering Journal*, 2021.

[109] G. Zhou and W. Wang. Synthesis of silver nanoparticles and their antiproliferation against human lung cancer cells in vitro. *Oriental journal of chemistry*, 28:651–655, 2012.

[110] J. Zhou, J. Zhang, and Z. Zhong. Mechanical properties of yttria-stabilized zirconia: A study by reaxff molecular dynamics simulations. *Mechanics of Materials*, 149:103542, 2020.

[111] R. M. Zubrin. Moon direct: A cost-effective plan to enable lunar exploration and development. *AIAA Scitech 2019 Forum*, 2019.